

Superhydrophobic, Biomimetic Surfaces with High and Low Adhesion, Optical Transmittance, and Nanoscale Mechanical Wear Resistance

DISSERTATION

Presented in Partial Fulfillment of the Requirements for the Degree Doctor of Philosophy
in the Graduate School of The Ohio State University

By

Daniel R. Ebert

Graduate Program in Mechanical Engineering

The Ohio State University

2016

Dissertation Committee:

Professor Bharat Bhushan, Advisor

Professor Terrence Conlisk

Professor Noriko Katsube

Professor Soheil Soghrati

Copyrighted by

Daniel R. Ebert

2016

ABSTRACT

Superhydrophobic surfaces (defined as surfaces having water contact angle greater than 150°) show great promise for use in a rapidly growing number of engineering applications, ranging from biomedical devices to fluid drag reduction in pipelines. In nature, the surfaces of many organisms, such as certain plant leaves, are known to exhibit superhydrophobicity. In some cases, droplet adhesion is very low (droplet rolls away easily), while in other cases adhesion is high (droplet remains adhered when surface is inverted). The recent advent and development of microscopes with resolution down to a few nanometers (such as atomic force microscopes and scanning electron microscopes) has allowed for in-depth understanding of the micro- and nanoscale mechanisms employed by these plant leaves and other natural surfaces to achieve their particular wetting properties. Biomimetics (or “mimicking nature”) is therefore a very promising approach for the development of engineering surfaces with desired wetting characteristics. However, research in creating biomimetic surfaces is still in its early stages, and many of the surfaces created thus far are not mechanically robust, which is required for many potential real-world applications. In addition, for applications such as self-cleaning windows and solar panels, optical transparency is required.

In this thesis, a set of original studies are presented in which superhydrophobic surfaces were designed based on biomimetics and fabricated using a wide of variety of techniques. The surfaces were characterized with regard to wetting characteristics such as water contact angle and contact angle hysteresis, micro- and nanoscale mechanical durability, and in some cases optical transmittance. Theoretical wetting models served as guides both in the design and in the understanding of experimental results, especially in regard to different wetting regime and regime transition. This work provides important conclusions and valuable insight for identifying materials, techniques, and designs for mechanically durable, optically transparent superhydrophobic surfaces.

Dedicated to my parents

ACKNOWLEDGMENTS

I would like to thank first and foremost my research advisor, Professor Bharat Bhushan, for working with me at every step of this long journey. I have made enormous strides professionally because of his guidance and tutelage. Next I would like to thank my fellow researchers at NLBB, especially Dr. Manuel Palacio and Dr. Philip Brown, who provided critical assistance with my work in the lab. I thank the graduate advising staff of the mechanical engineering department, as well as my doctoral committee members, Professor Terrence Conlisk, Professor Noriko Katsube, and Professor Soheil Soghrati. I thank The Ohio State University for a full undergraduate scholarship, for countless academic, research, and teaching opportunities, and for so many memorable experiences. Lastly I want to thank my family, my true friends, and all of my teachers throughout my life.

VITA

2002.....	Beavercreek High School Beavercreek, Ohio, USA
2008.....	B.S. Mechanical Engineering The Ohio State University
2012.....	M.S. Mechanical Engineering The Ohio State University

PUBLICATIONS

1. Ebert, D. and Bhushan, B. (2012a), “Durable Lotus-effect surfaces with hierarchical structure using micro- and nanosized hydrophobic silica particles,” *J. Colloid Interf. Sci.* **368**, 584-591
2. Ebert, D. and Bhushan, B. (2012b), “Wear-resistant rose petal-effect surfaces with superhydrophobicity and high droplet adhesion using hydrophobic and hydrophilic nanoparticles,” *J. Colloid Interf. Sci.* **384**, 182-188
3. Ebert, D. and Bhushan, B. (2012c), “Transparent, Superhydrophobic, and Wear-Resistant Coatings on Glass and Polymer Substrates Using SiO₂, ZnO, and ITO Nanoparticles,” *Langmuir* **28**, 11391–11399

4. Ebert, D.R. and Bhushan, B. (2013), “Methods of Fabricating Superhydrophobic, Optically Transparent Surfaces,” U.S. Patent Pending
5. Ebert, D. and Bhushan, B. (2016), “Transparent, superhydrophobic, and wear-resistant surfaces using deep reactive ion etching on PDMS substrates,” *J. Colloid Interf. Sci.* **481**, 82-90

FIELDS OF STUDY

Major Field: Mechanical Engineering

TABLE OF CONTENTS

ABSTRACT	ii
ACKNOWLEDGMENTS	v
VITA	vi
LIST OF TABLES	xii
LIST OF FIGURES	xiv
CHAPTER 1: Introduction	1
1.1 Significance of the problem	1
1.2 Overview of surface wettability and superhydrophobicity	2
1.3 Biomimetics and extreme wettability found in nature	14
1.4 Scope of the thesis	19
CHAPTER 2: Lotus Effect Surfaces with Superhydrophobicity and Low Droplet Adhesion	23
2.1 Introduction	23
2.2 Overview of wettability on a patterned surface	25
2.3 Sample preparation and characterization	27

2.3.1 Samples using epoxy micropatterns and nanoparticles	27
2.3.2 Samples using micro- and nanoparticles	31
2.3.3 Characterization of samples with microstructured, nanostructured, and hierarchically structured surfaces	32
2.4 Results and discussion for hierarchically structured surfaces.....	35
2.4.1 Wettability of structured surfaces using micropattern.....	36
2.4.2 Wettability of surfaces with microparticles and comparison to surfaces with micropattern.....	38
2.4.3 Wear resistance in AFM sliding wear, tribometer, and water jet experiments	40
2.5 Conclusions	44
 CHAPTER 3: Rose Petal Effect Surfaces with Superhydrophobicity and High Droplet Adhesion	
3.1 Introduction and Background.....	47
3.2 Experimental details.....	51
3.2.1 Preparation of hierarchically structured samples.....	51
3.2.2 Characterization of samples.....	54
3.3 Results and discussion.....	54
3.3.1 Samples with hydrophilic nanostructure (before modification).....	55
3.3.2 Samples with hydrophobic nanostructure (after modification)	62

3.3.3 Wear resistance in AFM sliding wear experiment	68
3.4 Conclusions	70
CHAPTER 4: Superhydrophobic Surfaces with High Optical Transmittance on Glass and Polymer Substrates Using Dip-Coated Nanoparticles	72
4.1 Introduction	72
4.2 Experimental details	77
4.2.1 Materials	77
4.2.2 Functionalization of nanoparticles and dip coat procedure	78
4.2.3 Characterization of dip-coated glass and polymer samples.....	79
4.3 Results and discussion for dip-coated glass and polymer samples	82
4.3.1 Surface roughness and morphology	82
4.3.2 Wettability and optical transmittance	85
4.3.3 Wear resistance in AFM sliding wear and water jet experiments	93
4.4 Conclusions	96
CHAPTER 5: Superhydrophobic Surfaces with High Optical Transmittance on PDMS Using Reactive Ion Etching	100
5.1 Introduction	100
5.2 Experimental Details	103
5.2.1 Materials	103

5.2.2 Reactive ion etching of PDMS and fluorosilane vapor deposition	104
5.2.3 Characterization of etched PDMS samples	107
5.3 Results and discussion for etched PDMS samples.....	110
5.3.1 Surface roughness and morphology	110
5.3.2 Wettability and optical transmittance	112
5.3.3 Comparison of measured CA and CAH to predicted values	117
5.3.4 Wear resistance in AFM sliding wear experiment	122
5.4 Conclusions	123
CHAPTER 6: Summary and Future Work	126
BIBLIOGRAPHY	133

LIST OF TABLES

Table 1: Potential advantages and disadvantages of hydrophobic vs. hydrophilic nanoparticles in fabrication of structured surfaces (Ebert and Bhushan, 2012b)	50
Table 2: Summary of measured and calculated contact angle (CA) and measured contact angle hysteresis (CAH) for selected superhydrophobic surfaces with high and low adhesion using hydrophilic ZnO nanoparticles. Where microstructure is used, data for hierarchical structure correspond to final samples (Ebert and Bhushan, 2012b).	59
Table 3: Summary of measured and calculated contact angle (CA) and measured contact angle hysteresis (CAH) for selected superhydrophobic surfaces with high and low adhesion using hydrophobic ZnO nanoparticles. Data for hierarchical structure correspond to final samples (Ebert and Bhushan, 2012b).	66
Table 4: Typical values for optical properties, electrical resistivity, and hardness for SiO ₂ , ZnO, and indium tin oxide (ITO) (Ebert and Bhushan, 2012c).....	73
Table 5: Summary of recent studies in fabricating transparent superhydrophobic surfaces on glass substrates (Ebert and Bhushan, 2012c).....	75
Table 6: Summary of recent studies in fabricating transparent superhydrophobic surfaces on polymer substrates (Ebert and Bhushan, 2012c)	76
Table 7: Measured roughness values (RMS, PV, and R_f), coating thickness, and estimated liquid-air fractional area (f_{LA}) for samples with SiO ₂ , ZnO, and indium tin oxide (ITO) (Ebert and Bhushan, 2012c)	83

Table 8: Wettability and optical transmittance data for all dip-coated samples using SiO₂, ZnO, and indium tin oxide (ITO) nanoparticles (Ebert and Bhushan, 2012c)..... **86**

Table 9: Measured and calculated CA and CAH values for samples with SiO₂, ZnO, and indium tin oxide (ITO) nanoparticles. Measured values are taken from samples on glass substrates (Ebert and Bhushan, 2012c)..... **90**

Table 10: Measured roughness values (RMS, PV, and R_f) and estimated liquid-air fractional area (f_{LA}) for samples etched by O₂/CF₄ plasma only, samples etched by O₂/CF₄ with subsequent C₄F₈ plasma treatment, and samples etched by O₂/CF₄ with subsequent perfluorooctyltrichlorosilane (PFOTCS) vapor deposition (Ebert and Bhushan, 2016) **111**

Table 11: Summary of measured and calculated contact angle (CA) and measured contact angle hysteresis (CAH) for samples etched by O₂/CF₄ plasma only, samples etched by O₂/CF₄ with subsequent C₄F₈ plasma treatment, and samples etched by O₂/CF₄ with subsequent perfluorooctyltrichlorosilane (PFOTCS) vapor deposition. ($f_{LA}=0$ assuming Wenzel state, $R_f \sim 1$ assuming Cassie-Baxter state) (Ebert and Bhushan, 2016) **119**

Table 12: Summary of measured and calculated contact angle hysteresis (CAH) for samples etched by O₂/CF₄ plasma only, samples etched by O₂/CF₄ with subsequent C₄F₈ plasma treatment, and samples etched by O₂/CF₄ with subsequent perfluorooctyltrichlorosilane (PFOTCS) vapor deposition. Based on CA analysis in Table 11, Wenzel state assumed ($f_{LA}=0$) for samples with 0 and 5 min etch times and Cassie-Baxter state assumed ($R_f \sim 1$) for samples with 10, 15, 20, 25 min etch times (Ebert and Bhushan, 2016). **121**

LIST OF FIGURES

Figure 1: Illustration of hydrophobic and hydrophilic surfaces with contact angle θ	3
Figure 2: Schematics of a Wenzel wetting interface (full wetting) and a Cassie-Baxter wetting interface (composite with air pockets) (adapted from Bhushan, 2016)	4
Figure 3: Schematic of a liquid droplet in contact with a smooth solid surface (contact angle θ_0) and with a rough solid surface (contact angle θ) (Bhushan, 2016)	6
Figure 4: (a) Droplet in contact with a rough surface with liquid added or removed (advancing and receding contact angles are θ_{adv} and θ_{rec} , respectively) and (b) tilted surface profile (tilt angle α with a moving liquid droplet). The contact angle hysteresis (CAH) is defined as $\theta_{adv} - \theta_{rec}$ (Bhushan, 2016)	7
Figure 5: Schematic of four different surface structure types and their wetting behaviors. The largest contact area between the droplet and the surface occurs on flat and microstructured surfaces, but is reduced on nanostructured surfaces and minimized on hierarchically structured surfaces (Jung and Bhushan, 2009).	9
Figure 6: Schematic examples of (a) non-re-entrant surface geometry supporting non-wetting by liquid for flat surface CA of 90° , (b) re-entrant geometry supporting non-wetting for flat surface CA of 30° , and (c) doubly re-entrant geometry supporting non-wetting for flat surface CA of $\sim 0^\circ$ (Ebert and Bhushan, 2016)	11
Figure 7: Schematic showing a droplet sliding on a smooth surface, leading to redistribution of contaminant particles, and a droplet rolling on a lotus-like surface with low contact angle hysteresis and low adhesion/drag, removing contaminant particles from the leaf surface (Bhushan, 2016)	13

Figure 8: Examples from nature that have inspired researchers developing new products (adapted from Bhushan, 2009). Shown are (a) water droplet on a self-cleaning Lotus leaf and its micropapillae, (b) glands of carnivore plant that trap insects, (c) water strider walking on water and its leg structure, (d) Gecko feet spatula with reversible adhesion, (e) riblet-covered low-drag and antifouling shark skin, (f) bird wing structure and orientation during landing approach, (g) spider webs made of silk strands, and (h) antireflective moth eyes.	15
Figure 9: SEM micrographs (shown at three magnifications) of a lotus (<i>Nelumbo nucifera</i>) leaf surface, consisting of microstructure formed by papillose epidermal cells covered with 3-D epicuticular wax tubules on surface, which create nanostructure, and an image of a water droplet sitting on a lotus leaf with a contact angle of about 164° (Bhushan <i>et al.</i> , 2009).....	17
Figure 10: Optical micrographs of water droplets on <i>Rosa, cv. Bairage</i> at 0° and 180° tilt angles. Droplet is still suspended when the petal is turned upside down (adapted from Bhushan and Her, 2010).....	18
Figure 11: SEM images of <i>Rosa, cv. Bairage</i> at three magnifications (adapted from Bhushan and Her, 2010)	18
Figure 12: SEM micrographs of superhydrophilic leaves and mosses (Koch and Barthlott, 2009). (a) Water plant <i>Anubias barteri</i> with unstructured, flat surface. (b) Surface of water-absorbing moss <i>Sphagnum squarrosum</i> . (c) Porous structure of <i>Rhacocarpus purpureus</i> moss formed by epidermal cells. (d) Water-absorbing hairs of Spanish moss <i>Tillandsia usneoides</i> . (e) <i>Calathea zebrine</i> leaf surface with conical cells. (f) <i>Ruellia devosiana</i> leaf surface employing different cell types.	20
Figure 13: Schematic of a small water droplet suspended on a superhydrophobic surface consisting of a uniform array of cylindrical pillars. The maximum droop of the droplet occurs in the center of the square formed by four pillars (Jung and Bhushan, 2009).	26
Figure 14: Schematic examples of microstructured and hierarchically structured surfaces in which the microstructure is formed by both a uniform micropattern (top) and microparticles (bottom). In both cases, the hierarchical structure is achieved through addition of nanoparticles (Ebert and Bhushan, 2012a).	27

Figure 15: Two-step molding process to create epoxy micropatterns through soft lithography (top), and SEM micrographs of Si master micropattern template and positive replica epoxy micropattern (bottom) (Jung and Bhushan, 2009).....	29
Figure 16: Illustration of spray method to deposit a mixture of SiO ₂ micro- and/or nanoparticles, epoxy, and acetone on surfaces (Jung and Bhushan, 2009)	30
Figure 17: SEM micrographs taken at 45° tilt angle showing 10 nm particles on flat surface at high magnification (top), epoxy micropattern at three magnifications (middle) and 10 nm particles on micropattern at three magnifications (bottom) (Ebert and Bhushan, 2012a).....	31
Figure 18: SEM micrographs taken at 45° tilt angle showing microparticles with and without nanoparticles at two different concentrations of microparticles in spray solution. Three magnifications are shown for microparticle spray concentrations of (a) 400 mg/L and (b) 1400 mg/L, both with and without nanoparticles in each case. The resulting average pitch values (P_{avg}) are indicated on images at lowest magnification. Nanoparticle concentration was 2000 mg/L when added (Ebert and Bhushan, 2012a).	33
Figure 19: Schematic of water jet setup shown in front and side views (Jung and Bhushan, 2009)	36
Figure 20: Bar chart showing the measured static contact angle and contact angle hysteresis on nano-, micro- and hierarchically structured surfaces using both 10 nm and 50 nm particles. The error bars represent ± 1 standard deviation. (Ebert and Bhushan, 2012a).	37
Figure 21: Static contact angle and contact angle hysteresis as a function of average pitch for surfaces with 10 μm particles alone and with 10 μm /10 nm particles combined. Epoxy micropattern data is also shown for comparison of microstructure behavior. Reproducibility is $\pm 1^\circ$ for CAH of 10 μm /10 nm particles combined, $\pm 2^\circ$ for CAH of 10 μm particles and epoxy micropatterns, and $\pm 2^\circ$ for all CA data. Lines between data points are intended only to guide the eyes and not for interpolation (Ebert and Bhushan, 2012a).....	39

Figure 22: Surface height maps and sample surface profiles (locations indicated by arrows) before and after AFM wear experiment with 15 μm radius borosilicate ball at load of 10 μN for 10 nm particles on flat surface (top) and epoxy resin on flat surface (bottom). RMS roughness values for surface profiles are displayed within surface profile boxes (Ebert and Bhushan, 2012a)..... 41

Figure 23: Optical micrographs before and after wear experiment using ball-on-flat tribometer at 10 mN for 10 μm particles (top), 10 μm particles with 10 nm particles (middle), and epoxy resin on flat surface (bottom). Sample profiles across wear areas are shown below after-images (arrows indicate location of profile) (Ebert and Bhushan, 2012a). 43

Figure 24: Static contact angle (top) and contact angle hysteresis (bottom) as a function of water pressure after 20 min. exposure time for samples with combined 10 μm /10 nm particles and epoxy resin on flat surface. Reproducibility is $\pm 1^\circ$ for CAH of 10 μm /10 nm particles, $\pm 2^\circ$ for CAH of epoxy resin, and $\pm 2^\circ$ for all CA data. Lines between data points are intended to guide the eyes (Ebert and Bhushan, 2012a). 45

Figure 25: Schematic of droplets on superhydrophobic surfaces with high adhesion (impregnating regime, shown at top) and low adhesion (Cassie-Baxter regime, shown at bottom). Surfaces have hierarchical structure with same microstructure pitch value and different nanostructure density (Ebert and Bhushan, 2012b)..... 49

Figure 26: Schematic of hydrophobization of a generic metal oxide surface with octadecylphosphonic acid (ODP). The ODP molecule first attaches to the hydrolyzed surface via hydrogen bonds. After annealing, the ODP is strongly bonded to the metal oxide surface (Ebert and Bhushan, 2012c). 53

Figure 27: SEM micrographs of (a) ZnO nanoparticles on flat substrate at three magnifications and (b) low magnification images of microstructures at three different pitch values, along with high magnification images of individual micropillar with two different nanoparticle spray concentrations. The different spray concentrations produce different nanostructure density values. (Ebert and Bhushan, 2012b) 56

Figure 28: Contact angle and contact angle hysteresis data on nanostructured surfaces with hydrophilic ZnO nanoparticles (before modification with octadecylphosphonic acid (ODP)) using microstructures with three different pitch values (23 μm , 105 μm , 210 μm) as well as a flat substrate. Reproducibility is $\pm 1^\circ$ for CA data and $\pm 2^\circ$ for

CAH data. “Low adhesion” indicates $CAH < 30^\circ$, while “high adhesion” indicates adherence of droplet to an inverted substrate. Lines between data points are intended only to guide the eyes and not for interpolation (Ebert and Bhushan, 2012b). 57

Figure 29: Illustration of approximation method for true surface area using an AFM scan matrix. Using the Z-height of each data point, two right triangles can be formed for each patch. The area of the patch (A_{patch}) is taken as the sum of the areas of the two triangles (Burton and Bhushan, 2006). 61

Figure 30: Droplets on flat substrate with hydrophilic ZnO nanoparticles at 3000 mg/L spray concentration at 0° tilt, 90° tilt, and fully inverted, showing superhydrophobicity and high droplet adhesion (Ebert and Bhushan, 2012b). 63

Figure 31: Contact angle and contact angle hysteresis data on nanostructured surfaces with hydrophobic ZnO nanoparticles (after modification with octadecylphosphonic acid (ODP)) using microstructures with three different pitch values (23 μm , 105 μm , 210 μm) as well as a flat substrate. Reproducibility is $\pm 1^\circ$ for CA data and $\pm 2^\circ$ for CAH data. “Low adhesion” indicates $CAH < 30^\circ$, while “high adhesion” indicates adherence of droplet to an inverted substrate. Lines between data points are intended only to guide the eyes and not for interpolation (Ebert and Bhushan, 2012b). 64

Figure 32: Droplets on hierarchically structured surfaces with microstructure pitch value of 105 μm and two different spray concentrations (1000 mg/L and 2250 mg/L) of hydrophobic ZnO nanoparticles resulting in superhydrophobicity with high adhesion (with 1000 mg/L) and low adhesion (with 2250 mg/L). In the case of low adhesion, air pockets are visible beneath droplet. Droplet in high adhesion state is also shown at 90° tilt and fully inverted (Ebert and Bhushan, 2012b). 67

Figure 33: Surface height maps and sample surface profiles (locations indicated by arrows) before and after AFM sliding wear experiment using 15 μm radius borosilicate ball at load of 10 μN for glass samples with hydrophobic ZnO nanoparticles on flat substrate as well as epoxy resin alone on flat substrate. RMS roughness and PV distance values for surface profiles are displayed within surface profile boxes (Ebert and Bhushan, 2012b). 69

Figure 34: Simplified schematic of dip coat procedure used to create transparent, superhydrophobic nanoparticle coatings on glass, polycarbonate, and PMMA substrates. The mixture of nanoparticles (SiO_2 , ZnO, or indium tin oxide (ITO)),

silicone resin, and solvent is first sonicated to ensure dispersion in the solvent. Then, substrates are dipped and slowly removed vertically from the mixture, leaving a thin nanoparticle layer that is strongly bonded to the substrate by the silicone resin after annealing. 80

Figure 35: SEM micrographs of SiO₂, ZnO, and indium tin oxide (ITO) nanoparticle coatings on glass substrates at two magnifications each showing nanoscale roughness (Ebert and Bhushan, 2012c). 84

Figure 36: Bar chart showing contact angle (CA), contact angle hysteresis (CAH), and optical transmittance for samples with SiO₂, ZnO, and indium tin oxide (ITO) nanoparticles on glass, polycarbonate, and PMMA substrates. Error bars represent ± 1 standard deviation (Ebert and Bhushan, 2012c). 87

Figure 37: Transmittance spectra in the visible range ($\lambda = 400-700$ nm) for samples with silica (SiO₂), zinc oxide (ZnO), and indium tin oxide (ITO) nanoparticle coatings on glass, polycarbonate, and poly(methyl methacrylate) (PMMA) substrates. Data represent optical transmittance as a percentage of the optical transmittance of the uncoated substrate (Ebert and Bhushan, 2012c). 92

Figure 38: Water droplets deposited on glass, polycarbonate, and PMMA with indium tin oxide (ITO) nanoparticle coatings showing superhydrophobicity and high optical transmittance (top). Blue dye was added to water for visual clarity of droplets. Goniometer image of droplet is shown for glass substrate with ITO coating (bottom) (Ebert and Bhushan, 2012c). 94

Figure 39: Surface height maps and sample surface profiles (locations indicated by arrows) before and after AFM sliding wear experiment using 15 μm radius borosilicate ball at load of 10 μN for glass samples with silicone resin alone, SiO₂ nanoparticles, ZnO nanoparticles, and indium tin oxide (ITO) nanoparticles. RMS roughness and PV distance values for surface profiles are displayed within surface profile boxes. Results shown are typical for all substrates (Ebert and Bhushan, 2012c). 95

Figure 40: Contact angle (CA) and contact angle hysteresis (CAH) as a function of water pressure after 20 min. exposure time for samples with SiO₂ nanoparticles on glass and silicone resin alone on glass. Reproducibility is $\pm 1^\circ$ for CAH of SiO₂ nanoparticles, $\pm 2^\circ$ for CAH of silicone resin alone on glass, and $\pm 2^\circ$ for all CA data. Results shown are typical for all samples. CA > 150° and CAH < 10° were

maintained in all cases. Lines between data points are intended to guide the eyes (Ebert and Bhushan, 2012c)..... 97

Figure 41: Illustration of plasma chamber configured for reactive ion etching of PDMS samples. The sample is placed on the electrode connected to the excitation source, with the other electrode grounded. This causes directional bombardment of ions toward the sample surface leading to higher etch rate with greater anisotropy. 105

Figure 42: Schematic of (a) reactive ion etching of PDMS by O₂/CF₄ and subsequent C₄F₈ plasma treatment, and (b) reactive ion etching of PDMS by O₂/CF₄ and subsequent vapor deposition of perfluorooctyltrichlorosilane (PFOTCS). In both cases, the surface is first etched anisotropically by the oxyfluoride (OF⁻) ions formed in the O₂/CF₄ mixture, resulting in a rough surface. In the case of C₄F₈ treatment (a), a thin fluorocarbon layer is then formed on the surface. In the case of PFOTCS modification (b), after surface activation by O₂ plasma, a covalently bonded fluorosilane layer is then formed with exposed long-chain hydrophobic tails (Ebert and Bhushan, 2016). 106

Figure 43: SEM micrographs of (a) unetched, virgin PDMS sample at high magnification and (b) PDMS samples at three magnifications after 10 min and after 20 min etch time by O₂/CF₄ plasma (Ebert and Bhushan, 2016)..... 113

Figure 44: Contact angle and contact angle hysteresis data on PDMS samples of varying RMS roughness values for samples etched by O₂/CF₄ plasma only, by O₂/CF₄ with subsequent C₄F₈ plasma treatment, and by O₂/CF₄ with subsequent perfluorooctyltrichlorosilane (PFOTCS) vapor deposition. Reproducibility is ±1° for CA data and ±2° for CAH data. Lines between data points are intended only to guide the eyes and not for interpolation (Ebert and Bhushan, 2016)..... 114

Figure 45: Optical transmittance of O₂/CF₄ etched PDMS samples of varying RMS roughness values. Data represent the percentage of the baseline transmittance of a PDMS substrate, and is taken as the average across the visible range ($\lambda = 400\text{--}700$ nm). Lines between data points are intended only to guide the eyes and not for interpolation (Ebert and Bhushan, 2016). 116

Figure 46: Water droplet deposited on PDMS sample etched by O₂/CF₄ for 15 min with subsequent C₄F₈ plasma treatment showing superhydrophobicity and high optical transmittance (left). Blue dye was added to water for visual clarity. A

goniometer image of a deposited water droplet is shown on right (Ebert and Bhushan, 2016). 118

Figure 47: Surface height maps and sample surface profiles (locations indicated by arrows) for before and after AFM wear experiment using 15- μm radius borosilicate ball at loads of 1 μN and 10 μN for PDMS samples etched by O_2/CF_4 for 15 min with subsequent C_4F_8 plasma treatment. RMS roughness and PV distance values for surface profiles are displayed within surface profile boxes (Ebert and Bhushan, 2016). 124

CHAPTER 1: Introduction

1.1 Significance of the problem

Surface wettability is of crucial importance as the vast potential of nanotechnology begins to permeate many areas of modern life. Wetting of surfaces has been studied as far back as the 19th century, but only since the inventions of the atomic force microscope (AFM) and scanning electron microscope (SEM) in the 1980s has it been possible to study the nanoscale mechanisms involved, which play a role in many extreme wetting behaviors. For example, it was discovered that a dual-scale roughness of micro- and nanosized bumps is responsible for the remarkable water repellency and self-cleaning ability of the Lotus leaf. Nanotechnology now allows us to imitate these natural phenomena (an endeavor known as “biomimetics”) to create surfaces with extreme wetting characteristics that are of growing engineering interest.

As nanotechnology develops, surface properties are of ever-increasing interest to engineers and scientists. Since surface forces dominate at small length scales, careful study and optimization of these properties is required. In particular, the affinity for water to spread on or repel from a surface becomes a central design parameter in many applications, such as in microchannels in MEMS devices, where fluid drag tends to be very high. As research in biosensors, lab-on-chip technology, and other microdevices

progresses, manipulation of small droplets and intelligent control of fluid flow will be paramount.

The importance of surface wettability, however, is not limited to the realm of the very small. Contamination of surfaces is a potentially expensive problem, in terms of energy, money, resources, and labor. The ability of some surfaces with extreme wetting to resist contamination leads to the possibility of self-cleaning windows, anti-biofouling watercraft, and improvement of high-performance optics. Design and control of surface wettability can provide durable, passive solutions to these problems as opposed to continuous, active solutions (such as repeated cleaning) that require sustained inputs of energy.

1.2 Overview of surface wettability and superhydrophobicity

Water is a polar molecule with high surface energy. As such, it has a greater affinity for surfaces with high surface energy. A simple measure of a water droplet's affinity for a surface is its contact angle, or the angle the edge of the droplet makes with the surface. On a hydrophilic ("water-loving") surface with high energy, a droplet tends to spread and the contact angle is low (less than 90°). On a hydrophobic ("water-fearing") surface with low energy, a droplet tends to bead up and the contact angle is high (greater than 90°).

Figure 1 illustrates contact angle for hydrophilic and hydrophobic surfaces. On a flat surface, the contact angle (CA) can be determined theoretically in terms of surface tensions by the Young Equation:

$$\gamma_{SG} = \gamma_{SL} + \gamma_{LG} \cos\theta \quad (1)$$

where θ is the contact angle and the γ -values are the surface tensions at the solid-gas (SG), solid-liquid (SL), and liquid-gas (LG) interfaces.

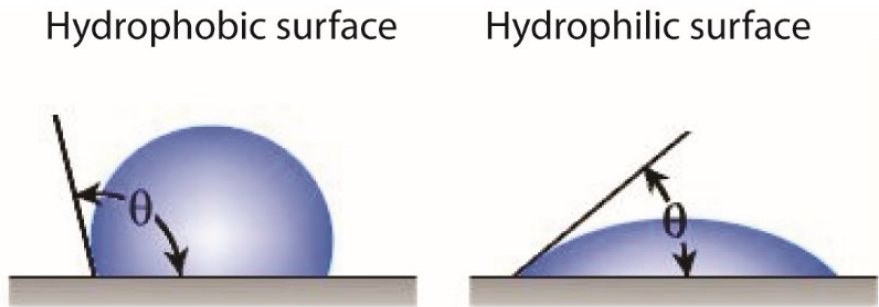


Figure 1: Illustration of hydrophobic and hydrophilic surfaces with contact angle θ

Equation (1) assumes a perfectly flat surface for which the CA depends entirely on surface chemistry. However, surface roughness plays a vital role in wettability. For a rough surface, two basic wetting regimes are seen for a deposited water droplet. In the Cassie-Baxter state, the bottom of the droplet rests on the tops of the surface asperities, with air trapped in the cavities between asperities (Cassie and Baxter, 1944). In the Wenzel state, the liquid fully penetrates the cavities, resulting in a continuous liquid-solid interface with no trapped air (Wenzel, 1936). **Figure 2** illustrates the Wenzel and Cassie-Baxter wetting states. For a surface with uniform roughness and homogeneous surface chemistry, the CA can be predicted by the Wenzel Equation (Bhushan, 2016), given as:

$$\cos \theta = R_f \cos \theta_0 \quad (2)$$

where θ is the apparent CA, θ_0 is the CA on a flat surface of the same surface energy, and R_f is the roughness factor, defined as the ratio of the true area of the solid-liquid interface

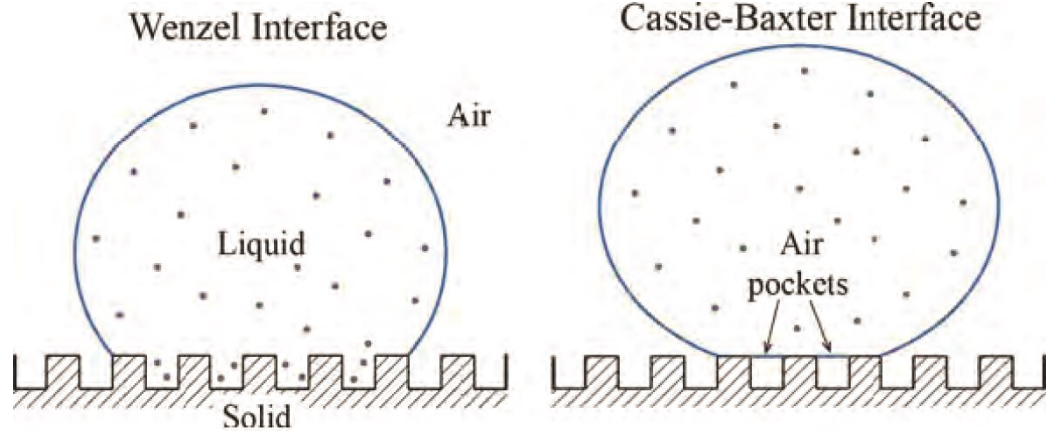


Figure 2: Schematics of a Wenzel wetting interface (full wetting) and a Cassie-Baxter wetting interface (composite with air pockets) (adapted from Bhushan, 2016)

to its two-dimensional projection. Since the roughness factor amplifies the cosine of the CA, the CA itself is predicted to increase for flat-surface angles greater than 90° , and decrease for angles less than 90° . In other words, roughening has the effect of making a hydrophobic surface more hydrophobic, and a hydrophilic surface more hydrophilic.

Superhydrophilic plant surfaces found in nature, as will be discussed in section 1.3, exploit this phenomenon. Broadly speaking, superhydrophilicity relies on a 3-D or 2-D capillary effect (seen when surface tension and adhesive forces are sufficient to propel a liquid) on a hydrophilic material (Sun *et al.*, 2004). Roughening of a hydrophilic surface can create a capillary effect for quick water spreading, and reduces the static CA in accordance with the Wenzel Equation (Eq. 2). Superhydrophilic surfaces have been fabricated in a number of ways. Liu *et al.* (2007, 2008) created surfaces through use of

porous films and self-assembly of nanospheres. Others have taken advantage of the photocatalytic effect of titania (in which exposure to UV light essentially changes the surface chemistry of titania particles on surface) to enhance hydrophilicity (Watanabe *et al.*, 1999; Sakai *et al.*, 2001). Superhydrophilic surfaces are of growing interest due to several potential properties, such as self-cleaning, anti-fogging, and high adhesion (Patel *et al.*, 2010; Bhushan and Jung, 2008). These properties have many industrial applications, including anti-fogging glass, sticky or highly adhesive surfaces, and in pressure-free liquid transport in microchannels, due to strong capillary forces (Koch and Barthlott, 2009).

The effect of roughness for an initially hydrophobic surface is shown in **Fig. 3**. If the interface is composite (containing both solid-liquid and liquid-air components), the CA can be predicted by the Cassie-Baxter Equation (Bhushan, 2016):

$$\cos \theta = R_f \cos \theta_0 - f_{LA} (R_f \cos \theta_0 + 1) \quad (3)$$

where f_{LA} is the fraction of the composite interface that is solid-liquid. The equation predicts that the CA of any surface will increase with increasing f_{LA} . In fact, an initially hydrophilic surface can be made hydrophobic if roughening results in sufficiently high f_{LA} . Roughening of a surface can give rise to CA values above 150° (termed “superhydrophobic”), whereas the highest observed CAs on hydrophobic flat surfaces are around 120° (Nishino *et al.*, 1999).

Another important parameter in characterizing the wetting of a surface is the contact angle hysteresis (CAH), which is the difference in the advancing and receding contact angles for a moving droplet. CAH is shown schematically in **Fig. 4**. Contact angle

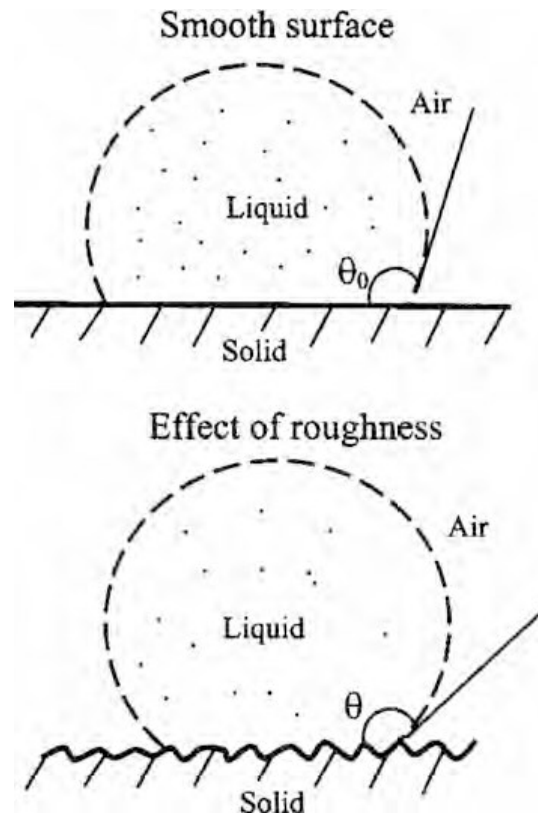


Figure 3: Schematic of a liquid droplet in contact with a smooth solid surface (contact angle θ_0) and with a rough solid surface (contact angle θ) (Bhushan, 2016)

hysteresis can be described as energy dissipation. The primary factors that contribute to it are adhesion hysteresis, surface roughness, and chemical heterogeneities. In order for a droplet to move along a surface, the so-called “triple line” formed by the intersection of the solid, liquid, and air must move. Surface roughness necessitates contortion of the triple line as it moves between local states of minimum free energy, and there is an energy barrier associated with moving between any two local minima. In addition, sharp edges can have the effect of pinning the triple line, as the local contact angle will be

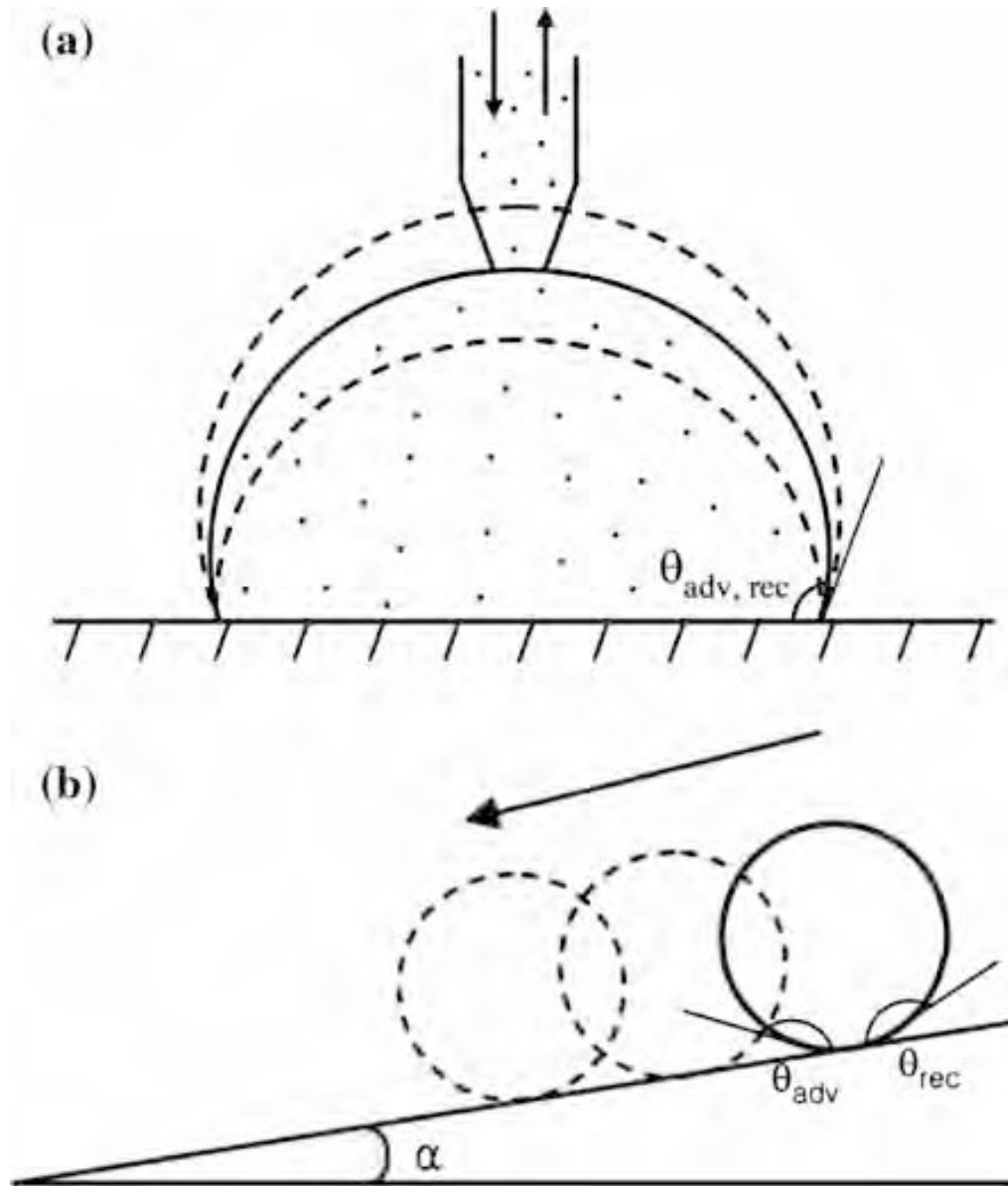


Figure 4: (a) Droplet in contact with a rough surface with liquid added or removed (advancing and receding contact angles are θ_{adv} and θ_{rec} , respectively) and (b) tilted surface profile (tilt angle α with a moving liquid droplet). The contact angle hysteresis (CAH) is defined as $\theta_{adv} - \theta_{rec}$ (Bhushan, 2016)

intermediate to the contact angles on the two planes forming the sharp edge. Chemical heterogeneities have a similar effect of causing triple line contortion for free energy minimization. However, contact angle hysteresis will exist even on an atomically smooth, chemically homogeneous surface due to adhesion hysteresis: the energy required to separate the liquid-solid interface is greater than the energy gained by forming the interface. When CAH is high, a droplet tends to slide on a tilted surface. However, when CAH is very low, droplets tend to roll, maintaining a more spherical shape. Droplets tend to have low CAH when the liquid-air fraction is high in the Cassie-Baxter state, since the low adhesion of liquid to air as opposed to liquid to solid allows easy motion of the droplet.

Transition from the Cassie-Baxter (composite) to the Wenzel (fully-wetted) regime can occur, but the reverse is never observed (Jung and Bhushan, 2007). If the distance between surface asperities is too large, the droplet will droop low enough to contact the solid surface between them. Therefore, surface geometry and droplet size are important factors in the wetting transition. In addition, droplet impact velocity, condensation of nanodroplets between asperities, and standing capillary waves can decrease the stability of the composite interface and aid in the transition to the Wenzel state. Since many of the potential destabilizing factors occur on different characteristic length scales, a surface with multiscale (or hierarchical) roughness could serve to guard against these factors (Nosonovsky and Bhushan, 2007). The term “hierarchical” in regard to roughness will be used hereafter to mean a multiscale roughness, typically where nanoscale roughness is

superimposed onto microscale roughness. **Figure 5** illustrates surfaces with different roughness types: flat, microstructured, nanostructured, and hierarchically structured.

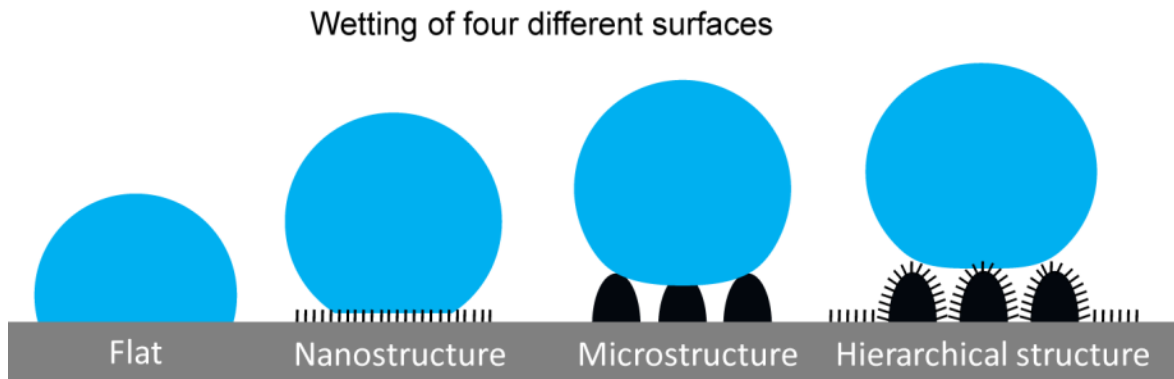


Figure 5: Schematic of four different surface structure types and their wetting behaviors.

The largest contact area between the droplet and the surface occurs on flat and microstructured surfaces, but is reduced on nanostructured surfaces and minimized on hierarchically structured surfaces (Jung and Bhushan, 2009).

The Wenzel and Cassie-Baxter models apply to surfaces with uniform roughness and surface chemistry. Recently, however, experimental data have shown that for non-uniform surfaces, conditions at the triple line (solid-liquid-air interface) determine the contact angle (Gao and McCarthy, 2007). In other words, roughness and/or surface energy under the central bulk of the droplet do not affect CA. However, for droplets in the Cassie-Baxter regime, many internal triple lines exist inside the droplet perimeter, and are thought to impact wettability (McHale, 2007). Generalized theories of surface wetting

intended to resolve these issues are still being developed (Nosonovsky and Bhushan, 2008, Bormashenko, 2011).

The very high apparent CA associated with ultra-repellency of liquids is in fact a macroscale phenomenon caused by amplification of the solid-liquid interface (due to roughness) and/or the liquid-air fraction of the interface. At a scale smaller than the roughness features, the true CA approaches the CA of the liquid on a flat surface. Liquids with low surface tension (and correspondingly low flat-surface CA) will tend to penetrate between asperities and wet the surface more easily (Bhushan, 2011). Thus, the geometry of roughness asperities can become an important factor for wettability. When the flat-surface CA is less than 90° , a so-called re-entrant geometry is typically required to maintain a Cassie-Baxter state. When flat surface CA is close to 0° , a doubly re-entrant geometry is needed (Brown and Bhushan, 2016). **Figure 6** shows non-re-entrant, re-entrant, and doubly re-entrant geometries supporting non-wetting for liquids of different flat surface CA (θ_{flat}) (Ebert and Bhushan, 2016).

Surfaces that are ultra-repellent to liquids of nearly any surface tension are often referred to as superomniphobic. Much attention has been given to the ultra-repellency of oils (superoleophobicity) for applications such as anti-smudge coatings for electronic device screens and reduction of drag in oil pipelines (Bhushan, 2016; Brown and Bhushan, 2016). There is a wide range of surface tension values among different oils, which can dictate, among other things, the geometry required for surface asperities. Therefore, to deem a surface superoleophobic, as compared to superomniphobic or

Surface geometries supporting non-wetting for different θ_{flat}

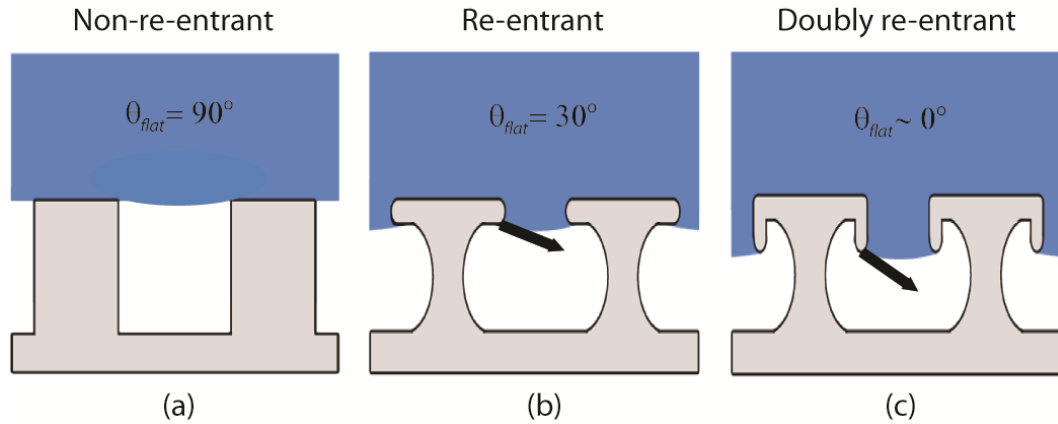


Figure 6: Schematic examples of (a) non-re-entrant surface geometry supporting non-wetting by liquid for flat surface CA of 90° , (b) re-entrant geometry supporting non-wetting for flat surface CA of 30° , and (c) doubly re-entrant geometry supporting non-wetting for flat surface CA of $\sim 0^\circ$ (Ebert and Bhushan, 2016)

superhydrophobic, is not particularly informative unless a minimum surface tension of the oils repelled is given. Due to low surface tension of many oils leading to low flat-surface CA, superoleophobicity typically requires re-entrant (and sometimes doubly re-entrant) geometry, often in tandem with minimization of surface energy by means of fluorination. These complex geometries are inherently difficult to fabricate, and are typically fragile, making them prone to mechanical wear and failure. Brown and Bhushan (2015) created surfaces that achieved CA of 155° for hexadecane (surface tension = 27 mN/m) with a layer-by-layer approach using a polyelectrolyte binder, SiO_2 nanoparticles, and a fluorosurfactant. The surfaces exhibited some optical transmittance, a higher degree

of durability than has been reported in many existing studies, and an oil-water separation capability.

Since the mechanisms of the Lotus Effect were discovered, interest has grown substantially in creating biomimetic superhydrophobic surfaces. Superhydrophobic surfaces have potential in a number of industrial applications. One of the more obvious examples is the development of self-cleaning materials, such as paints and other coatings, which could eliminate the labor and energy costs associated with maintenance. A schematic of the self-cleaning effect on a Lotus-like surface is given in **Fig. 7**. Of particular interest is the prospect of superhydrophobic coatings on glass, which could give rise to self-cleaning windows but which requires optical transparency of the coating. Transparent, superhydrophobic surfaces are also of keen interest for many other applications such as photovoltaics and optical devices. However, the multiple requirements of optical transparency and superhydrophobicity pose a unique challenge: the surface must be sufficiently rough for a high CA and low CAH, but the dimensions of the roughness features must be small enough to preserve high transmittance (typically on the order of the wavelength of visible light) (Zhang *et al.*, 2008). Design of superhydrophobic surfaces that require high optical transmittance often requires development of different and novel fabrication techniques due to the additional constraints. Research on these techniques is therefore necessary to realize the potential benefits of such surfaces, such as a self-cleaning ability for windows.

A superhydrophobic surface also has the potential to prevent ice formation, or to have a very low adhesion to ice that has formed. Ice formation is a significant problem for aviation, power infrastructure, and automotive safety. Ice adheres to materials mainly

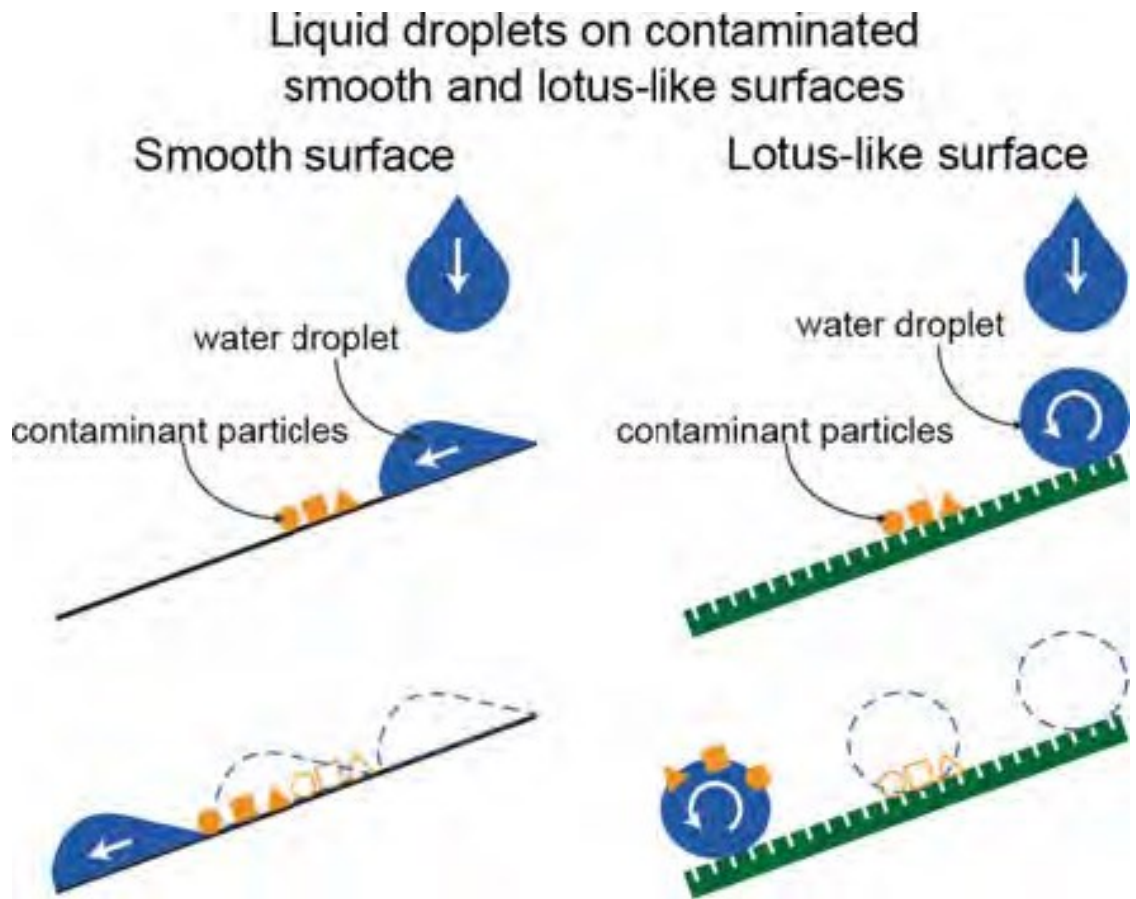


Figure 7: Schematic showing a droplet sliding on a smooth surface, leading to redistribution of contaminant particles, and a droplet rolling on a lotus-like surface with low contact angle hysteresis and low adhesion/drag, removing contaminant particles from the leaf surface (Bhushan, 2016)

due to electrostatic interactions between polar ice molecules and the solid surface at the solid-ice interface (Petrenko and Peng, 2003). Kulinich and Farzaneh (2009) found that a high CA is not enough for an anti-icing surface, and that CAH has a much stronger correlation with ice adhesion strength. Tourkine *et al.* (2009) showed that the time required for a droplet to freeze was greater in Cassie-Baxter wetting on a rough surface compared to a flat surface, and suggested that the high proportion of liquid-air interface acts as insulation to delay freezing. Mishchenko *et al.* (2010) showed that with proper structure size, superhydrophobic surfaces could prevent ice formation at temperatures below the freezing point of water by repelling droplets before ice nucleation can occur. However, literature on the performance of superhydrophobic surfaces at freezing temperatures is still somewhat sparse (Kulinich and Farzaneh, 2009).

1.3 Biomimetics and extreme wettability found in nature

Billions of years of evolution have produced finely tuned, intricate designs that have the effect of increasing the likelihood of survival and reproduction. These designs can provide guidance and inspiration to researchers for engineering applications. The mimicking of designs found in nature is a field broadly referred to as biomimetics.

Figure 8 shows a collection of examples of natural designs that have been studied and mimicked for practical uses, such as shark skin riblets and micropatterned moth eyes.

Many plants exhibit extreme water repellency or other forms of extreme wettability. The most famous example is the leaf of the Lotus plant (*Nelumbo nucifera*), which has CA of about 163° and CAH of 3° (Bhushan and Jung, 2008). Water droplets on the Lotus leaf

Montage of living nature examples inspiring field of biomimetics

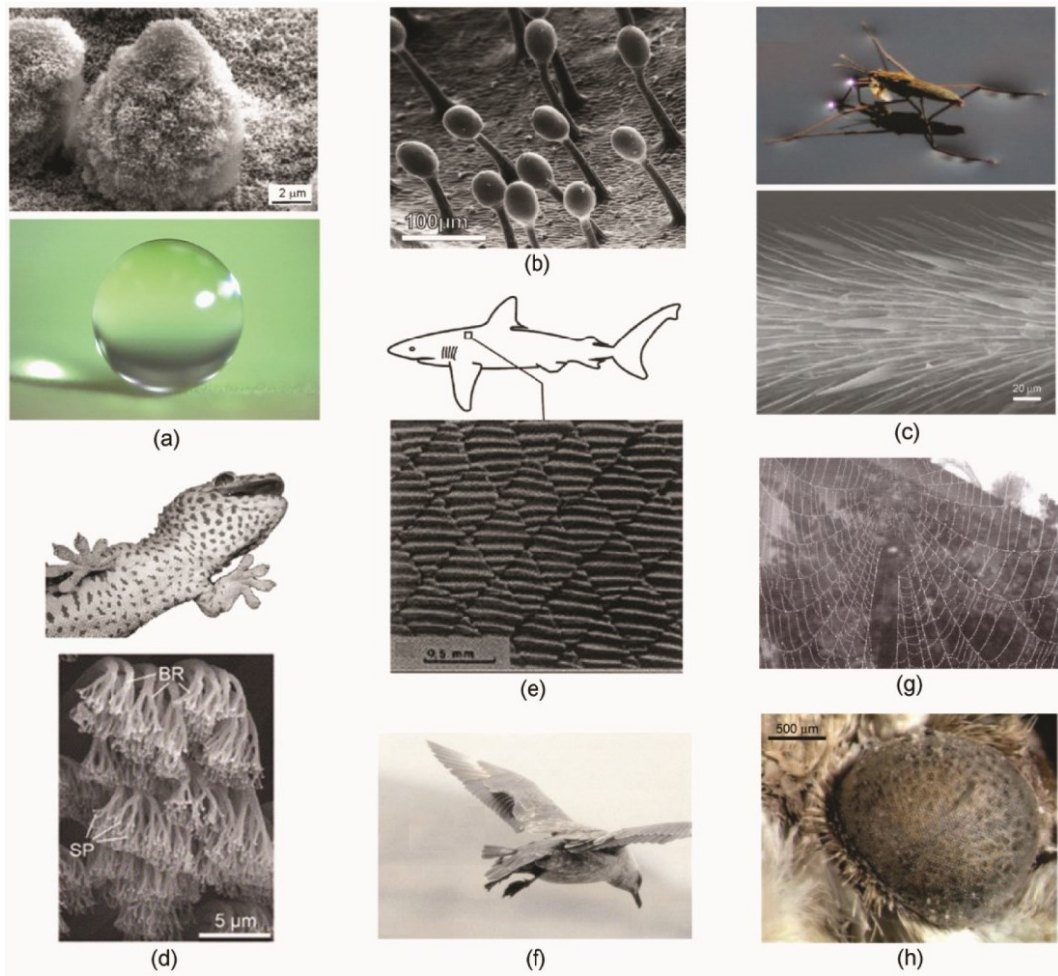


Figure 8: Examples from nature that have inspired researchers developing new products (adapted from Bhushan, 2009). Shown are (a) water droplet on a self-cleaning Lotus leaf and its micropapillae, (b) glands of carnivore plant that trap insects, (c) water strider walking on water and its leg structure, (d) Gecko feet spatula with reversible adhesion, (e) riblet-covered low-drag and antifouling shark skin, (f) bird wing structure and orientation during landing approach, (g) spider webs made of silk strands, and (h) antireflective moth eyes.

remain nearly spherical and roll away almost effortlessly, a phenomenon known as the “Lotus Effect.” The low CAH also results in the removal of contaminants from the leaf’s surface as the droplet rolls off of it, known as the “self-cleaning effect.” The Lotus leaf’s superhydrophobic properties are due to its dual-scale (micro- and nanoscale) roughness. The microscale roughness is formed by convex cell papillae, and the nanoscale roughness by hydrophobic wax tubules (Barthlott and Neinhuis, 1997). **Figure 9** shows a scanning electron microscope (SEM) image of the surface of a Lotus leaf.

The red rose petal (*rosea Rehd*) is another example of a surface in nature that exhibits superhydrophobicity. However, in contrast to the Lotus leaf, on which droplets roll away at only a few degrees tilt, droplets on the rose petal remain adhered even when the petal is turned upside down. Optical micrographs of droplets on the surface of the rose petal *Rosa, cv. Bairage* can be seen in **Fig. 10**. This combination of superhydrophobicity with high adhesion is known as the “Rose Petal Effect” or “Petal Effect” (L. Feng *et al.*, 2008). The reason for this unique wetting behavior is that an applied water droplet on a rose petal resides in a special wetting regime known as the “impregnating state” (Feng *et al.*, 2008). In this state, liquid is able to penetrate between the microstructures, but is unable, or only partially able, to penetrate the nanostructures. Like the Lotus leaf, the red rose petal has a hierarchical structure with both micro- and nanoscale surface features. However, the microstructure of the red rose petal has a higher average pitch value and lower height than that of the Lotus leaf, allowing liquid to more easily penetrate the

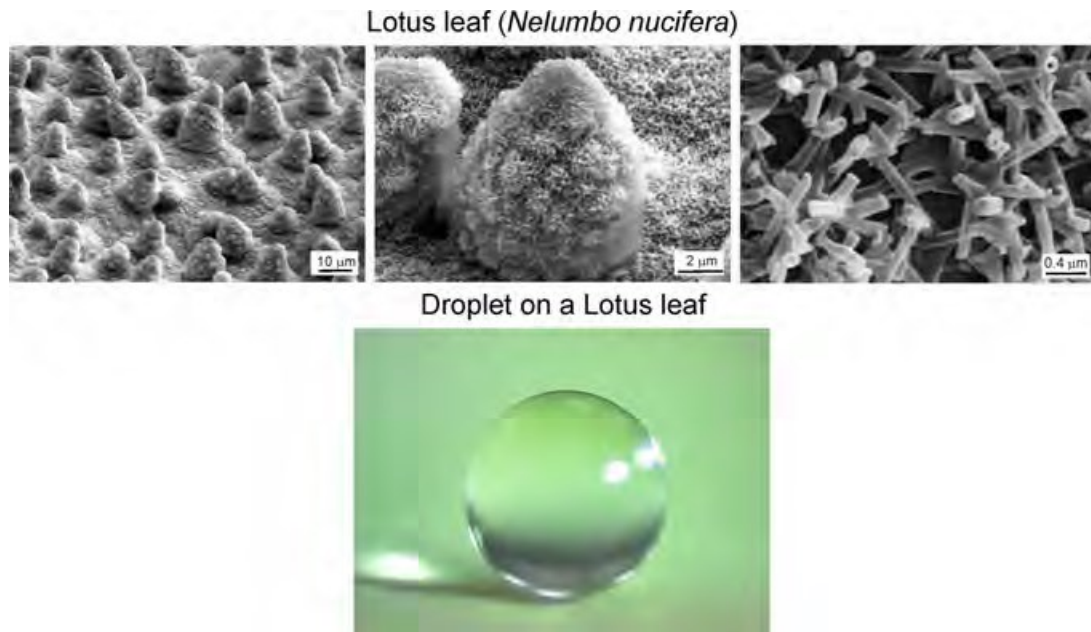


Figure 9: SEM micrographs (shown at three magnifications) of a lotus (*Nelumbo nucifera*) leaf surface, consisting of microstructure formed by papillose epidermal cells covered with 3-D epicuticular wax tubules on surface, which create nanostructure, and an image of a water droplet sitting on a lotus leaf with a contact angle of about 164° (Bhushan *et al.*, 2009)

microstructure. In addition, a lower nanostructure density is believed to play a role, as an increased degree of penetration of the nanostructure leads to increased wetted area and therefore higher droplet adhesion (Bhushan and Her, 2010). **Figure 11** shows a scanning electron microscope (SEM) image of the surface of *Rosa, cv. Bairage*.

The mechanisms behind the Rose Petal Effect were discovered much more recently than those of the Lotus Effect, and fewer attempts have been made to fabricate Rose Petal

Droplet on Rosa, cv. Bairage

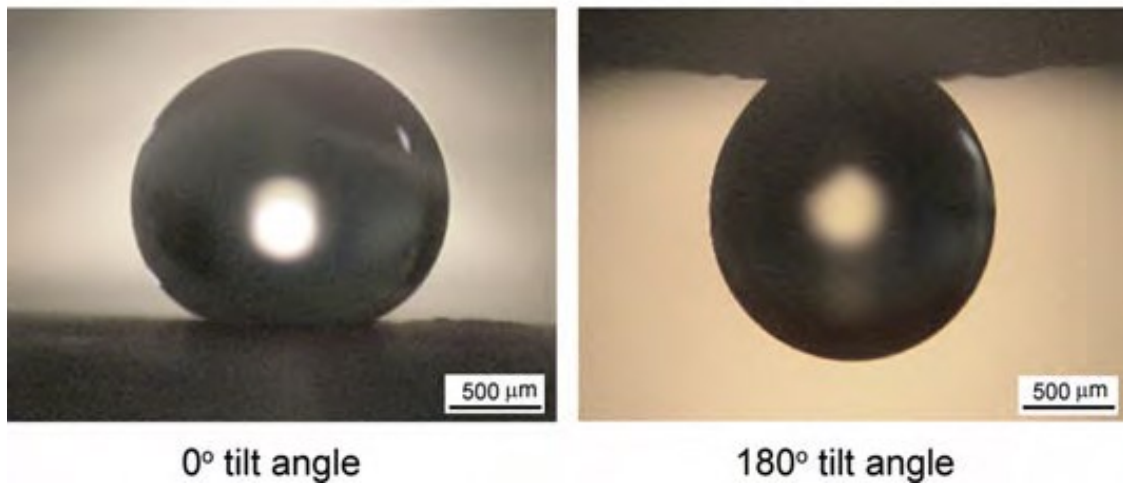
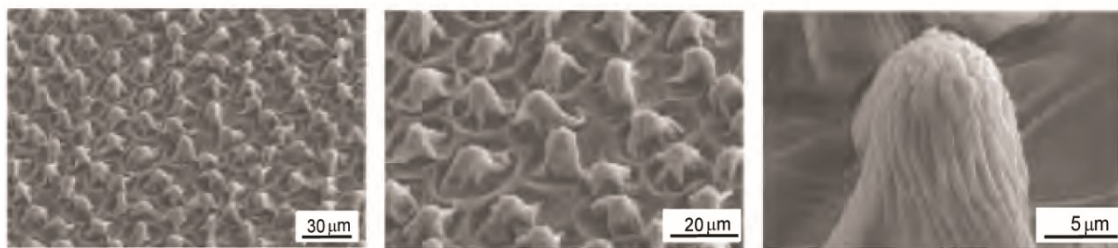


Figure 10: Optical micrographs of water droplets on Rosa, cv. Bairage at 0° and 180° tilt angles. Droplet is still suspended when the petal is turned upside down (adapted from Bhushan and Her, 2010).

Superhydrophobic rose petal with high droplet adhesion



Rosa, cv. Bairage (dried)

Figure 11: SEM images of Rosa, cv. Bairage at three magnifications (adapted from Bhushan and Her, 2010)

Effect surfaces exhibiting high CA and high droplet adhesion. The Rose Petal Effect state has several potential applications, including transportation of small droplets (a kind of “mechanical hand”), and pinning of droplets for *in situ* detection and localized chemical reaction (K. Liu *et al.*, 2010; M. Liu *et al.*, 2010).

Surfaces with very low CA (typically less than 10°) are referred to as “superhydrophilic”. A flat surface with high surface energy results in CAs less than 90°, as the spreading of a water droplet is energetically favorable. Certain plant species have evolved superhydrophilic leaves or other organisms for varying survival purposes. Some have evolved to remain permanently wetted, such as plants that grow underwater. These surfaces tend to be very smooth and free of wax structures. Other plants utilize structures that are meant to absorb water, typically involving pores (as in *Sphagnum* moss) or thin hairs (as in Spanish moss). Still other plants have developed surfaces capable of spreading water rapidly across themselves. Many of these surfaces employ an evenly spaced microstructure of hydrophilic material. In some species, it seems to be a design feature that allows them to trap insects, as in many carnivorous plants. In others, it may be a way to quickly maximize the liquid-air interface for faster evaporation (Koch and Barthlott, 2009). **Figure 12** shows SEM micrographs of the surfaces of several different types of superhydrophilic leaves and mosses (Koch and Barthlott, 2009).

1.4 Scope of the thesis

In the following chapters, the results of a set of studies exploring the fabrication and characterization of mechanically durable superhydrophobic surfaces will be presented

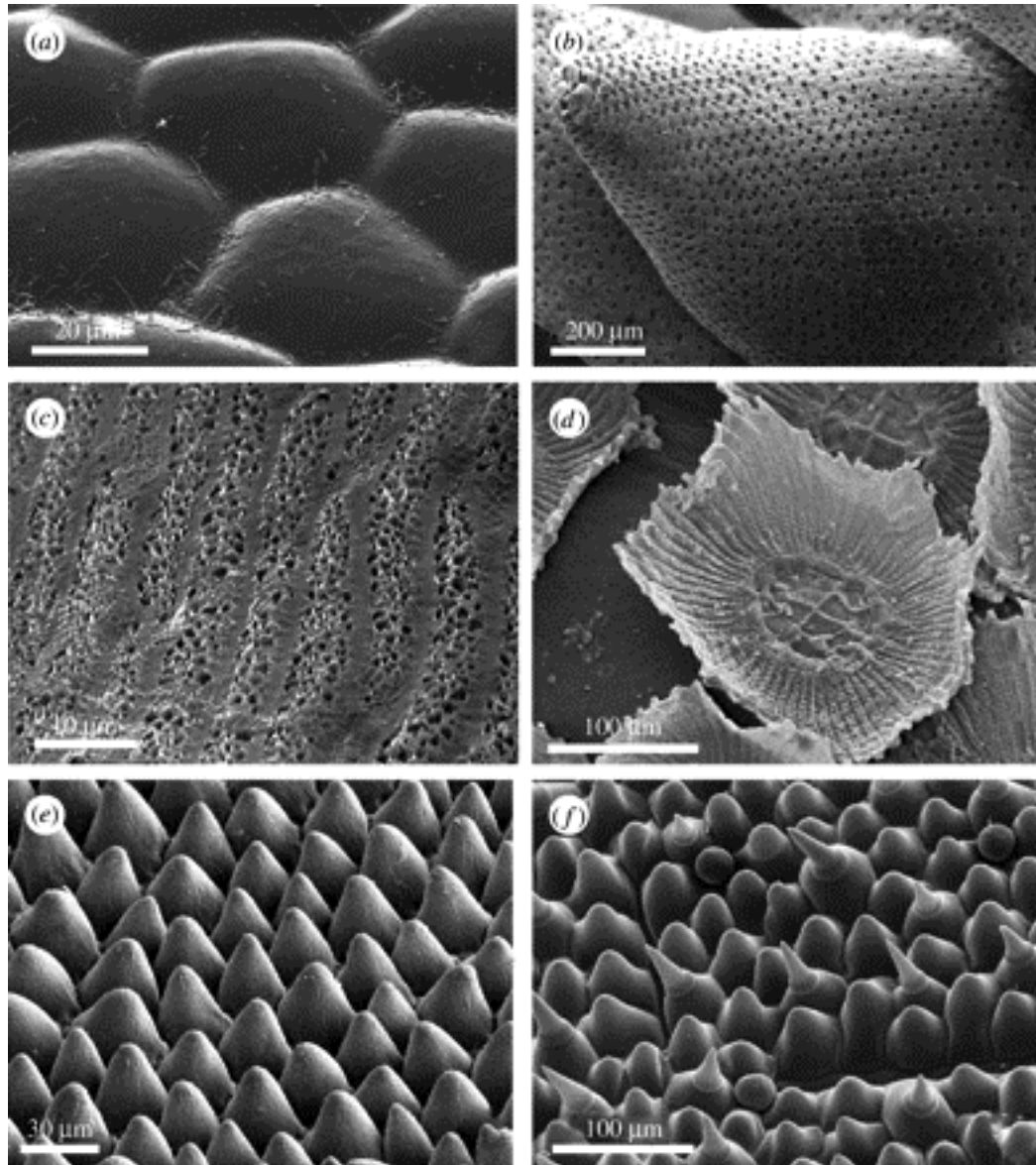


Figure 12: SEM micrographs of superhydrophilic leaves and mosses (Koch and Barthlott, 2009). (a) Water plant *Anubias barteri* with unstructured, flat surface. (b) Surface of water-absorbing moss *Sphagnum squarrosum*. (c) Porous structure of *Rhacocarpus purpurescens* moss formed by epidermal cells. (d) Water-absorbing hairs of Spanish moss *Tillandsia usneoides*. (e) *Calathea zebrine* leaf surface with conical cells. (f) *Ruellia devosiana* leaf surface employing different cell types.

and discussed. These studies are inspired in part by phenomena witnessed in nature, in particular the Lotus Effect and Rose Petal Effect. The motivation of this work is to achieve the benefits of these effects (for example, self-cleaning in the case of the Lotus Effect) for engineering purposes. Two broad objectives of the work can be summarized as follows: The first objective is to study the effects of micro- and nanoscale geometry and roughness parameters and surface chemistry with regard to wettability and, in some cases, optical transmittance. This is done in order to optimize surface design for the desired biomimetic effects. The second broad objective is to determine materials and fabrication techniques that result in mechanically durable surfaces that are simple to manufacture.

Chapter 2 examines the design of hierarchically structured, Lotus-inspired surfaces using different sized particles, with comparison of the use of particles versus a uniform epoxy micropattern to form the underlying microstructure. Wettability is examined across a range of microstructure pitch values with particular focus on the Cassie-Baxter to Wenzel regime transition, which is undesirable. Chapter 3 introduces another wetting regime intermediate to Cassie-Baxter and Wenzel that is responsible for the Rose Petal Effect (superhydrophobic with high droplet adhesion). The chapter expands upon the concept of hierarchical design and examines the tuning of the nanostructure density and surface energy in order to achieve superhydrophobic surfaces with both high and low droplet adhesion. The effectiveness of using hydrophobic versus hydrophilic nanoparticles, as well as the required geometric spacing and roughness values required in

each case, are discussed. Chapter 4 examines the design of superhydrophobic surfaces with high optical transmittance. Optical transmittance is an important requirement for applications such as self-cleaning windows and solar panels. A novel dip-coat technique (U.S. Patent Pending) is used to form highly transparent coatings on glass and polymer substrates using three different types of nanoparticles, exhibiting high versatility of the technique. The effects of particle size and inherent optical properties of the particles and substrates are examined in regard to fabricating surfaces that simultaneously exhibit superhydrophobicity and high transmittance, which are competing goals in terms of the degree of roughness required to achieve them. In Chapter 5, superhydrophobic surfaces with high transmittance are fabricated without the use of particles by using a reactive ion etching (RIE) procedure on polydimethylsiloxane (PDMS) substrates to create roughness on the surface through highly anisotropic etching. The use of particles to create surface roughness may not be ideal in all cases, and thus techniques should be explored to fabricate superhydrophobic surfaces by creating roughness in the bulk material itself. The effect of surface roughness on surface wettability and transmittance is examined, as well as two different surface post-treatment methods aimed at further reducing the surface energy. In all studies, the mechanical wear resistance and durability of samples is investigated using AFM, and in some cases using ball-on-flat tribometer and/or a water jet procedure. Chapter 6 concludes the thesis by providing a summary and an outlook for future work.

CHAPTER 2: Lotus Effect Surfaces with Superhydrophobicity and Low Droplet

Adhesion

2.1 Introduction

The leaf of the Lotus plant (*Nelumbo nucifera*) has a hierarchically structured surface, which is responsible for its superhydrophobic and self-cleaning qualities (Barthlott and Neinhuis, 1997; Koch *et al.*, 2008, 2009a). The microscale roughness is formed by convex cell papillae, and the nanoscale roughness is formed by hydrophobic wax tubules. The Lotus leaf has a contact angle (CA) of 164° and contact angle hysteresis (CAH) of 3° . The very low CAH value allows a water droplet to roll off the surface instead of slide, taking contaminants along with it. A hierarchical structure allows for increased formation and stability of air pockets, reducing the contact area of an applied water droplet with the surface. This results in low CAH, tilt angle, and adhesive force (Patankar, 2004; Bhushan and Jung, 2008; Li and Amirfazli, 2008; Nosonovsky and Bhushan, 2008; Bhushan *et al.*, 2009).

Synthetic surfaces inspired by the Lotus leaf have been fabricated using a number of techniques, such as soft lithography, self-assembly, electrodeposition, and imprinting (Shirtcliffe *et al.*, 2004; Ming *et al.*, 2005; Sun *et al.*, 2005; Chong *et al.*, 2006; del Campo and Greiner, 2007; Cortese *et al.*, 2008; Zhao *et al.*, 2008; Bhushan *et al.*, 2009;

Koch *et al.*, 2009b; Kuan *et al.*, 2009). For industrial applications, these surfaces must possess mechanical durability. For applications such as windows or self-cleaning toilets, surfaces must retain superhydrophobicity after impingement of water. Durable, Lotus Effect surfaces have previously been created, among other methods, by depositing carbon nanotubes (CNTs) onto epoxy micropatterns (Jung and Bhushan, 2009).

The motivation of this study was to fabricate durable, superhydrophobic surfaces with self-cleaning ability by imitating the hierarchically structured surfaces seen on the Lotus leaf. The objectives were to use hydrophobic SiO₂ particles of different sizes for both micro- and nanoscale roughness to create mechanically wear-resistant, Lotus Effect surfaces, and to examine the use of microparticles versus uniform micropatterns as a means to create the microstructure. Superhydrophobic surfaces using SiO₂ particles have been created by dropcasting, chemical deposition and sol-gel processes (Ming *et al.*, 2005; Liu *et al.*, 2006; Englert *et al.*, 2006). In this study, hierarchical structures resistant to mechanical wear were created with SiO₂ particles using a simple spray process. First, SiO₂ nanoparticles of two different sizes were deposited onto micropatterned surfaces to confirm superhydrophobicity and low CAH. Then, SiO₂ microparticles were substituted for the micropattern to create the microscale roughness. The pitch between pillars for the micropatterns is known, and the average pitch between microparticles on a surface can be determined through SEM imaging. The CA and CAH behaviors of micropatterns and surfaces with microparticles are examined across a range of pitch values to compare the use of microparticles and micropatterns. Hierarchical surfaces were also created using a combination of microparticles and nanoparticles. Wear experiments were conducted for

the microparticles and nanoparticles using an atomic force microscope (AFM), a ball-on-flat tribometer, and a water jet apparatus. In all experiments, the wear of an epoxy resin on a flat surface is used as a benchmark for comparison.

2.2 Overview of wettability on a patterned surface

Combining roughness on both the micro- and nanoscale results in a hierarchically structured surface, which is the basis of the Lotus Effect. As seen in **Fig. 5** in section 1.2, the lowest area of contact between the droplet and the surface occurs in the case of the hierarchical structure, which can be expected to have highest CA and lowest CAH as a result. In addition, the multiscale roughness allows for more stable air pocket formation, guarding against destabilizing factors on both the micro- and nanoscale.

As discussed in Chapter 1, wetting of a structured surface can be generally described in terms of different wetting regimes, the main two of which are the fully wetted (Wenzel) and composite (Cassie-Baxter) regimes (Wenzel, 1936; Cassie and Baxter, 1944). In the Wenzel regime, the liquid fully penetrates the gaps between asperities. In the Cassie-Baxter regime, the droplet sits on top of the asperities, creating air pockets. The micropatterns used in this study consist of cylindrical pillars with uniform height (H), diameter (D), and pitch (P). The maximum droop of the droplet (δ) between pillars (**Fig. 13**) can be found if these parameters are known. It has been shown that for this geometry, the droop is expected to fully penetrate the air gaps when:

$$\frac{(\sqrt{2}P - D)^2}{R} \geq H \quad (4)$$

where R is the droplet radius (Jung and Bhushan, 2007). This represents the transition from the Cassie-Baxter to the Wenzel regime. For a given height and diameter, the pitch value can be determined above which transition to the Wenzel regime will occur.

Because of the sudden loss of air pockets and increased liquid-solid interface, a droplet that has transitioned to the Wenzel regime can be expected to have lower CA and higher CAH compared to before the transition.

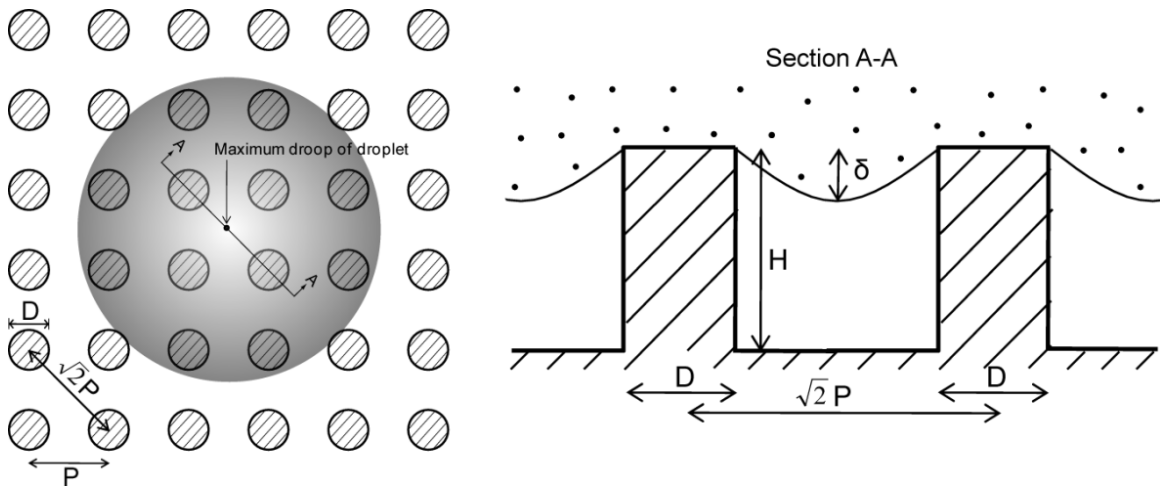


Figure 13: Schematic of a small water droplet suspended on a superhydrophobic surface consisting of a uniform array of cylindrical pillars. The maximum droop of the droplet occurs in the center of the square formed by four pillars (Jung and Bhushan, 2009).

A microstructure can also be formed by depositing microsized particles on a flat surface. **Figure 14** illustrates the use of both particles and a patterned surface to form microstructures and hierarchical structures. Knowing the geometry of the particles,

transition to the Wenzel regime can similarly be predicted to occur above a certain pitch value. If a surface with microparticles is providing an adequate microstructure, it should be expected to exhibit similar trends in CA and CAH with varying pitch as those seen on a uniform micropatterned surface.

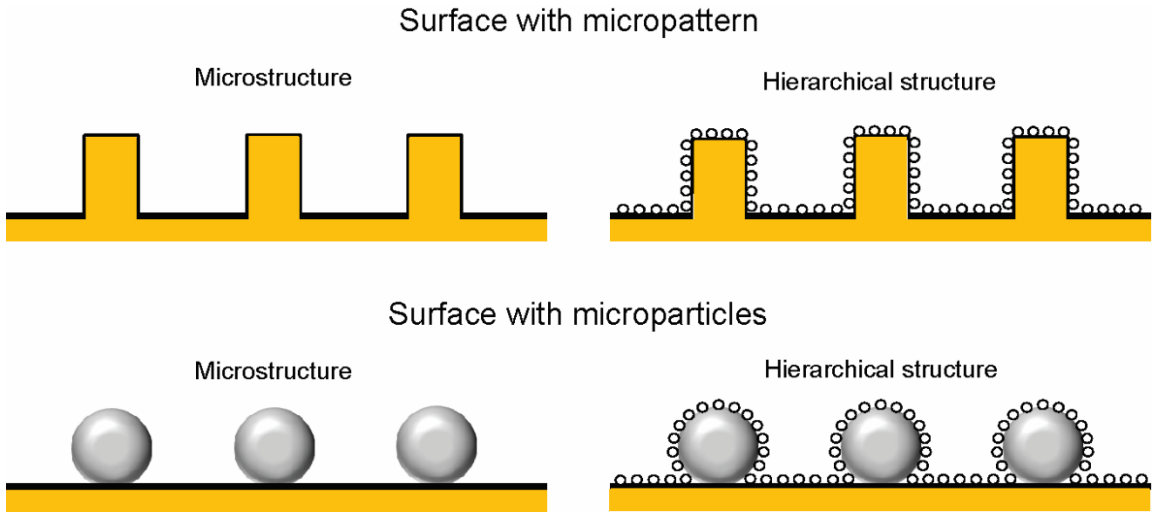


Figure 14: Schematic examples of microstructured and hierarchically structured surfaces in which the microstructure is formed by both a uniform micropattern (top) and microparticles (bottom). In both cases, the hierarchical structure is achieved through addition of nanoparticles (Ebert and Bhushan, 2012a).

2.3 Sample preparation and characterization

2.3.1 Samples using epoxy micropatterns and nanoparticles

Epoxy micropatterns were fabricated by replicating a Si micropatterned surface through soft lithography. This method, shown in **Fig. 15**, has been used by Jung and

Bhushan (2009), in which a negative replica is created using polyvinylsiloxane dental wax, and a positive replica is then made with liquid epoxy. The epoxy is weakly hydrophilic, with a CA of $80^\circ \pm 2^\circ$ for a flat epoxy surface with no micropattern.

Hierarchically structured surfaces using micropatterns were created by depositing nanoparticles onto the micropatterned epoxy substrates using an established spray method (Jung and Bhushan, 2009). The spray method is illustrated in **Fig. 16**. A gravity-feed spray gun was used inside a fume hood to deposit coatings onto samples from a distance of approximately 60 cm.

Surfaces with only a nanostructure were created by spraying particles onto flat substrates. Silica (SiO_2) nanoparticles of 10 nm (± 1 nm) and 50 nm (± 15 nm) were created through continuous flame hydrolysis of SiCl_4 , and hydrophobized through silane treatment (Evonik-Degussa Corporation, Parsippany, New Jersey). In order to spray the particles onto the surfaces, they were first dispersed uniformly in solution. 200 mg of particles were sonicated (dispersed via application of sound energy) in 100 mL of acetone for 4 minutes with a Branson Sonifier 450A with a frequency of 20 kHz at 80% amplitude. For strong bonding of the nanoparticles to the substrates, 200 mg of EPON epoxy resin 1002F (Hexion Specialty Chemicals, Columbus, Ohio) was then added, and the solution was sonicated for another 4 minutes. The dispersion of particles in solution was then sprayed onto the sample surface using a spray gun. The samples were then annealed at 120°C for 3 hours. Annealing at this temperature (above the melting point and below the burning point of EPON 1002F) was done so that the resin would melt and

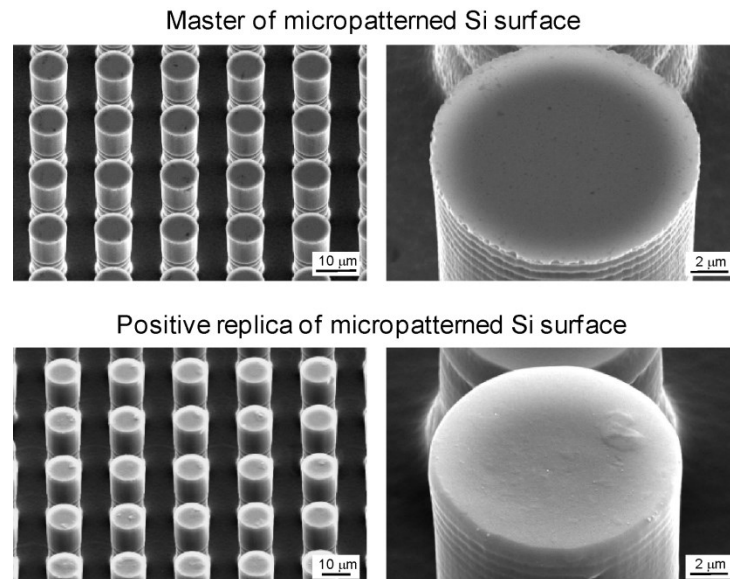
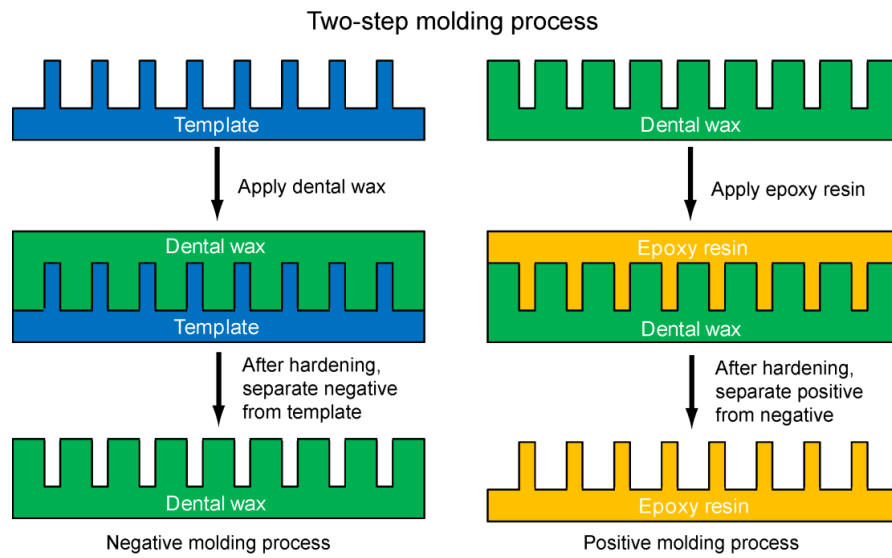


Figure 15: Two-step molding process to create epoxy micropatterns through soft lithography (top), and SEM micrographs of Si master micropattern template and positive replica epoxy micropattern (bottom) (Jung and Bhushan, 2009)

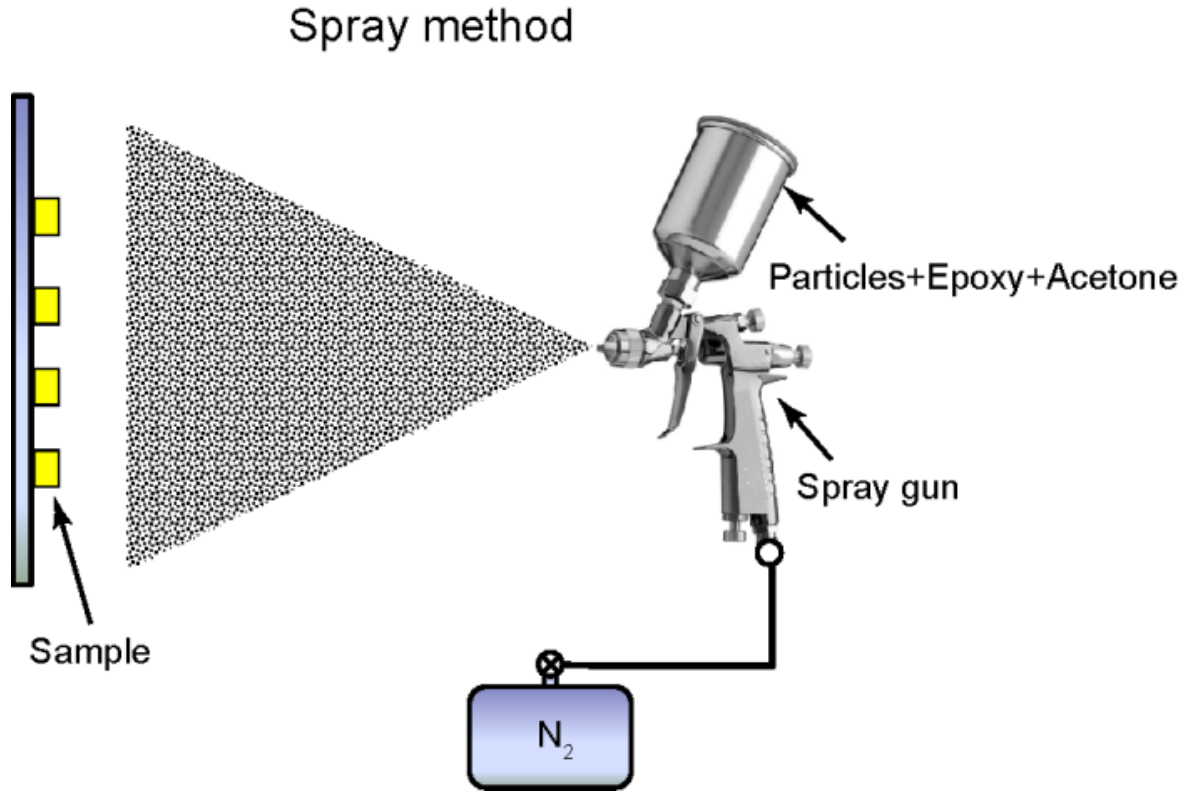
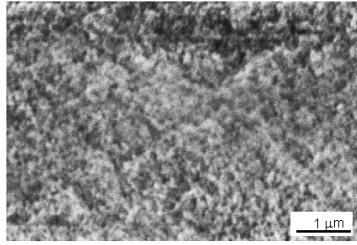


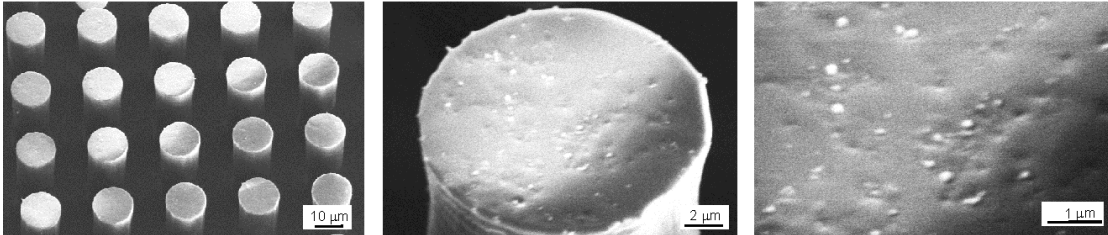
Figure 16: Illustration of spray method to deposit a mixture of SiO₂ micro- and/or nanoparticles, epoxy, and acetone on surfaces (Jung and Bhushan, 2009)

move to the interface between the particles and the surface. **Figure 17** shows the scanning electron microscope (SEM) micrographs of nano-, micro-, and hierarchical structures with SiO₂ nanoparticles and an epoxy micropattern. The micro- and hierarchical structures are shown at three magnifications: the lowest to show pitch between pillars, the middle to show an individual pillar, and the highest to show surface nanoscale roughness.

10 nm particles on flat surface



Micropattern (D = 14 μm , H = 30 μm , P = 23 μm)



10 nm particles on micropattern

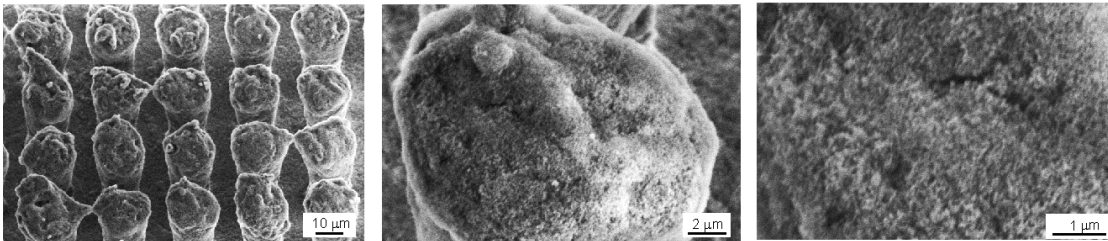


Figure 17: SEM micrographs taken at 45° tilt angle showing 10 nm particles on flat surface at high magnification (top), epoxy micropattern at three magnifications (middle) and 10 nm particles on micropattern at three magnifications (bottom) (Ebert and Bhushan, 2012a)

2.3.2 Samples using micro- and nanoparticles

For samples using microparticles as the microscale roughness, the microparticles were sonicated in solution in the same manner and sprayed onto flat epoxy surfaces. For hierarchically structured surfaces, an additional sonication and spray of nanoparticles was

performed. Surfaces of varying pitch were created by changing the concentration of microparticles in the solution. The value of the average pitch between microparticles was found by determining the number of particles in a 1 mm^2 area in five different locations on the sample by examining SEM images. The hydrophobic SiO_2 microparticles (diameter = $10 \text{ }\mu\text{m} \pm 5 \text{ }\mu\text{m}$) were obtained as a trimethylated SiO_2 gel powder from Dow Corning (Midland, Michigan). **Figure 18** shows the SEM micrographs of surfaces using microparticles alone as well as surfaces with nanoparticles included. Both types of surfaces with microparticle concentrations of 400 mg/L and 1400 mg/L in spray solution are shown. The measured values of average microparticle pitch (P_{avg}), found as described earlier, are also displayed ($40 \text{ }\mu\text{m}$ and $21 \text{ }\mu\text{m}$ in the top and bottom of the figure, respectively). The images are analogous to those in **Fig. 17**: the lowest magnification shows average pitch between microparticles, the middle shows an individual microparticle, and the highest shows surface nanoscale roughness.

2.3.3 Characterization of samples with microstructured, nanostructured, and hierarchically structured surfaces

For contact angle and contact angle hysteresis data, droplets of $5 \text{ }\mu\text{L}$ in volume (with a radius of about 1 mm) were deposited onto samples using a microsyringe. Reproducibility of all CA and CAH data is reported as ($\pm\sigma$) as determined from measurement on five samples. Images of the droplets were obtained using a digital camcorder (Sony, DCRSR100, Tokyo, Japan) with a 10x optical and 120x digital zoom.

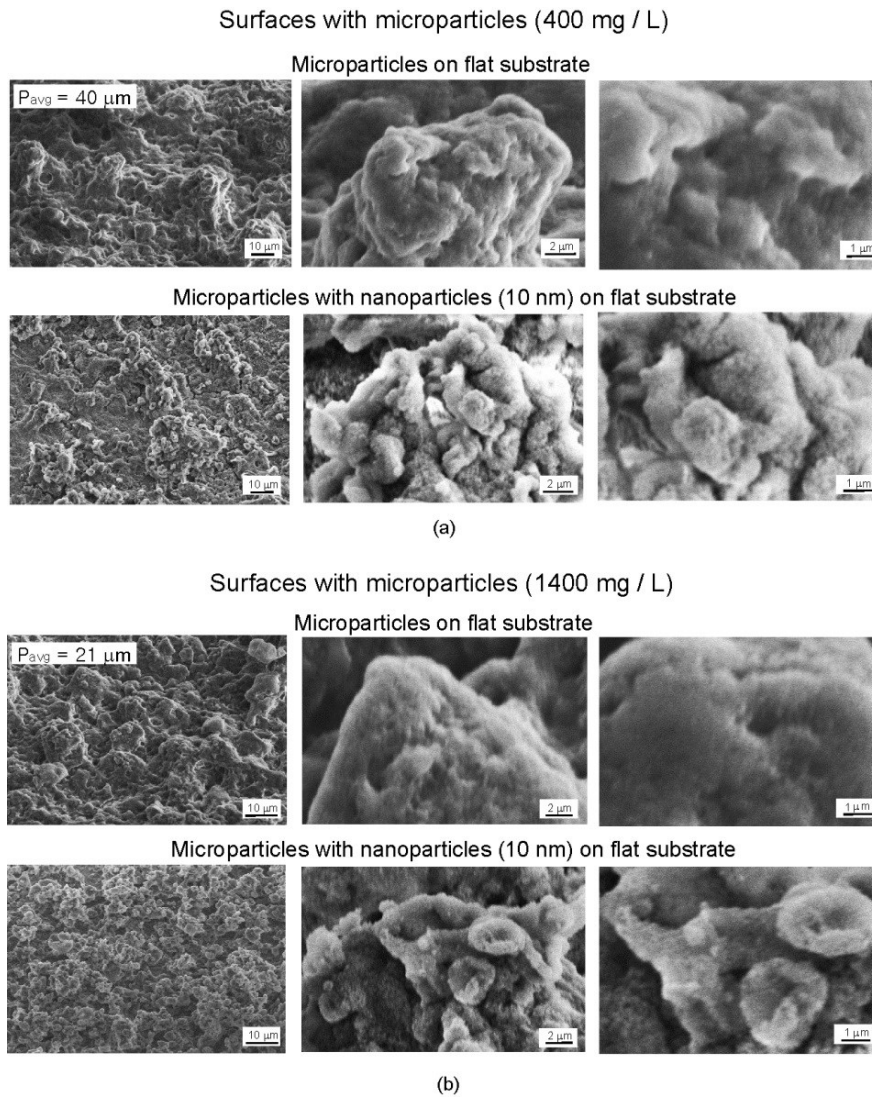


Figure 18: SEM micrographs taken at 45° tilt angle showing microparticles with and without nanoparticles at two different concentrations of microparticles in spray solution. Three magnifications are shown for microparticle spray concentrations of (a) 400 mg/L and (b) 1400 mg/L, both with and without nanoparticles in each case. The resulting average pitch values (P_{avg}) are indicated on images at lowest magnification. Nanoparticle concentration was 2000 mg/L when added (Ebert and Bhushan, 2012a).

For CAH, a surface was slowly inclined on a tilting stage, and the advancing and receding contact angle were measured just as the droplet began to move (see **Fig. 4b**). Images were analyzed for CA and CAH using Scion® image software.

The mechanical durability of the surfaces was examined through wear experiments using an AFM (for wear of the nanostructure) and a ball-on-flat tribometer (for wear of the microstructure). Ability to preserve Lotus Effect properties was also examined in a water jet experiment. An established AFM wear procedure was performed (Jung and Bhushan, 2009; Bhushan, 2010, 2011) with a commercial AFM (D3100, Nanoscope IIIa controller, Digital Instruments, Santa Barbara, CA). Surfaces with SiO₂ nanoparticles were worn using a borosilicate ball with radius 15 μm mounted on a rectangular Si(100) cantilever with nominal spring constant of 7.4 N/m. Areas of 50 x 50 μm² were worn for 1 cycle at a load of 10 μN. To analyze the change in the morphology of the surfaces before and after the wear experiment, height scans of 100 x 100 μm² in area were obtained using a rectangular Si(100) cantilever with a resonant frequency of 76 kHz in tapping mode and a spring constant of 3 N/m. The cantilever has a square pyramidal Si(100) tip with nominal radius of 20 nm and a native oxide layer. As a baseline, the wear results for the SiO₂ nanoparticles are compared to that of epoxy resin on a flat surface.

Microscale wear was examined with an established procedure of using a ball-on-flat tribometer (Bhushan, 1999, 2011, 2013a,b). A sapphire ball of 3 mm diameter was fixed in a stationary holder. A load of 10 mN was applied normal to the surface, and the tribometer was put into reciprocating motion. Stroke length was 800 μm and average

linear speed was 1 mm/s. Surfaces were imaged before and after the tribometer wear experiment using an optical microscope with a CCD camera (Nikon Optiphot-2) to examine changes. In addition, the profile of the surface was obtained across the wear scar using a Tencor® stylus profiler. Samples with SiO₂ microparticles alone as well with nanoparticles included were studied. Epoxy resin on a flat surface was again used as a benchmark for comparison.

To examine the durability of surfaces in water flow of varying kinetic energy, an established water jet procedure was performed (Jung and Bhushan, 2009). A schematic of the water jet setup is shown in **Fig. 19**. Surfaces with combined micro- and nanoparticles were examined as well as epoxy resin on a flat surface. Samples were exposed to water jet flow at different kinetic energy levels by varying the water pressure. The exposure time was 20 minutes at each pressure. After each experiment, the CA and CAH of the samples were measured as described previously.

2.4 Results and discussion for hierarchically structured surfaces

The wettability and mechanical durability of the hierarchically structured surfaces created using both types of microstructures are discussed below. First, the CA and CAH of the nanostructured, microstructured, and hierarchically structured surfaces are reported. Then, the data for the micro- and hierarchically structured surfaces using micro- and nanoparticles are examined, including comparison of CA and CAH to micropatterns. Lastly, the results of the wear experiments for durability are discussed.

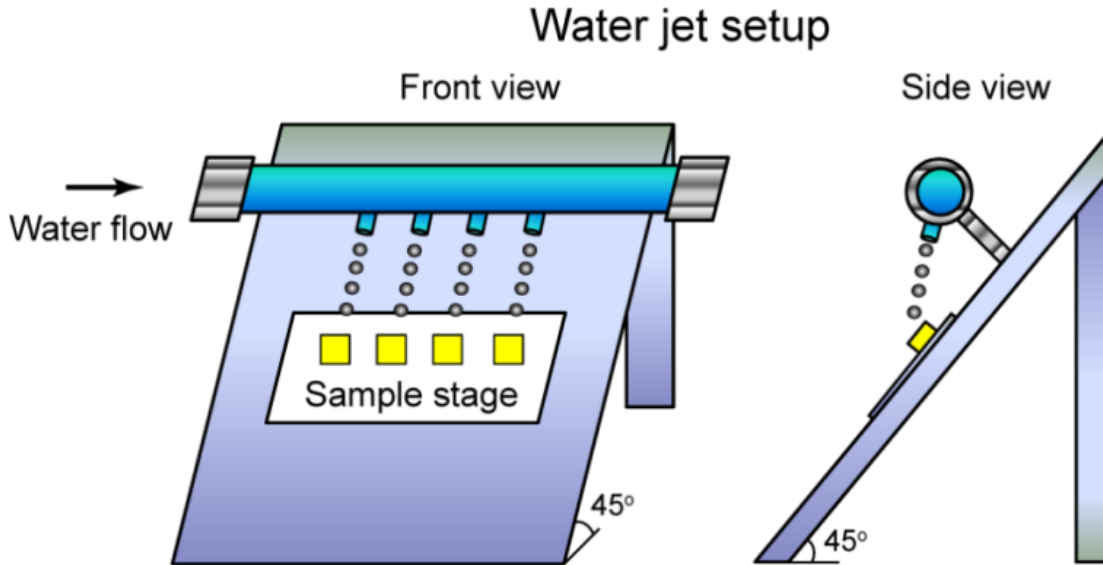


Figure 19: Schematic of water jet setup shown in front and side views (Jung and Bhushan, 2009)

2.4.1 Wettability of structured surfaces using micropattern

Contact angle and contact angle hysteresis data for the 10 nm and 50 nm particles on flat and micropatterned surfaces are shown in **Fig. 20**. Data for the micropattern without nanoparticles is shown for reference. In the cases of both flat and micropatterned surfaces, the difference in the data between the 10 nm and 50 nm particles was insignificant. Nanoparticles on a flat surface (nanostructure) showed a CA of $161^\circ (\pm 2^\circ)$ and CAH of $2^\circ (\pm 1^\circ)$. The CA and CAH of the epoxy micropattern alone were found to be $151^\circ (\pm 2^\circ)$ and $33^\circ (\pm 2^\circ)$, respectively. For nanoparticles on the micropattern (hierarchical structure), the highest CA of $168^\circ (\pm 2^\circ)$ and lowest CAH of $1^\circ (\pm 0.5^\circ)$ were found. The relative improvements in CA and CAH (higher CA and lower CAH are

desired) seen in the nanostructured, microstructured, and hierarchically structured surfaces are in agreement with Jung and Bhushan's work using carbon nanotubes and Lotus wax (Jung and Bhushan, 2009).

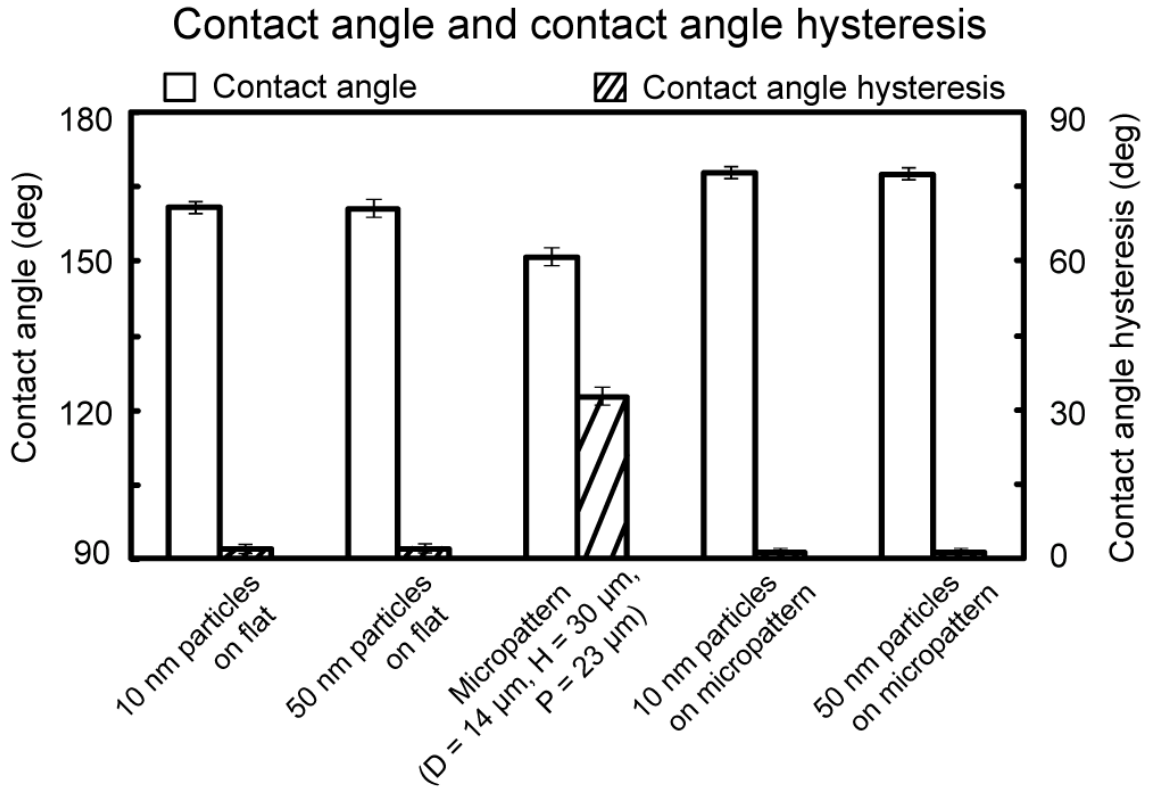


Figure 20: Bar chart showing the measured static contact angle and contact angle hysteresis on nano-, micro- and hierarchically structured surfaces using both 10 nm and 50 nm particles. The error bars represent ± 1 standard deviation. (Ebert and Bhushan, 2012a).

2.4.2 Wettability of surfaces with microparticles and comparison to surfaces with micropattern

The CA and CAH of surfaces with 10 μm particles on flat and 10 μm /10 nm particles combined on flat are shown in **Fig. 21** across a range of average pitch values. In addition, the CA and CAH of epoxy micropatterns of varying pitch are shown in order to provide a comparison of the trends seen with microparticles versus micropatterns. In this comparison, micropatterns with pillars with $D = 5 \mu\text{m}$ and $H = 10 \mu\text{m}$ were used, as the size is more comparable to the microparticles. It is seen that for 10 μm particles alone on flat, the trends in CA and CAH with pitch are similar to those of the micropatterns. The micropatterns maintain a contact angle above 150° from the lowest pitch value until a sharp drop at a pitch of 60 μm . The surfaces with microparticles similarly show a steady CA above 150° , with a sharp drop at an average pitch of 40 μm . For CAH, the micropattern shows a steady decrease with increasing pitch, until a large increase occurs at 60 μm . For the 10 μm particles, an initial decrease is seen at low pitch, and very low CAH is seen until a large increase occurs, again at 40 μm .

The sudden changes in CA and CAH, occurring at around 45 to 60 μm pitch for the micropatterns and around 25 to 40 μm average pitch for the microparticles, represent the transition to the Wenzel regime. This can be concluded for two reasons: the sudden drop in CA is predicted by Eq. (3) when f_{LA} is reduced to zero (as water fills the air gaps forming a homogeneous solid-liquid interface), and the sudden increase in CAH is expected as the interface triple line is confronted with greater roughness and adhesion

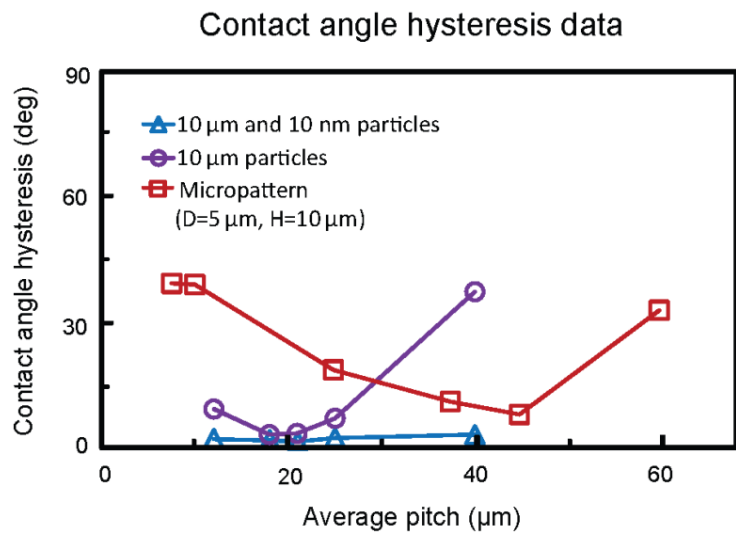
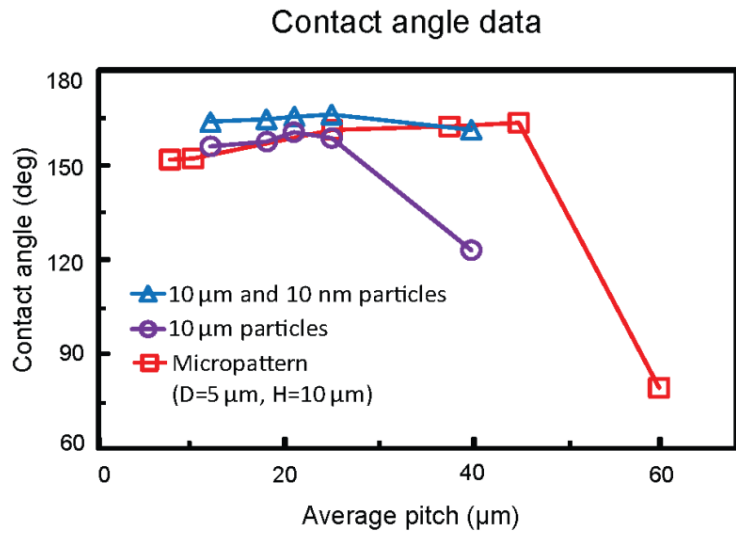


Figure 21: Static contact angle and contact angle hysteresis as a function of average pitch for surfaces with 10 μm particles alone and with 10 μm/10 nm particles combined. Epoxy micropattern data is also shown for comparison of microstructure behavior. Reproducibility is $\pm 1^\circ$ for CAH of 10 μm/10 nm particles combined, $\pm 2^\circ$ for CAH of 10 μm particles and epoxy micropatterns, and $\pm 2^\circ$ for all CA data. Lines between data points are intended only to guide the eyes and not for interpolation (Ebert and Bhushan, 2012a).

effects in the now larger solid-liquid interface. If transition did not occur, CA would be expected to remain approximately the same or increase, and CAH would be expected to remain approximately the same or decrease. At these pitch values, the droop of the water between microstructures (**Fig. 13**) is enough that the water fully penetrates between them, leaving no air pockets. For the micropatterns, the transition pitch value of around 45 to 60 μm is reasonably close to the value predicted by Eq. (4) given in section 2.2 (74 μm with $D = 5 \mu\text{m}$, $H = 10 \mu\text{m}$). The transition value for the surfaces with 10 μm particles can be expected to be different since the pitch, diameter and height are much less uniform compared to the micropatterns. However, the similarity of the overall trends in CA and CAH with pitch indicates that the microparticles are reasonably mimicking a micropatterned surface. In addition, the data for the 10 μm /10 nm particles combined shows an overall increase in CA and decrease in CAH compared to the 10 μm particles alone, indicating that the benefits of hierarchical structure can be realized using the 10 μm particles as the underlying microstructure. CA as high as $166^\circ (\pm 2^\circ)$ and CAH as low as $2^\circ (\pm 1^\circ)$ were seen for these surfaces.

2.4.3 Wear resistance in AFM sliding wear, tribometer, and water jet experiments

The results of the AFM sliding wear experiment for 10 nm particles as well as an epoxy resin are shown in **Fig. 22**. Surface height maps before and after the wear experiment are displayed, as well as sample scans across the middle of the image

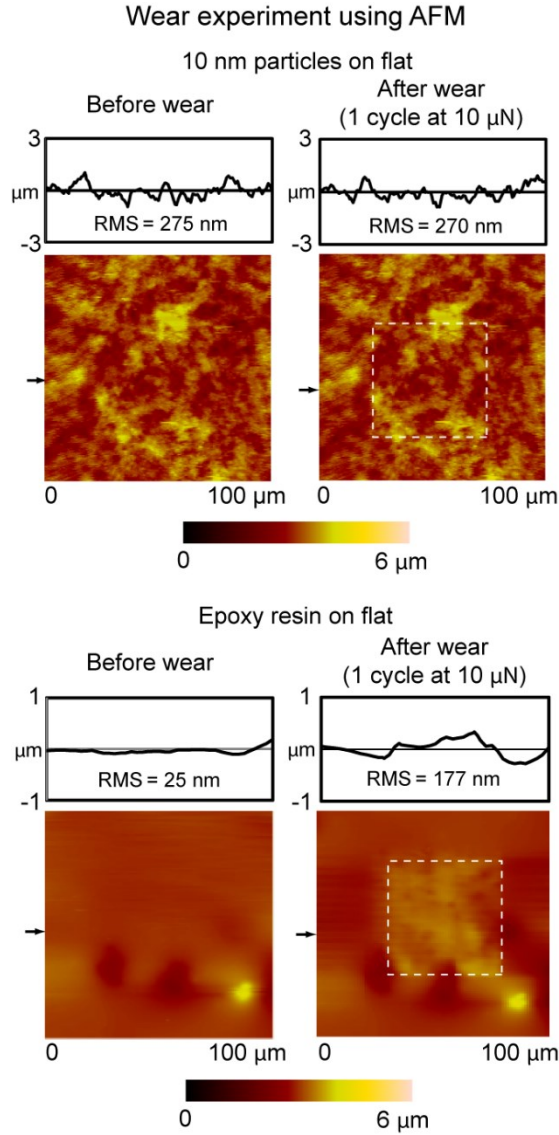


Figure 22: Surface height maps and sample surface profiles (locations indicated by arrows) before and after AFM wear experiment with 15 μ m radius borosilicate ball at load of 10 μ N for 10 nm particles on flat surface (top) and epoxy resin on flat surface (bottom). RMS roughness values for surface profiles are displayed within surface profile boxes (Ebert and Bhushan, 2012a).

(position indicated by arrow) with root mean square roughness (RMS) within the wear area displayed. After 1 cycle at 10 μN with the borosilicate ball, the morphology of the surface with 10 nm particles was not significantly changed, and RMS of the sample scan within the wear area was nearly identical (270 nm after compared with 275 nm before). However, the after-image for the epoxy resin reveals some wear, as well as an overall swelling of the wear area. In addition, RMS of the sample scan increased from 25 nm to 177 nm within the wear area. This demonstrates that the durability of the nanoparticle-coated surfaces is superior to that of the surfaces with epoxy resin alone.

The ball-on-flat tribometer experimental results are shown in **Fig. 23** for surfaces with 10 μm particles, 10 μm /10 nm particles combined, and an epoxy resin. Before and after images as well as a scan across the wear scar are displayed for 10 μm particles on flat, 10 μm with 10 nm particles on flat, and epoxy resin on flat. After 100 cycles at 10 mN, the 10 μm particles alone showed minimal wear (mainly in the form of burnishing of the tops of particles), and a microscale roughness is preserved. The 10 μm and 10 nm particles combined show similar results of minimal wear. However, the after image of the epoxy resin reveals a well-defined groove. The scan shows buildup along the sides of the groove, and the groove depth can be seen as approximately 300 nm. Thus, the surfaces with microparticles also showed resistance to wear superior to that of the surfaces with epoxy resin alone.

Results of the water jet experiment can be seen in **Fig. 24**. Samples were exposed to

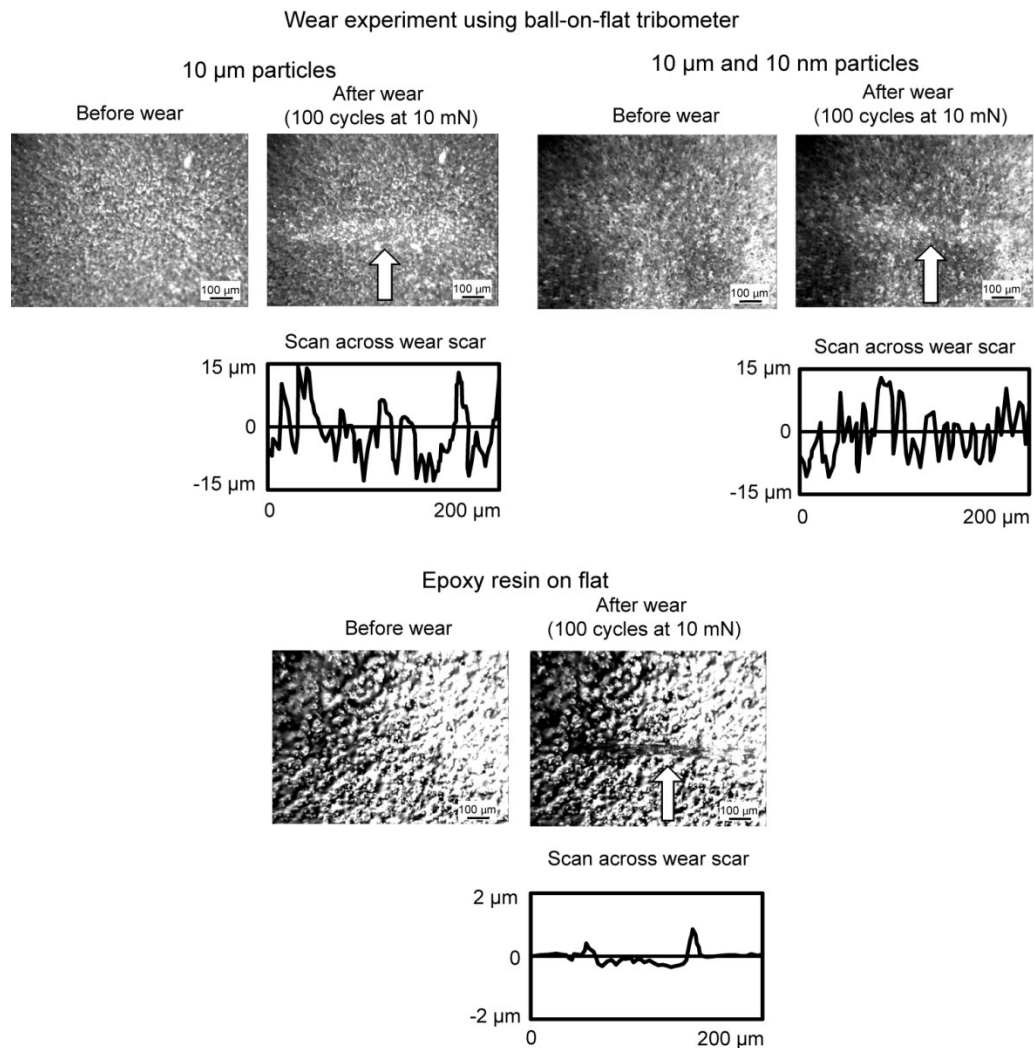


Figure 23: Optical micrographs before and after wear experiment using ball-on-flat tribometer at 10 mN for 10 μm particles (top), 10 μm particles with 10 nm particles (middle), and epoxy resin on flat surface (bottom). Sample profiles across wear areas are shown below after-images (arrows indicate location of profile) (Ebert and Bhushan, 2012a).

water with pressure ranging from 0 to 45 kPa for 20 minutes. Data from samples with combined 10 μm and 10 nm particles at an average microparticle pitch of 21 μm are shown, as well as data from the epoxy resin on flat surface. For the samples with 10 μm /10 nm particles, Lotus Effect properties were maintained even at highest pressure, with CA decreasing slightly to 161° from 165°, and CAH increasing slightly to 3° from 1°. The wettability of the samples with epoxy resin on flat was likewise not significantly changed. Interestingly, in contrast to the superhydrophobic samples, a slight increase in CA and a slight decrease in CAH was seen. This can be due to a small decrease in roughness on the epoxy samples, which in a Wenzel framework would be expected to increase CA for a hydrophilic surface. In addition, a slight reduction in roughness could reduce pinning effects at asperities, reducing the CAH.

2.5 Conclusions

Mechanically durable, hierarchically structured surfaces with Lotus Effect characteristics were produced using micro- and nanosized SiO_2 particles and a simple spray process. In addition, a comparison was made between the use of microparticles and micropatterns in terms of wettability across different pitch values. Results show similar trends in CA and CAH with pitch value whether the microstructure was formed with particles or a micropattern. This indicates that microparticles can be effectively utilized as a means to create the underlying microscale roughness for Lotus Effect surfaces employing hierarchical structure. Hierarchical surfaces using micro- and nanoparticles

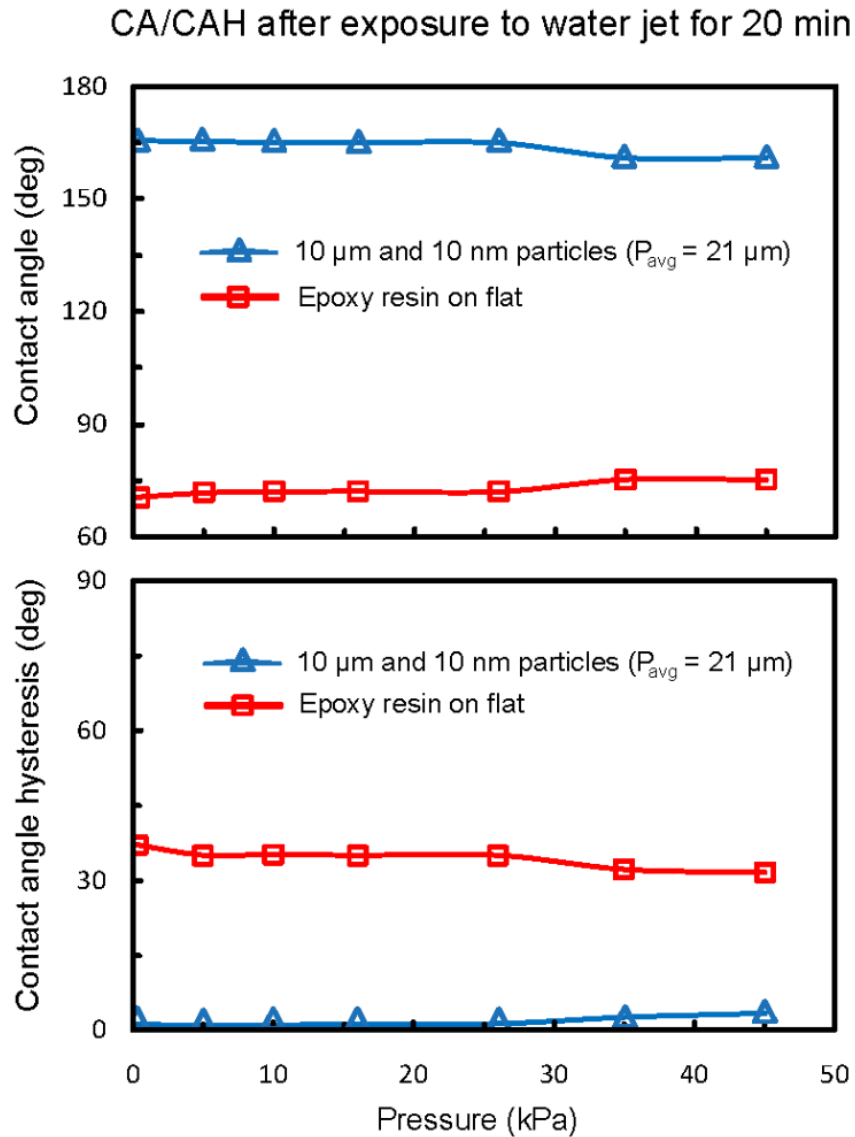


Figure 24: Static contact angle (top) and contact angle hysteresis (bottom) as a function of water pressure after 20 min. exposure time for samples with combined 10 μm/10 nm particles and epoxy resin on flat surface. Reproducibility is $\pm 1^\circ$ for CAH of 10 μm/10 nm particles, $\pm 2^\circ$ for CAH of epoxy resin, and $\pm 2^\circ$ for all CA data. Lines between data points are intended to guide the eyes (Ebert and Bhushan, 2012a).

exhibited CA of $166^\circ (\pm 2^\circ)$ and CAH of $2^\circ (\pm 1^\circ)$ at optimum pitch. For hierarchical surfaces using micropatterns with nanoparticles, a nearly identical CA of $168^\circ (\pm 2^\circ)$ and CAH of $1^\circ (\pm 0.5^\circ)$ were measured. In both cases, the requirements of superhydrophobicity ($CA > 150^\circ$) and self-cleaning ($CAH < 10^\circ$) were easily met. In addition, the surfaces demonstrated wear resistance superior to the epoxy resin on multiple length scales in the AFM and tribometer experiments, showing ability to preserve both nanoscale and microscale roughness. Preservation of superhydrophobicity under exposure to impacting water was demonstrated in water jet experiments. Excellent Lotus Effect properties combined with mechanical durability give these surfaces potential for industrial applications, such as water-repellent coatings, self-cleaning surfaces, and drag reduction in water.

CHAPTER 3: Rose Petal Effect Surfaces with Superhydrophobicity and High Droplet Adhesion

3.1 Introduction and Background

In nature, superhydrophobic surfaces with very low droplet adhesion are found on the leaves of many plants, most famously the Lotus. A water droplet on the Lotus leaf will roll off almost effortlessly. There also exist surfaces, such as the red rose petal, that exhibit superhydrophobicity with high droplet adhesion; the droplet remains pinned even when the petal is inverted. However, while there has been much research in superhydrophobic surfaces with low droplet adhesion (the so-called “Lotus Effect”), significantly fewer studies have been published on superhydrophobic surfaces with high droplet adhesion (the so-called “Rose Petal Effect”) (Feng *et al.*, 2008; Bormashenko *et al.*, 2009; Bhushan and Her, 2010; Dawood *et al.*, 2011; Zhao *et al.*, 2011; Zheng *et al.*, 2011; Stanton *et al.*, 2012). These surfaces have potential for applications including single-molecule spectroscopy (Winkleman *et al.*, 2008) and controlled transport of small volumes of liquid in open microfluidic devices (Hong *et al.*, 2007).

The Rose Petal Effect is believed to occur as the result of a special wetting regime known as the impregnating state (Feng *et al.*, 2008). In contrast to the Wenzel regime, in which liquid fully wets a rough surface, and the Cassie-Baxter regime, in which liquid

rests only on the highest asperities leaving air pockets, a droplet in the impregnating regime fully penetrates between microscale features, but is unable, or only partially able, to penetrate between nanoscale features. In this sense, the impregnating regime can be thought of as an intermediate state, with liquid wetting a lower fraction of the surface than in the Wenzel regime, but a higher fraction than in the Cassie-Baxter regime. **Figure 25** illustrates the impregnating and Cassie-Baxter wetting regimes. In the impregnating regime, the penetration of microstructures and partial penetration of nanostructures causes high contact angle hysteresis (CAH) and therefore high droplet adhesion. In the Cassie-Baxter regime, the droplet has very low CAH and adhesion as a result of resting only on the tips of nanostructures and only partially drooping between microstructures. The pitch of microstructures and density of nanostructures are known to be critical in creating superhydrophobic surfaces with both high and low adhesion (Bhushan and Her, 2010).

The contact angle (CA) of a droplet in the Wenzel regime can be predicted by Eq. (2) (given in section 1.2), which implies that increasing roughness will increase the CA of a hydrophobic surface and decrease the CA of a hydrophilic surface. Therefore, in the Wenzel regime, a superhydrophobic state can only be achieved by introducing roughness to a hydrophobic surface. In the Cassie-Baxter regime, CA can be predicted by Eq. (3) (given in section 1.2), which implies that superhydrophobicity can be achieved in the Cassie-Baxter regime with sufficiently high f_{LA} due to air pockets, even if the surface chemistry is hydrophilic. In the impregnating regime, air pockets exist primarily in

Droplets on hierarchical structure with same microstructure pitch value and different nanostructure density

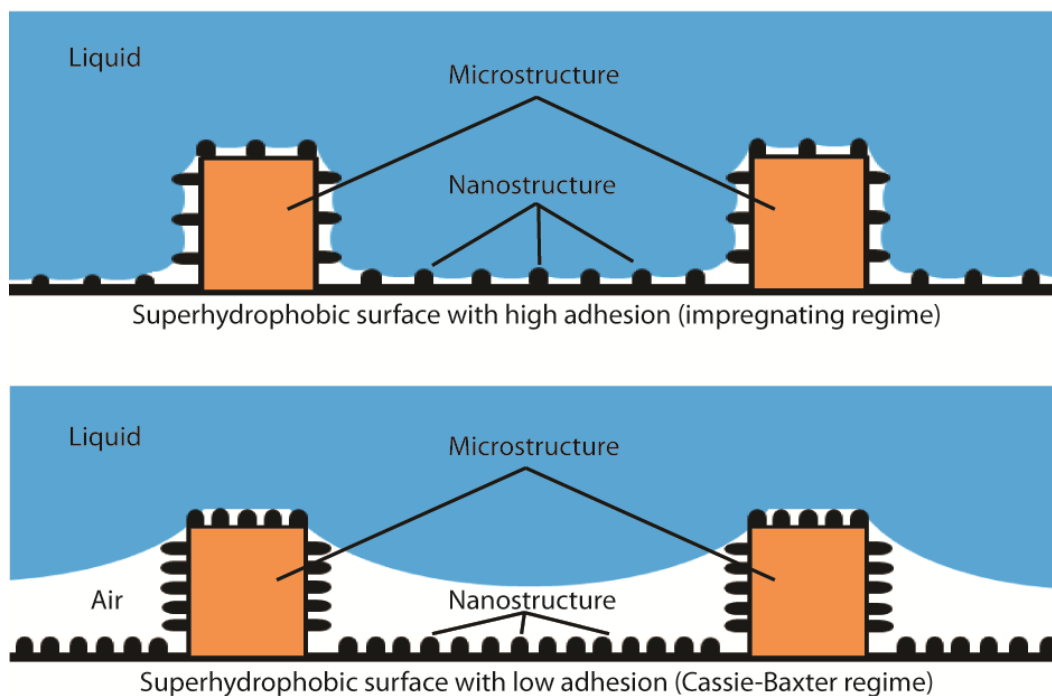


Figure 25: Schematic of droplets on superhydrophobic surfaces with high adhesion (impregnating regime, shown at top) and low adhesion (Cassie-Baxter regime, shown at bottom). Surfaces have hierarchical structure with same microstructure pitch value and different nanostructure density (Ebert and Bhushan, 2012b).

the nanostructure, providing a moderate value of f_{LA} . This leads to high CA but may result in high CAH, which is responsible for high droplet adhesion. It would ostensibly seem possible to create Rose Petal Effect surfaces using hydrophobic or hydrophilic materials to form the micro- and nanostructures. In the case of nanoparticles, which are often used to create nanoscale roughness, it may be of interest to study the effect of hydrophobic

versus hydrophilic surface chemistry. **Table 1** outlines a few of the potential benefits and drawbacks of hydrophobic vs. hydrophilic particles in the fabrication of structured

Table 1: Potential advantages and disadvantages of hydrophobic vs. hydrophilic nanoparticles in fabrication of structured surfaces (Ebert and Bhushan, 2012b)

Particle surface chemistry	Potential advantages	Potential disadvantages
Hydrophobic	<ul style="list-style-type: none"> • Can create superhydrophobic surfaces with high CA and low CAH • Good dispersibility in non-polar solvents 	<ul style="list-style-type: none"> • Poor dispersibility in polar solvents
Hydrophilic	<ul style="list-style-type: none"> • Can be used for high adhesion surfaces • Good dispersibility in polar solvents 	<ul style="list-style-type: none"> • More difficult to create superhydrophobic surfaces • Poor dispersibility in non-polar solvents

surfaces. In addition, for industrial applications, mechanical durability and wear resistance are necessary for Rose Petal Effect and other structured surfaces.

The motivation of this study was to create surfaces that achieve the Rose Petal Effect (superhydrophobicity combined with high droplet adhesion) for applications such as the transport of small volumes of liquid, which can be useful in microfluidic devices. The combination of superhydrophobicity and very high CAH (high adhesion) results in a droplet that is nearly spherical in shape, but remains pinned to the surface even when it is inverted. The objectives of this study were to create mechanically durable surfaces using hydrophobic and hydrophilic nanoparticles, and to examine the effects of microstructure

pitch and nanostructure density in regard to achieving high CA and high CAH. To create hierarchical structures, hydrophilic ZnO nanoparticles were deposited onto micropatterns with varying pitch values via a spray technique with varying particle concentration and using an epoxy binder, which is known to provide durability. The prepared samples were then modified by octadecylphosphonic acid (ODP) in solution in order to hydrophobize the exposed ZnO nanoparticles. ODP can be used to functionalize metal oxides from hydrophilic to hydrophobic (Gao *et al.*, 1996; Nishimoto *et al.*, 2009). CA and CAH (contact angle hysteresis) were measured before and after ODP hydrophobization. In addition, roughness and f_{LA} were measured in order to determine theoretical values in the Wenzel and Cassie-Baxter regimes. To examine wear resistance, an AFM wear experiment was performed.

3.2 Experimental details

3.2.1 Preparation of hierarchically structured samples

Epoxy micropatterns were fabricated by replicating micropatterned Si surfaces through soft lithography using the method described in section 2.3.1 and shown schematically in **Fig. 15**. The epoxy used was weakly hydrophilic, with a CA of $80^\circ \pm 2^\circ$ for a flat epoxy surface with no micropattern. The micropatterns used consist of arrays of cylindrical micropillars with diameter of 14 μm and height of 30 μm . The pitch values used were 23, 105, and 210 μm , where pitch is defined as the center-to-center distance between micropillars.

Hierarchically structured surfaces using micropatterns were created by depositing nanoparticles onto the micropatterned epoxy substrates using an established spray method described in section 2.3.1 and illustrated in **Fig. 16**. Nanostructured surfaces were also created by spraying particles onto flat substrates. ZnO nanoparticles with average diameter of 70 nm were obtained from Alfa Aesar (USA). In order to spray the particles onto the surfaces, they were first dispersed uniformly in solution. The desired quantity of particles was sonicated in 100 mL of acetone for 4 minutes with a Branson Sonifier 450A with a frequency of 20 kHz at 80% amplitude. For strong bonding of the nanoparticles to the substrates, 200 mg of EPON epoxy resin 1002F (Hexion Specialty Chemicals, Columbus, Ohio) was then added, and the solution was sonicated for another 4 minutes. The dispersion of particles in solution was then sprayed onto the sample surface using a spray gun. The samples were then annealed at 120 °C for 3 hours. Annealing at this temperature (above the melting point and below the burning point of EPON 1002F) allowed the resin to melt and move to the interface between the particles and the surface.

The ZnO nanoparticles were not surface-modified as received, and are intrinsically hydrophilic. In order to hydrophobize them, they were treated in solution by octadecylphosphonic acid (ODP) obtained from Aldrich. ODP can be used to functionalize metal oxides from hydrophilic to hydrophobic (Nishimoto *et al.*, 2009). The process by which functionalization occurs is illustrated in **Fig. 26**. The exposed long-chain hydrocarbon tails of the ODP molecules result in a hydrophobic particle surface. Samples were immersed in a 100 mL ethanol solution with ODP concentration of 2 mM

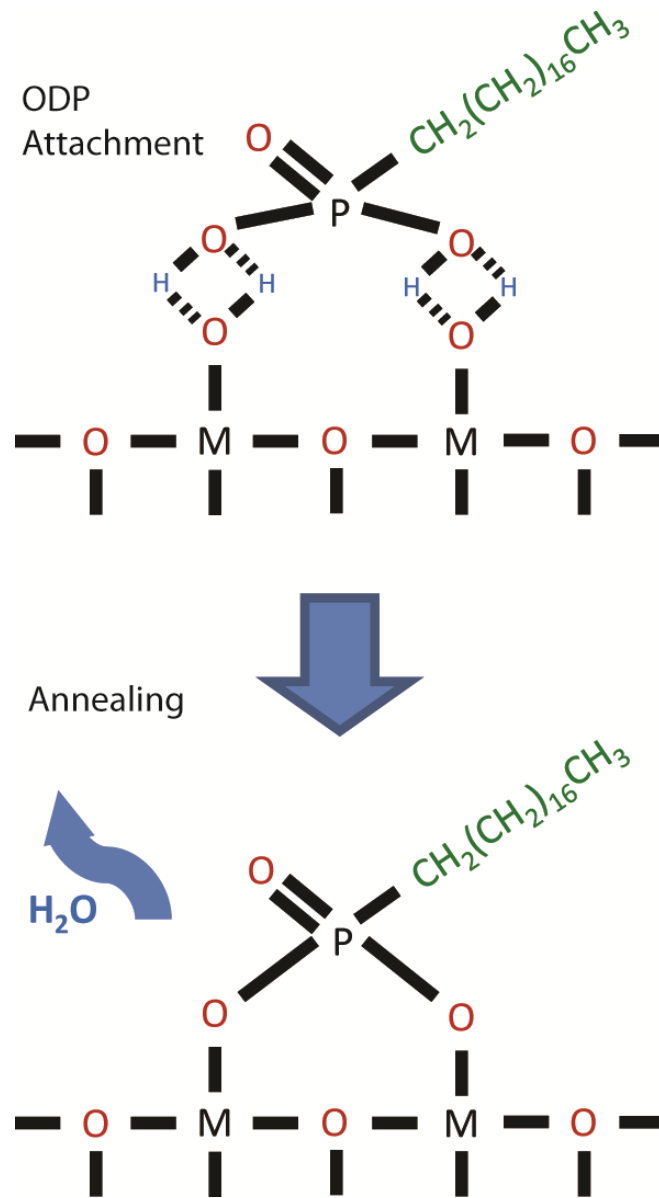


Figure 26: Schematic of hydrophobization of a generic metal oxide surface with octadecylphosphonic acid (ODP). The ODP molecule first attaches to the hydrolyzed surface via hydrogen bonds. After annealing, the ODP is strongly bonded to the metal oxide surface (Ebert and Bhushan, 2012c).

for 4 days at 20 °C. The samples were then heated at 100 °C for 1 hour to improve ODP bonding and remove adsorbed water or remaining solvent.

3.2.2 Characterization of samples

For wettability measurements, water droplets of 5 μL volume (~ 1 mm radius) were deposited onto samples using a microsyringe. CA and CAH were measured using a model 290-F4 Ramé-Hart goniometer (Ramé-Hart Inc., Succasunna, NJ). CAH was determined using the tilt method shown in **Fig. 4b**. Reproducibility of all CA and CAH data is reported as ($\pm\sigma$) as determined from measurement on five samples.

An established AFM wear procedure (Bhushan, 2011; Jung and Bhushan, 2009; Ebert and Bhushan, 2012a) was conducted with a commercial AFM (D3100, Nanoscope IIIa controller, Digital Instruments, Santa Barbara, CA). Samples were worn using a borosilicate ball with radius 15 μm mounted on a rectangular Si(100) cantilever ($k = 7.4$ N/m) in contact mode. Areas of 50 x 50 μm^2 were worn for 1 cycle at a load of 10 μN . To analyze the change in the morphology of the surfaces before and after the wear experiment, height scans of 100 x 100 μm^2 in area were obtained using a rectangular Si(100) tip ($f = 76$ kHz, $k = 3$ N/m) in tapping mode. As a baseline, the wear results for the samples were compared to that of the epoxy resin alone on a flat substrate.

3.3 Results and discussion

Wettability data for the structured surfaces with ZnO nanoparticles are reported and discussed in this section. First, data for samples with hydrophilic particles (before ODP

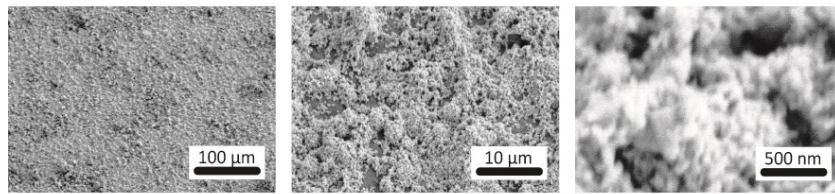
modification) are examined. Next, data with hydrophobic particles (after ODP modification) are discussed. Lastly, the results of the AFM wear experiment are analyzed.

3.3.1 Samples with hydrophilic nanostructure (before modification)

Figure 27 shows SEM micrographs of ZnO nanoparticles on flat and micropatterned substrates. The particles are shown on a flat substrate at three magnifications in **Fig. 27a**, while **Fig. 27b** shows microstructures at three pitch values along with an individual micropillar coated with nanoparticles at two different spray concentrations. Nanostructured surfaces were formed in the case of nanoparticles on flat substrate, while hierarchically structured surfaces were formed in the case of nanoparticles on microstructures.

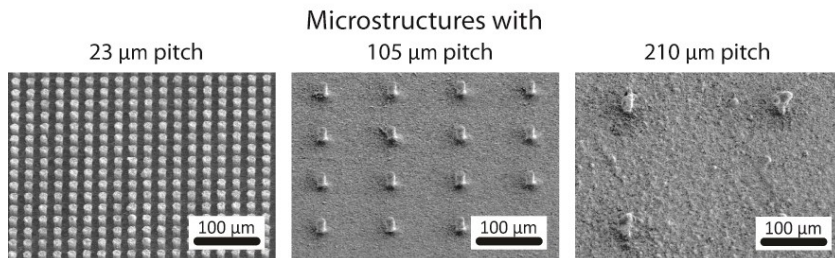
The CA and CAH data for microstructured and flat substrates with varying nanoparticle spray concentration are displayed in **Fig. 28**. At a pitch value of 23 μm , samples were superhydrophobic ($CA > 150^\circ$) at all nanoparticle concentrations. Droplet adhesion was low, as CAH did not exceed 37° and droplets did not adhere when the surfaces were inverted. Because the pitch is relatively small, a water droplet is unable to penetrate between microstructures, and remains in Cassie-Baxter regime with low adhesion. At pitch values of 105 μm and 210 μm , the CA is hydrophilic for lower nanoparticle concentrations, indicating that water is penetrating between microstructures and resulting in Wenzel regime wetting. At higher nanoparticle concentrations, superhydrophobic CAs were achieved (at 1500 mg/L and above for 105 μm pitch,

ZnO nanoparticles (3000 mg/L) on flat substrate



(a)

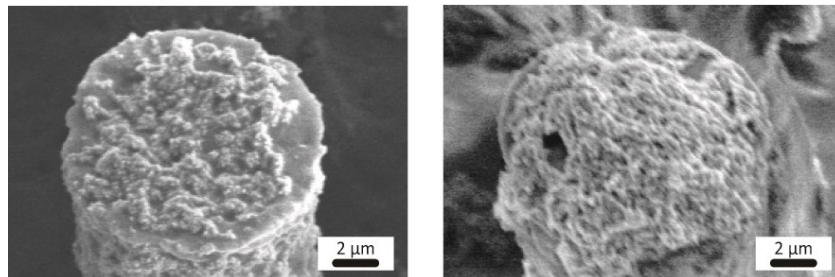
Hierarchical structures with ZnO nanoparticles



Low magnification images

ZnO nanoparticles (1000 mg/L)

ZnO nanoparticles (2250 mg/L)



High magnification images

(b)

Figure 27: SEM micrographs of (a) ZnO nanoparticles on flat substrate at three magnifications and (b) low magnification images of microstructures at three different pitch values, along with high magnification images of individual micropillar with two different nanoparticle spray concentrations. The different spray concentrations produce different nanostructure density values. (Ebert and Bhushan, 2012b)

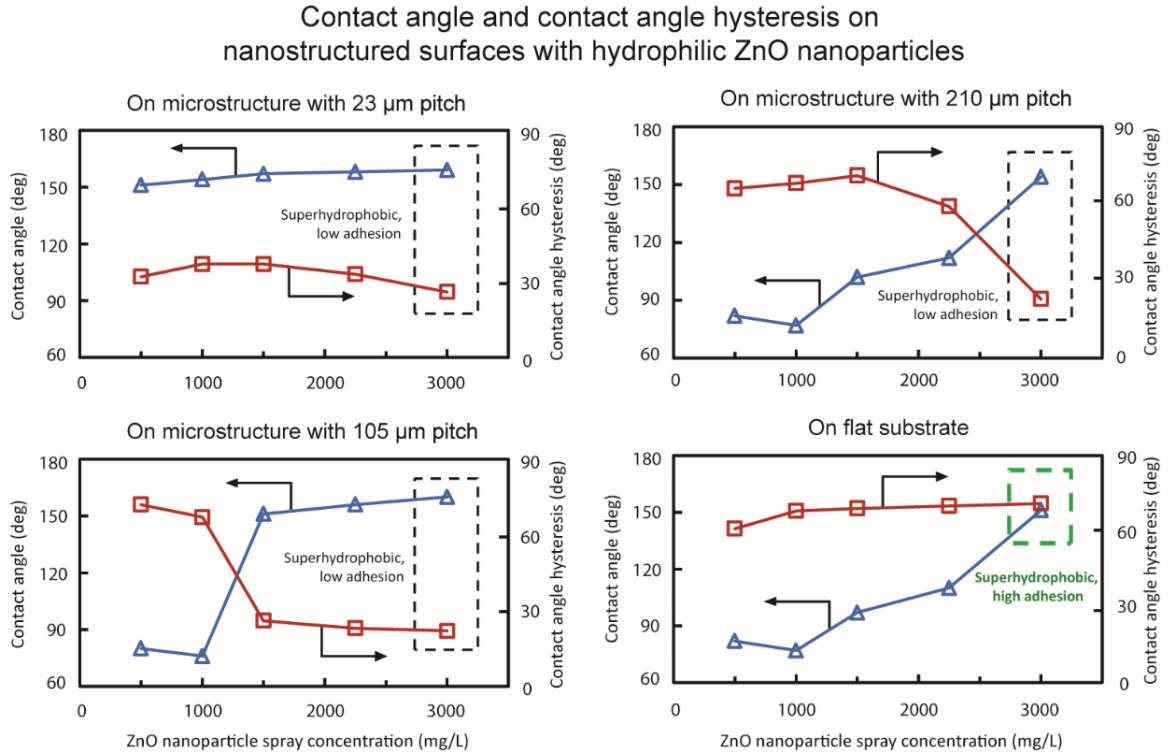


Figure 28: Contact angle and contact angle hysteresis data on nanostructured surfaces with hydrophilic ZnO nanoparticles (before modification with octadecylphosphonic acid (ODP)) using microstructures with three different pitch values (23 μm , 105 μm , 210 μm) as well as a flat substrate. Reproducibility is $\pm 1^\circ$ for CA data and $\pm 2^\circ$ for CAH data. “Low adhesion” indicates $\text{CAH} < 30^\circ$, while “high adhesion” indicates adherence of droplet to an inverted substrate. Lines between data points are intended only to guide the eyes and not for interpolation (Ebert and Bhushan, 2012b).

and at 3000 mg/L for 210 μm pitch). However, in each case, the corresponding CAH values were low ($< 30^\circ$) and droplets did not adhere when inverted, indicating low adhesion. At higher nanoparticle concentration, the droplet is unable or only partially able to penetrate between microstructures, resulting in Cassie-Baxter wetting and low adhesion.

Interestingly, the only superhydrophobic, high adhesion state using hydrophilic particles occurred in the case of a flat substrate. At a particle spray concentration of 3000 mg/L, a superhydrophobic CA of 151° was and high CAH of 71° were measured. In addition, a water droplet could remain adhered to the surface when fully inverted. The morphology of this surface can be seen in **Fig. 27a**. As the flat epoxy substrate and the nanoparticles are hydrophilic, the high CAs seen at higher concentrations are likely the result of higher roughness, leading to partial rather than full wetting of the nanostructure. This partial wetting also allows for high adhesion. However, with hydrophilic particles, it seems that the nanoscale roughness required for a superhydrophobic state with high adhesion precludes the use of a microstructure of the size used in this study, even with pitch value as high as 210 μm . With the uniform microstructures used, the high nanoscale roughness leads to Cassie-Baxter wetting and low adhesion. However, SEM of flat surface with 3000 mg/L ZnO nanoparticles (**Fig. 27a**) reveals microscale roughness on the order of 2-3 μm , which may provide the dual-scale roughness necessary for an impregnating state.

Table 2 shows measured CA and CAH values for two selected surfaces using hydrophilic nanoparticles, as well as calculated CA using both Wenzel and Cassie-Baxter

Table 2: Summary of measured and calculated contact angle (CA) and measured contact angle hysteresis (CAH) for selected superhydrophobic surfaces with high and low adhesion using hydrophilic ZnO nanoparticles. Where microstructure is used, data for hierarchical structure correspond to final samples (Ebert and Bhushan, 2012b).

	R_f	f_{LA}	CA measured (deg) ($\pm 1^\circ$)	CA calculated using Wenzel equation (Eq. 2) (deg)	CA calculated using Cassie-Baxter equation (Eq. 3) (deg)	CAH measured (deg) ($\pm 2^\circ$)
Flat substrate with 3000 mg/L ZnO nanoparticle spray; superhydrophobic with high adhesion						
nanostructure	4.0	0.98	151	~0	155 ^a	71
105 μm pitch with 3000 mg/L ZnO nanoparticle spray; superhydrophobic with low adhesion						
nanostructure	4.0	0.98	151	~0	155	71
bare microstructure	1.1	0.98	77	79	167	72
hierarchical structure	5.1	0.99	169	~0	~180	22

^aOverprediction of CA by Cassie-Baxter equation, along with high CAH, suggests impregnating regime

equations (Eqs. (2) and (3) given in section 1.2). The CA of ZnO without roughness (θ_0) is assumed to be 15° (Zhang *et al.*, 2010). For the surface with 3000 mg/L nanoparticles on flat substrate, the values for the resulting nanostructure are reported. For the surface with 3000 mg/L nanoparticles on microstructure with 105 μm pitch, the values for the

nanostructure alone, the bare microstructure, and the resulting hierarchical structure are reported. The R_f for the nanostructure was calculated using an AFM surface height map. The true surface can be approximated using a method illustrated in **Fig. 29**. The height scan produces a data matrix of Z-height values for the surface. If the matrix has size $n \times n$, the area can be divided into $(n - 1) \times (n - 1)$ sections, or patches. Two right triangles can be formed by drawing a hypotenuse across each patch. By using the Z-height of each point, the areas of the two triangles making up each patch can be solved. The sum of all of these patch areas gives an approximation of the true surface area of a scan. Dividing this value by the nominal two-dimensional scan area (*i.e.* projected area) gives an approximation of the roughness factor, R_f (Burton and Bhushan, 2006). For the microstructure made up of cylindrical flat-topped pillars of diameter (D), height (H), and pitch (P) in a regular square array, the R_f can be found using Eq. (5) (Bhushan and Jung, 2007):

$$(R_f)_{micro} = 1 + \pi DH/P^2 \quad (5)$$

The roughness for the hierarchical structure $(R_f)_{hierarchical}$ is taken as the sum of $(R_f)_{micro}$ and $(R_f)_{nano}$. To find the value of f_{LA} for the nanostructure, AFM maps were used with SPIP™ imaging software (Image Metrology) with the assumption that the droplet contacts only the highest peaks of surface asperities in Cassie-Baxter regime. Based on this assumption, threshold height criteria can be selected for image processing and applied consistently across all samples. For the microstructure, the droplet in Cassie-Baxter regime can be assumed to contact just the flat tops of micropillars, f_{LA} can be

Approximation of true surface area
using AFM scan matrix

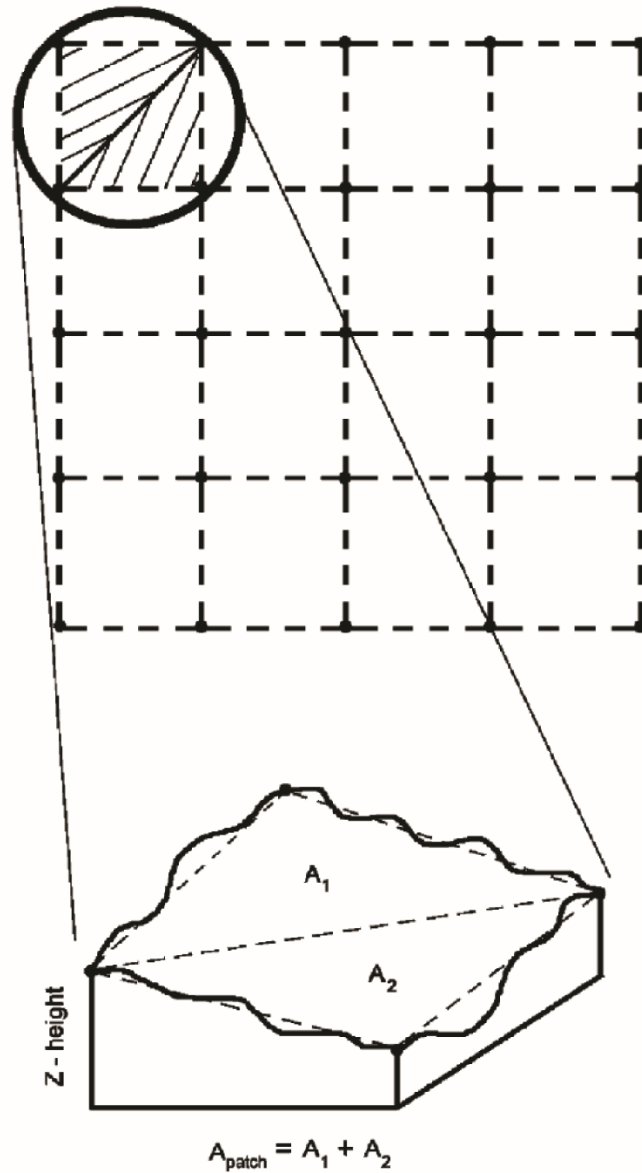


Figure 29: Illustration of approximation method for true surface area using an AFM scan matrix. Using the Z-height of each data point, two right triangles can be formed for each patch. The area of the patch (A_{patch}) is taken as the sum of the areas of the two triangles (Burton and Bhushan, 2006).

found using Eq. (6) (Bhushan and Jung, 2007):

$$(f_{LA})_{micro} = 1 - \pi D^2 / (4P^2) \quad (6)$$

The value of f_{LA} for the hierarchical structure can then be found using Eq. (7) (Bhushan and Jung, 2007):

$$(f_{LA})_{hierarchical} = (f_{LA})_{micro} + (f_{LA})_{nano}[1 - (f_{LA})_{micro}] \quad (7)$$

For both surfaces, R_f exceeds the value that results in a CA of 0° in the Wenzel regime, and the calculated CA using Eq. (2) (given in section 1.2) can be taken as 0° . For the surface with 3000 mg/L nanoparticles on microstructure with 105 μm pitch, R_f and f_{LA} are such that the calculated Cassie-Baxter CA exceeds 180° , and the calculated CA using Eq. (3) (given in section 1.2) can be taken as 180° . This overpredicts the measured value of 169° , however the low CAH of 22° indicates that Cassie-Baxter behavior with low adhesion is prevailing. For the surface with 3000 mg/L on flat substrate, the calculated Cassie-Baxter CA slightly overpredicts the measured value (155° vs. 151°). Coupled with high CAH of 71° and the ability of the droplet to remain adhered when inverted, this suggests an impregnating wetting regime with high adhesion. **Figure 30** shows images of the droplet on flat substrate with 3000 mg/L ZnO nanoparticles when it is horizontal, vertical, and upside-down.

3.3.2 Samples with hydrophobic nanostructure (after modification)

The CA and CAH data for microstructured and flat substrates with varying nanoparticle spray concentration after modification with ODP are displayed in **Fig. 31**.

Shape of droplets on flat substrate with hydrophilic ZnO nanoparticles (3000 mg/L spray conc.)

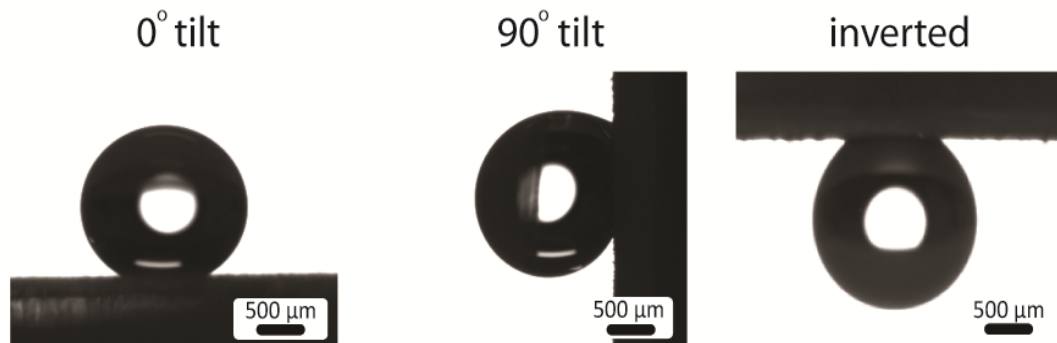


Figure 30: Droplets on flat substrate with hydrophilic ZnO nanoparticles at 3000 mg/L spray concentration at 0° tilt, 90° tilt, and fully inverted, showing superhydrophobicity and high droplet adhesion (Ebert and Bhushan, 2012b).

At a pitch value of 23 μm , surfaces were superhydrophobic for all nanoparticle concentrations, with CAH remaining below 25° and falling as low as 3° at higher concentrations. With a low pitch value of 23 μm , water is unable to penetrate the microstructure using either hydrophilic or hydrophobic particles. However, the hydrophobization of the particles provided a slight increase in CA and fairly substantial decrease in CAH. For samples on flat substrates and with microstructure pitch value of 210 μm , all surfaces with nanoparticle concentration of 1500 mg/L and above were superhydrophobic with low CAH (< 15°). At a concentration of 1000 mg/L, both had a highly hydrophobic CA (135° for flat, 139° for 210 μm pitch) and high CAH (56° for flat, 61° for 210 μm pitch). However, in addition to not achieving superhydrophobicity, a droplet did not adhere when the surface was inverted in either case.

Contact angle and contact angle hysteresis on nanostructured surfaces with hydrophobic ZnO nanoparticles

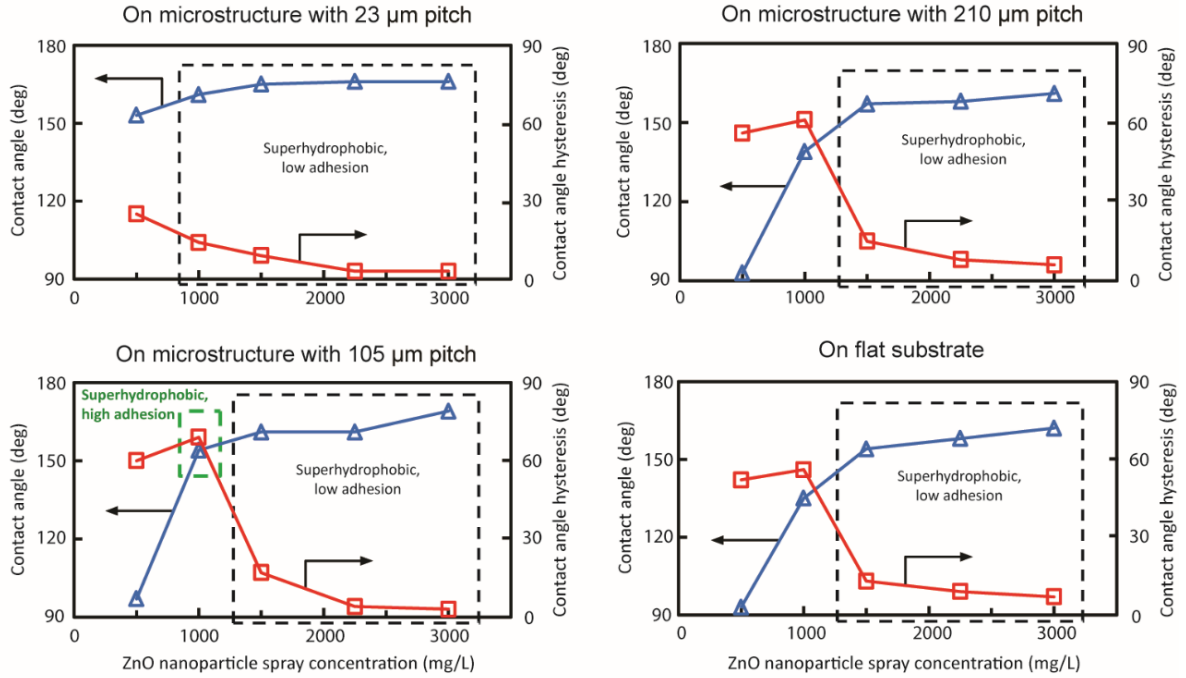


Figure 31: Contact angle and contact angle hysteresis data on nanostructured surfaces with hydrophobic ZnO nanoparticles (after modification with octadecylphosphonic acid (ODP)) using microstructures with three different pitch values (23 μm , 105 μm , 210 μm) as well as a flat substrate. Reproducibility is $\pm 1^\circ$ for CA data and $\pm 2^\circ$ for CAH data. “Low adhesion” indicates CAH < 30°, while “high adhesion” indicates adherence of droplet to an inverted substrate. Lines between data points are intended only to guide the eyes and not for interpolation (Ebert and Bhushan, 2012b).

A superhydrophobic, high adhesion state using hydrophobic particles occurred with a nanoparticle concentration of 1000 mg/L on the microstructure with 105 μm pitch. The measured CA and CAH were 154° and 69° , respectively, and a water droplet could remain adhered to the surface when inverted. The microstructure with 105 μm pitch and an individual micropillar with nanoparticles deposited at 1000 mg/L spray concentration can be seen in **Fig. 27b**. The data indicate that with properly selected microstructure geometry and nanostructure density, a superhydrophobic, high adhesion state can be achieved with a hydrophobic nanostructure. This finding is in agreement with Bhushan and Her (2010).

Table 3 shows measured CA and CAH values for three selected surfaces using hydrophobic nanoparticles, as well as calculated CA using both Wenzel and Cassie-Baxter equations (Eqs. (2) and (3) given in section 1.2). The values for R_f and f_{LA} were found as described previously. The CA of the ODP-modified ZnO without roughness (θ_0) was taken as 103° , which was the measured CA value on a glass slide modified by the same ODP solution. For the surface with 105 μm pitch and 1000 mg/L nanoparticle concentration, the measured CA of 154° is underpredicted by the Wenzel equation (136°) and overpredicted by the Cassie-Baxter equation (178°). As the CAH is high (69°) and pitch and concentration of 3000 mg/L, the measured CA (169°) is overpredicted, but CAH is extremely low (3°), indicating predominantly Cassie-Baxter behavior. **Figure 32** shows images of the droplet on 105 μm pitch microstructures with two different nanoparticle concentrations, leading to both high adhesion and low adhesion states. In

Table 3: Summary of measured and calculated contact angle (CA) and measured contact angle hysteresis (CAH) for selected superhydrophobic surfaces with high and low adhesion using hydrophobic ZnO nanoparticles. Data for hierarchical structure correspond to final samples (Ebert and Bhushan, 2012b).

	R_f	f_{LA}	CA measured (deg) ($\pm 1^\circ$)	CA calculated using Wenzel equation (Eq. 2) (deg)	CA calculated using Cassie-Baxter equation (Eq. 3) (deg)	CAH measured (deg) ($\pm 2^\circ$)
23 μm pitch with 1000 mg/L ZnO nanoparticle spray; superhydrophobic with low adhesion						
nanostructure	2.1	0.91	135	118	162	56
bare microstructure	3.5	0.71	152	53	122	37
hierarchical structure	4.6	0.97	161	~ 180	~ 180	14
105 μm pitch with 1000 mg/L ZnO nanoparticle spray; superhydrophobic with high adhesion						
nanostructure	2.1	0.91	135	118	162	56
bare microstructure	1.1	0.98	77	79	167	72
hierarchical structure	3.2	0.99	154	136	178 ^a	69
105 μm pitch with 3000 mg/L ZnO nanoparticle spray; superhydrophobic with low adhesion						
nanostructure	4.0	0.98	162	154	176	7
bare microstructure	1.1	0.98	77	79	167	72
hierarchical structure	5.1	0.99	169	~ 180	~ 180	3

^aOverprediction of CA by Cassie-Baxter equation, along with high CAH, suggests impregnating regime

Shape of droplets on hierarchical structure with 105 μm pitch and hydrophobic ZnO nanoparticles

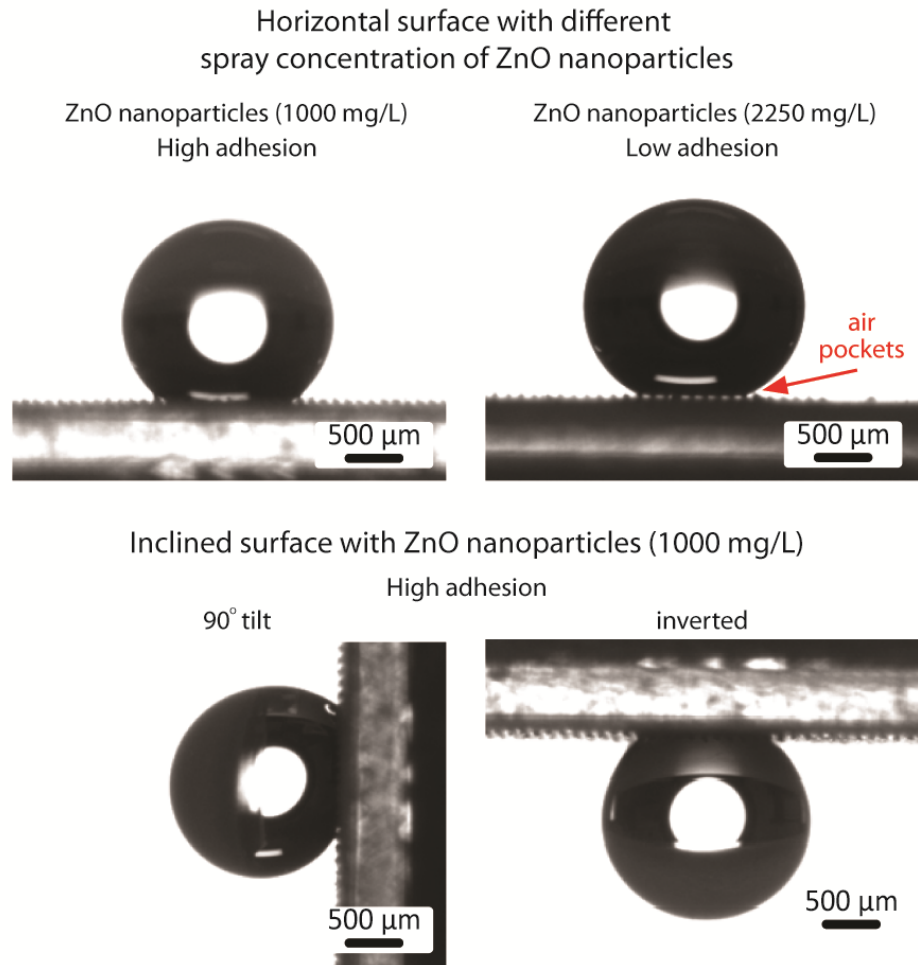


Figure 32: Droplets on hierarchically structured surfaces with microstructure pitch value of 105 μm and two different spray concentrations (1000 mg/L and 2250 mg/L) of hydrophobic ZnO nanoparticles resulting in superhydrophobicity with high adhesion (with 1000 mg/L) and low adhesion (with 2250 mg/L). In the case of low adhesion, air pockets are visible beneath droplet. Droplet in high adhesion state is also shown at 90° tilt and fully inverted (Ebert and Bhushan, 2012b).

addition, the droplet in high adhesion state is shown at vertical tilt and upside-down. For the low adhesion state, air pockets between micropillars are visible beneath the droplet.

3.3.3 Wear resistance in AFM sliding wear experiment

The results of the AFM sliding wear experiment for hydrophobic ZnO nanoparticles as well as the epoxy resin are shown in **Fig. 33**. Surface height maps before and after the wear experiment are displayed, as well as sample scans across the middle of the image (position indicated by arrow). Root mean square roughness (RMS) and peak-valley roughness (PV) within the wear area are also displayed. Hardness of the epoxy resin was measured with a microindenter (Micromet 3 Micro Hardness Tester) and found to be 570 MPa. The hardness of ZnO is approximately 5 GPa (Kucheyev *et al.*, 2002). After 1 cycle at 10 μ N with the borosilicate ball, the morphology of the surface with ZnO nanoparticles was not significantly changed, and RMS and PV of the sample scans within the wear area were nearly identical (455 nm after compared with 463 nm before for RMS, 1782 nm after and 1759 before for PV). The after-image for the epoxy resin reveals slight wear, as well as an overall swelling of the wear area, possibly due to frictional heating effects. In addition, RMS of the sample scan increased from 25 nm to 177 nm within the wear area, and PV increased from 48 nm to 286 nm. However, the preservation of nearly identical roughness and surface morphology for ZnO nanoparticles and fairly minimal wear of the epoxy resin indicates mechanical strength of the epoxy resin, sufficient hardness of

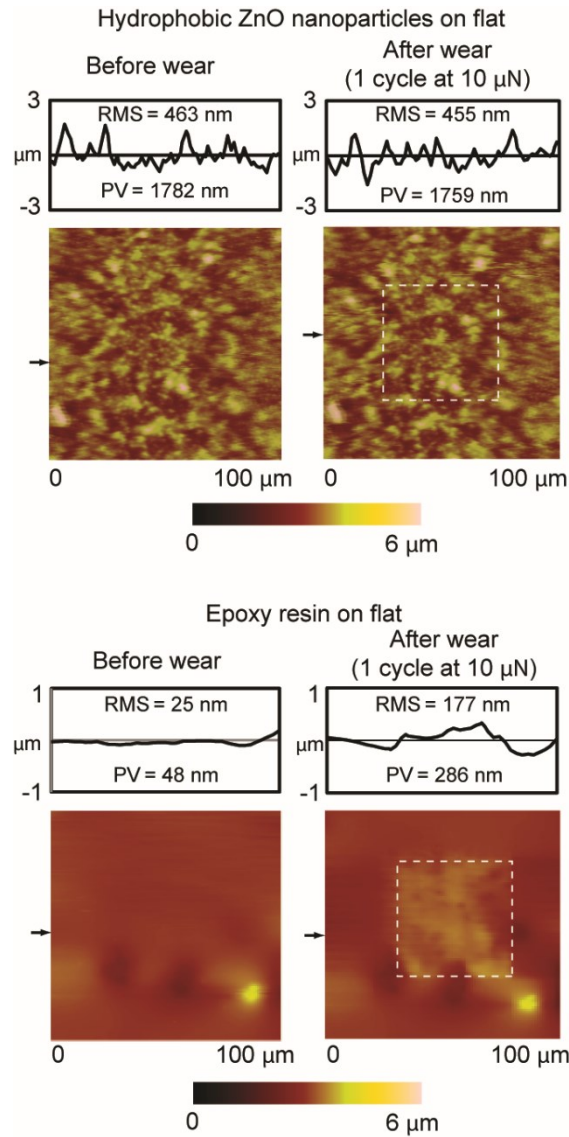


Figure 33: Surface height maps and sample surface profiles (locations indicated by arrows) before and after AFM sliding wear experiment using 15 μm radius borosilicate ball at load of 10 μN for glass samples with hydrophobic ZnO nanoparticles on flat substrate as well as epoxy resin alone on flat substrate. RMS roughness and PV distance values for surface profiles are displayed within surface profile boxes (Ebert and Bhushan, 2012b).

nanoparticles, and strong anchoring of particles in the epoxy resin layer. The resistance of structured surfaces to mechanical wear is critical to durability in industrial applications.

3.4 Conclusions

In this study, surfaces with the Rose Petal Effect (superhydrophobic with high droplet adhesion) were created using both hydrophilic and hydrophobic nanoparticles on microstructured and flat substrates. The impregnating wetting regime is responsible for this wetting behavior, in which liquid penetrates between microstructures but is only partially able to penetrate between nanostructures. In addition, the surfaces showed wear resistance for potential commercial use in an AFM wear experiment, indicating strong bonding of the epoxy resin and sufficient hardness of ZnO nanoparticles and resin.

With hydrophilic nanoparticles, the Rose Petal Effect could be achieved with high nanoparticle spray concentration (3000 mg/L) on a flat substrate. Droplets on this surface had a CA of 151° , CAH of 71° , and remained adhered when the surface was inverted. The high nanoparticle concentration created high surface roughness, which is necessary to obtain a superhydrophobic state using hydrophilic materials. However, the high roughness precluded the use of a microstructure of the geometry and the range of pitch values used in this study, as the roughness resulted in a predominantly Cassie-Baxter state on the microstructure with low droplet adhesion.

With hydrophobic nanoparticles, the Rose Petal Effect was achieved with significantly lower nanoparticle spray concentration (1000 mg/L) on a microstructure

with 105 μm pitch. Droplets on this surface had a CA of 154° , CAH of 69° , and could likewise remain adhered to an inverted substrate. Increasing nanoparticle concentration or decreasing microstructure pitch resulted in a Cassie-Baxter state with low adhesion. Conversely, decreasing nanoparticle concentration or increasing microstructure pitch resulted in a loss of superhydrophobicity. This is in agreement with results of previous studies using a hydrophobic nanostructure for high adhesion surfaces.

To summarize, wear-resistant surfaces with the Rose Petal Effect can be fabricated with either hydrophilic or hydrophobic materials by creating appropriate micro- and nanoscale surface structures. However, the hydrophilicity/hydrophobicity of material forming the nanostructure greatly affects the required nanostructure density, microstructure pitch value, and roughness necessary to achieve superhydrophobicity combined with high adhesion (i.e., droplet remains pinned to an inverted substrate). Use of a hydrophobic nanostructure may be preferable considering that a lower surface roughness is required.

CHAPTER 4: Superhydrophobic Surfaces with High Optical Transmittance on Glass and Polymer Substrates Using Dip-Coated Nanoparticles

4.1 Introduction

Superhydrophobicity is generally desired to achieve characteristics such as self-cleaning, antifouling and fluid drag reduction (Nosonovsky and Bhushan, 2008; Bhushan, 2011, 2016). However, for applications such as self-cleaning windows, optical devices, and solar panels, high optical transparency is additionally required. For example, typical requirements for an automotive windshield are optical transmittance $> 90\%$, 10,000 cycles of wiper sliding, and 250 car wash cycles, the last two requirements representing 10 years of life.

The multiple requirements of superhydrophobicity and optical transparency for these applications pose a challenge in design and fabrication. The surface must be sufficiently rough to support stable Cassie-Baxter wetting in order to obtain high CA and low CAH, but the dimensions of the roughness features must be small enough to preserve high optical transmittance of light. It is usually suggested that the size of surface features should not exceed roughly one quarter of the wavelength of visible light (around 100 nm or less) (Nakajima *et al.*, 1999; Manca *et al.*, 2009; Xiu *et al.*, 2009; Yanagisawa *et al.*, 2009; He *et al.*, 2011; Karunakaran *et al.*, 2011).

While glass is the most common optical material for lenses, architectural windows, *etc.*, transparent polymers such as polycarbonate (PC) and poly(methyl methacrylate) (PMMA) are also of great engineering importance. PC and PMMA are used for wide-ranging applications such as aircraft canopies, bullet-proof windows, solar cell panels, laptop computer screens, and many high-performance optical, electronic and medical devices. Silica (SiO₂), zinc oxide (ZnO), and indium tin oxide (ITO) thin films are of interest for varying applications. Select properties and potential benefits of SiO₂, ZnO, and ITO are shown in **Table 4**. The three metal oxides have high optical transmittance for

Table 4: Typical values for optical properties, electrical resistivity, and hardness for SiO₂, ZnO, and indium tin oxide (ITO) (Ebert and Bhushan, 2012c)

Particle	Band gap energy (band gap wavelength)	Refractive index	Hardness (GPa)	Electrical resistivity (Ω cm)	Potential benefits
SiO ₂	8.9 eV (138 nm) ^a	1.5 ^b	9 ^c	1 x 10 ¹⁸ d	Optical transparency, high hardness
ZnO	3.3 eV (375 nm) ^e	2.0 ^f	5 ^g	28 ^h	UV-protective effect
ITO	3.6 eV (345 nm) ⁱ	1.8 ^f	7 ^j	2-4 x 10 ⁻⁴ k,l	Optically transparent conducting oxide

^aSchneider and Fowler, 1976

^bMalitson, 1965

^cVila *et al.*, 2003

^dShackelford and Alexander, 2001

^eSrikant and Clarke, 1998

^fYang *et al.*, 2006

^gKucheyev *et al.*, 2002

^hNatsume and Sakata, 2000

ⁱHamberg and Granqvist, 1984

^jZeng *et al.* 2003

^kKim *et al.* 1999

^lEderth *et al.* 2003

due to low refractive indices (minimizing reflectance) and band gap wavelengths shorter than the visible range of 400-700 nm (minimizing visible-range absorption). SiO₂ in particular has extremely high optical transmittance. ZnO thin films can have a UV-protective effect, and have been shown to reduce photodegradation of PC (Moustaghfir *et al.*, 2004). When doped with other metals such as Al or Ga, ZnO can also be used for transparent conducting films (Noh *et al.*, 2010; Park *et al.*, 2010). ITO is the most commonly used material for transparent conducting films due to its combination of high optical transmittance and low electrical resistivity (Kim *et al.*, 1999; Ederth *et al.*, 2003; Cho *et al.*, 2006). In addition, these particles have high hardness (Kucheyev *et al.*, 2002; Vila *et al.*, 2003; Zeng *et al.*, 2003). Thus, SiO₂, ZnO, and ITO nanoparticles would seem to be suitable candidates for wear-resistant, transparent, superhydrophobic surfaces.

Tables 5 and 6 provide a representative summary of published work on transparent, superhydrophobic surfaces. **Table 5** summarizes surfaces created on glass substrates, while **Table 6** summarizes surfaces created on transparent polymers. In the case of glass, nanostructuring has generally been achieved through dip coating or spin coating of nanoparticles. For polymers, plasma etching techniques have also commonly been used. Several of the studies have reported optical transmittance approaching 100%, with a few even reporting enhanced optical transmittance compared to the uncoated substrate due to an antireflective effect (Bravo *et al.*, 2007; Li *et al.*, 2009; Manca *et al.*, 2009). However, many of the surfaces created required post-fabrication treatment with fluorosilane or other low surface energy substance to achieve superhydrophobicity. In some cases, CAH and/or tilt angle (TA), which are important for self-cleaning ability, are not reported. In

Table 5: Summary of recent studies in fabricating transparent superhydrophobic surfaces on glass substrates (Ebert and Bhushan, 2012c)

Nanostructure	Deposition or fabrication method	Surface post-treatment	CA	CAH or TA	Optical transmittance	Mechanical wear experiments	References
Ta ₂ O ₅	Sputter	Fluorocarbon	155°	20°	~82%		Manakasettham <i>et al.</i> (2012)
ZnO	Spray pyrolysis		154°		85%		Tarwal <i>et al.</i> (2010)
Boehmite	Spin coat	Fluorosilane	163°		94%	Cotton rubbing	Yanagisawa <i>et al.</i> (2009)
CNT, SiO ₂	Spray		153°	>10°	93%		Han <i>et al.</i> (2008)
SiO ₂ , fluorocarbon	MW plasma		156°	5°	100%	Waterfall	Irzh <i>et al.</i> (2011)
SiO ₂ , PDMS	Spin coat	Chlorosilane	153°	<1°	~93%	Ultrasonic damage, tape adhesion	He <i>et al.</i> (2011)
SiO ₂ , polystyrene	Dip coat	Fluorocarbon	160°	1°-4°	100%	Water drip	Xu <i>et al.</i> (2009), Cao and Gao (2010)
SiO ₂	Dip coat		171°		90%		Kavale <i>et al.</i> (2011)
SiO ₂	Dip coat	Fluorosilane, chlorosilane	152°-172°	< 7°	90-100%	Tape adhesion, sand grain impact	Bravo <i>et al.</i> (2007), Li <i>et al.</i> (2009), Ling <i>et al.</i> (2009) Deng <i>et al.</i> (2011), Karunakaran <i>et al.</i> (2011)
SiO ₂	Spin coat		160°-179°	1°-5°	80-100%	Water drip, tape adhesion, outdoor exposure	Manca <i>et al.</i> (2009), Cho <i>et al.</i> (2010), Budunoglu <i>et al.</i> (2011), Xu <i>et al.</i> (2012)
SiO ₂	Spin coat	Fluorosilane	168°-170°	4°-11°	100%		Su <i>et al.</i> (2006), Xiu <i>et al.</i> (2009)

CA – contact angle

CAH – contact angle hysteresis

TA – tilt angle

many cases, mechanical wear experiments are either absent or lack a quantitative approach. Fewer studies have used polymer substrates as compared to glass. Notably, SiO₂ nanoparticles have been the overwhelming favorite to provide a nanostructure, while studies using other particles such as ZnO have been less common. The use of ITO nanoparticles to create superhydrophobic surfaces has not been found in the literature. In order to capitalize on the unique properties that different nanoparticles offer, as well as

Table 6: Summary of recent studies in fabricating transparent superhydrophobic surfaces on polymer substrates (Ebert and Bhushan, 2012c)

Substrate	Nanostructure	Deposition or fabrication method	Surface post-treatment	CA	CAH or TA	Optical transmittance	Mechanical wear experiments	References
PC	SiO ₂ , fluorocarbon	MW plasma		156°	5°	90%	Waterfall	Irzh <i>et al.</i> (2011)
PDMS	Substrate itself	Lithography	Fluoropolymer	153°	18°	94%	Water droplet impingement	Im <i>et al.</i> (2010)
PDMS	Substrate itself (microstructured)	Lithography	Fluorosilane	145°	~30°			Dufour <i>et al.</i> (2010)
PMMA	Substrate itself	Plasma etch	Fluorocarbon	152°	5°		Waterfall	Vourdas <i>et al.</i> (2007)
PET	Substrate itself	Plasma etch	Fluorosilane	150°		90%		Teshima <i>et al.</i> (2005)
PET	SiO ₂	Spin coat	Fluorosilane	150°	< 2°	80%	Cloth rubbing	Hikita <i>et al.</i> (2005)
PET	Al ₂ O ₃	Dip coat	Fluorosilane	150°		90%	Tape adhesion	Tadanaga <i>et al.</i> (2003)

CA – contact angle

CAH – contact angle hysteresis

TA – tilt angle

expand potential applications, fabrication techniques should be developed that are suitable for a variety of nanoparticles and optical substrates.

The motivation of this work was to achieve surfaces that simultaneously exhibit Lotus Effect characteristics and high optical transparency for applications such as self-cleaning windows and solar panels. The objective of the study was to design and optimize a versatile dip coating technique to create transparent, superhydrophobic surfaces on multiple substrate types (glass, PC, and PMMA) using multiple types of nanoparticles (SiO₂, ZnO, and indium tin oxide (ITO)) that have potential benefits as outlined in **Table 4**. A study using a single technique to create transparent, superhydrophobic surfaces with such a variety of materials has not been performed. In addition, particles were hydrophobized before fabrication of surfaces, and no chemical post-treatment of the

prepared surfaces was required to render them superhydrophobic. As hydrophobized particles are often available commercially, the elimination of the need for surface post-treatment may simplify the fabrication process and reduce costs, particularly for surfaces with large area. In addition, for many polymer substrates, some post-treatment techniques such as vapor deposition or plasma may be undesirable. The samples were characterized in terms of wettability (CA and CAH) and optical transmittance in the visible spectrum. Wear resistance experiments were conducted using an atomic force microscope and a water jet apparatus to examine sliding wear and impingement of water jet.

4.2 Experimental details

4.2.1 Materials

Soda-lime glass (2.2 mm thick), polycarbonate (Lexan, SABIC Innovative Plastics, 2.4 mm thick), and PMMA (Optix, Plaskolite Inc., 2 mm thick) were used to create 1 cm x 1 cm substrates. Silane-modified hydrophobic SiO₂ nanoparticles with average diameter of 55 nm (± 15 nm) were obtained from Evonik Industries (AEROSIL RX 50). ZnO nanoparticles with average diameter of 70 nm (± 30 nm) were obtained from Alfa Aesar (NanoTek Zinc Oxide). ITO nanoparticles (90:10 In₂O₃:SnO₂) of average diameter 45 nm (± 25 nm) were obtained from US Research Nanomaterials (US3855 Indium Tin Oxide Nanopowder). Octadecylphosphonic acid (ODP) was purchased from Aldrich, and methylphenyl silicone resin was obtained from Momentive Performance Materials (SR355S Methylphenyl Silicone Resin).

4.2.2 Functionalization of nanoparticles and dip coat procedure

While the SiO₂ particles were obtained already silane-modified, the ZnO and ITO particles were not surface-modified as received. The particles were hydrophobized using octadecylphosphonic acid using the method described in section 3.2.1 and shown schematically in **Fig. 26**. Approximately 2 g of particles were added to a 100 mL ethanol solution with ODP concentration of 2 mM. The mixture was stirred vigorously for 10 min, covered, and left for 4 days at 20 °C. The solvent was then removed by evaporation, and the particles were heated at 100 °C for 1 hour to improve ODP bonding and remove adsorbed water or remaining solvent.

Particles were dispersed in a 40%/60% THF/IPA (by volume) mixture to form the dip coating solution. While pure THF rapidly dissolves PC and PMMA resulting in complete loss of optical transmittance, it was found that when THF concentration was kept below approximately 50% by volume in IPA, substrates could be dipped for over one minute without visible damage or loss of optical transmittance. A dip coating solution of pure IPA, however, does not evaporate quickly or evenly enough to leave a homogeneous coating on the substrate. Optimal concentrations of nanoparticles in the solvent were found to be approximately 10 mg/mL for SiO₂ particles, 35 mg/mL for ZnO particles, and 50 mg/mL for ITO particles. Too low of a concentration resulted in loss of superhydrophobicity, while too high of a concentration resulted in visible agglomeration of particles on substrates, substantially reducing optical transmittance.

The functionalized nanoparticles were added to 30 mL of the THF/IPA solvent in a 100 mL glass beaker and sonicated for 4 min with a Branson Sonifier 450A (20 kHz

frequency at 35% amplitude). Then, 150 mg of methylphenyl silicone resin was added and the mixture was sonicated for an additional 4 min. In the case of the silicone resin, a concentration significantly below this optimal level resulted in poor adherence of the particles to the substrate. Concentration significantly above this level resulted in loss of superhydrophobicity, likely due to the complete engulfing of particles in the resin layer. In addition to ultimately acting to bind nanoparticles to the substrates, the silicone resin worked excellently as a dispersant in the dip coating solution. For ITO particles in particular, settling was noticeable within seconds when silicone resin was not added, but particles remained homogeneously dispersed with resin included. After sonication, approximately 10 mL of fresh solvent was added at 40%/60% THF/IPA ratio. Substrates were dipped into the solution and immediately removed at a speed of 10 cm/min. Coated samples were then heated at 40 °C for 10 min to remove any remaining solvent. The samples required no chemical post-treatment or modification after dip coating. A schematic of the dip coat procedure is shown in **Fig. 34**.

4.2.3 Characterization of dip-coated glass and polymer samples

For wettability measurements, water droplets of 5 μ L volume (\sim 1 mm radius) were deposited onto samples using a microsyringe. CA and CAH were measured using a model 290-F4 Ramé-Hart goniometer (Ramé-Hart Inc., Succasunna, NJ). CAH was determined using the tilt method shown in **Fig. 4b**. Reproducibility of all CA and CAH data is reported as ($\pm\sigma$) as determined from measurement on five samples. Values for f_{LA} were estimated using SPIPTM imaging software (Image Metrology). Optical transmittance

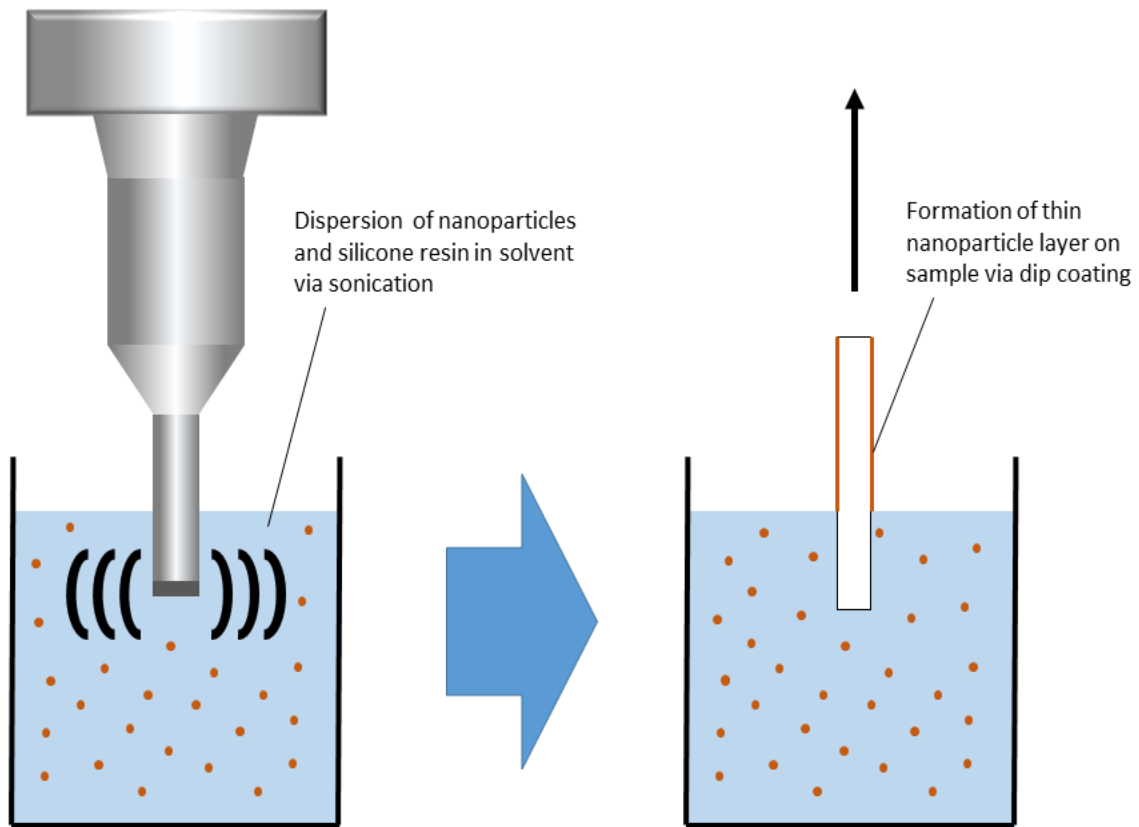


Figure 34: Simplified schematic of dip coat procedure used to create transparent, superhydrophobic nanoparticle coatings on glass, polycarbonate, and PMMA substrates. The mixture of nanoparticles (SiO_2 , ZnO , or indium tin oxide (ITO)), silicone resin, and solvent is first sonicated to ensure dispersion in the solvent. Then, substrates are dipped and slowly removed vertically from the mixture, leaving a thin nanoparticle layer that is strongly bonded to the substrate by the silicone resin after annealing.

measurements were performed using an Ocean Optics USB400 spectrometer (Ocean Optics Inc., Dunedin, FL) with a 200 μm aperture width. All transmittance data is reported for a one-sided coating as a percentage of the transmittance of the uncoated substrate in the visible spectrum (400-700 nm).

To examine the wear resistance of the samples, wear experiments were performed using an AFM and water jet apparatus. In order to study sliding wear resistance, an established AFM wear experiment (Bhushan, 2011; Jung and Bhushan, 2009; Ebert and Bhushan, 2012a) was performed as described in section 2.3.3 with a commercial AFM (D3100, Nanoscope IIIa controller, Digital Instruments, Santa Barbara, CA). For wear experiments, investigation of single asperity contact is necessary to understand fundamental interfacial phenomena. An AFM tip can simulate single asperity contact for micro/nanostructured surfaces (Bhushan, 2011). Samples with SiO_2 , ZnO, and ITO nanoparticles on glass substrates were worn using a borosilicate ball with radius 15 μm mounted on a rectangular Si(100) cantilever ($k = 7.4 \text{ N/m}$) in contact mode. Areas of 50 x 50 μm^2 were worn for 1 cycle at a load of 10 μN . To analyze the change in the morphology of the surfaces before and after the wear experiment, height scans of 100 x 100 μm^2 in area were obtained using a rectangular Si(100) tip ($f = 76 \text{ kHz}$, $k = 3 \text{ N/m}$) in tapping mode. As a baseline, the wear results for the samples were compared to that of the silicone resin alone on a glass substrate.

An established water jet procedure, described in section 2.3.3 and illustrated in **Fig. 19**, was performed to examine macroscale wear resistance of the samples in water flow. For applications involving self-cleaning glass, resistance to impingement of water is of

critical interest. Samples were exposed to the water jet at different kinetic energy levels by varying the pressure of the water ejected from the nozzle. The samples were placed 2 cm below the four holes in the pipe, and the runoff plate was tilted at 45°. The exposure time was 20 min at each pressure. After each experiment, the CA and CAH of the samples were measured as described previously. The results for the coated samples were compared to a baseline sample of silicone resin alone on a glass substrate.

4.3 Results and discussion for dip-coated glass and polymer samples

The nine types of transparent superhydrophobic samples using three different nanoparticles (SiO₂, ZnO, ITO) on three different substrates (glass, PC, PMMA) are discussed below. First, roughness values and surface morphology are presented. Then, the CA, CAH, and optical transmittance of samples are reported, discussing trends in the data. Lastly, the results of the wear resistance experiments are examined.

4.3.1 Surface roughness and morphology

Table 7 displays RMS roughness, PV (peak-valley) distance, roughness factor (R_f), coating thickness, and estimated liquid-air fractional area (f_{LA}) for samples with SiO₂, ZnO, and ITO. Surfaces had nanoscale roughness formed by nanoparticles bound to the substrate with silicone resin. The values of R_f were calculated using AFM surface height maps as described in section 3.3.1 and shown in **Fig. 29**. By using the Z-height of each data point in the AFM scan matrix, the real surface area can be approximated using

Table 7: Measured roughness values (RMS, PV, and R_f), coating thickness, and estimated liquid-air fractional area (f_{LA}) for samples with SiO₂, ZnO, and indium tin oxide (ITO) (Ebert and Bhushan, 2012c)

Particles on sample	RMS (nm)	PV (nm)	R_f	Coating thickness (nm)	f_{LA}
SiO ₂	58 ± 3	137 ± 5	1.5	150 ± 10	0.94
ZnO	84	191	1.8	205	0.94
ITO	45	127	1.3	135	0.91

simple geometry. Dividing this value by the two-dimensional scan area gives R_f . The values of f_{LA} were estimated using AFM maps with SPIPTM imaging software (Image Metrology) with the assumption that the droplet contacts only the highest peaks of surface asperities, which is characteristic of a stable Cassie-Baxter regime. Based on this assumption, threshold height criteria can be selected for image processing and applied consistently across all samples to determine estimated f_{LA} values so that the differences between measured and calculated CA and CAH for different nanoparticle coatings can be compared. Coating thicknesses were measured with a Tencor® stylus profiler on the step formed by partially coating a substrate, and found to be nearly equal to PV distance. **Figure 35** shows SEM micrographs of sample surfaces using each of the three nanoparticles on glass substrates at two magnifications. At lower magnification, the

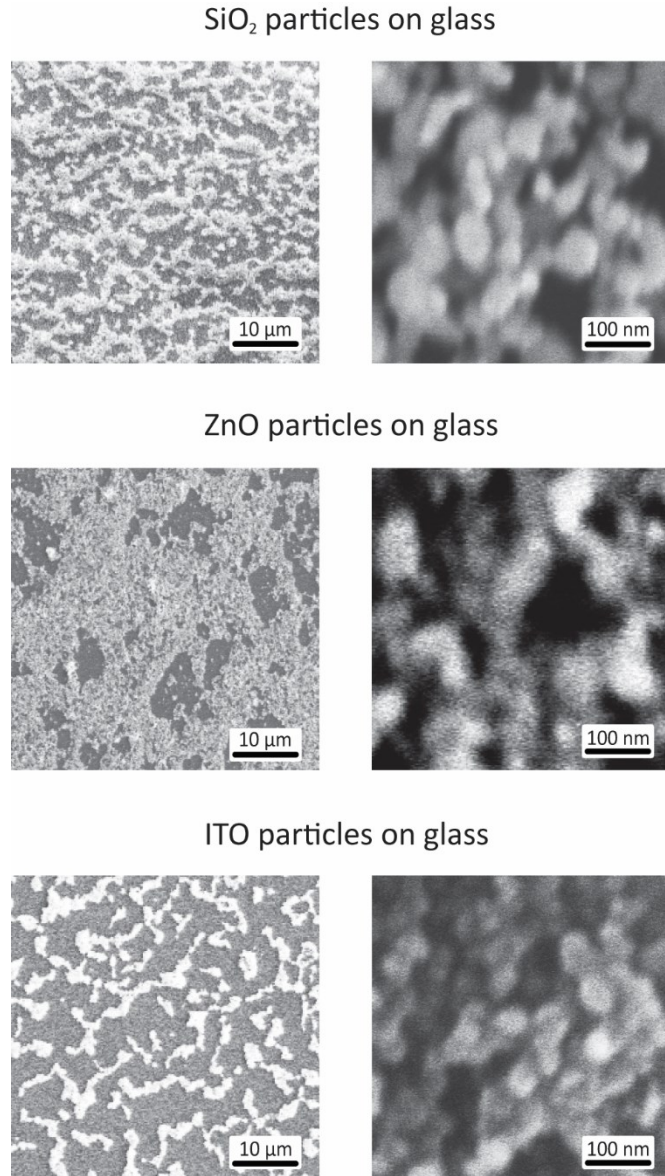


Figure 35: SEM micrographs of SiO₂, ZnO, and indium tin oxide (ITO) nanoparticle coatings on glass substrates at two magnifications each showing nanoscale roughness (Ebert and Bhushan, 2012c)

particles can be seen to form islands with width on the order of a few microns. The solution with ZnO nanoparticles, which resulted in highest PV and RMS roughness (see Table 7), tended to cover more of the substrate, but less evenly and with larger pockets of uncoated area. The solution with ITO nanoparticles tended to coat in a more regular pattern and with smallest islands. These coatings had lowest PV and RMS roughness. The solution with SiO₂ nanoparticles tended to coat with a fairly regular pattern, but with structures more densely packed than in the case of ITO solution. The SiO₂ coatings had PV and RMS roughness intermediate to ZnO and ITO. At higher magnification, individual nanoparticles can be seen forming roughness on the nanoscale, which suggests the particles are well-dispersed in solution. While there were some differences in the coating tendencies of the three nanoparticle solutions, they were all seen to form closely packed roughness features that did not exceed ~ 200 nm in PV height. This roughness is desirable for superhydrophobicity (Bhushan, 2016).

4.3.2 Wettability and optical transmittance

Data for samples using three different nanoparticles (SiO₂, ZnO, ITO) on three different substrates (glass, PC, PMMA) are shown in **Table 8** (data shown graphically in **Fig. 36**). CA, CAH, and optical transmittance are reported for each of the nine sample types. All samples exhibited superhydrophobic, self-cleaning behavior, with CA nearly 170° and CAH as low as 1° in some cases. For all three particles, CA was slightly higher on PC and PMMA substrates than on glass. CAH was slightly higher on glass substrates, except in the case of ZnO where it was unchanged at 1°. For all substrates, the samples

Table 8: Wettability and optical transmittance data for all dip-coated samples using SiO₂, ZnO, and indium tin oxide (ITO) nanoparticles (Ebert and Bhushan, 2012c)

Particle Substrate	SiO ₂ (55 nm) (Silane modified)			ZnO (70 nm) (ODP modified)			ITO (45 nm) (ODP modified)		
	CA	CAH	T*	CA	CAH	T*	CA	CAH	T*
Glass (soda-lime)	165° (±2°)	3° (±1°)	90% (±0.25%)	165°	1°	87%	154°	7°	93%
Polycarbonate	167°	1°	93%	168°	1°	88%	159°	3°	95%
PMMA	166°	1°	96%	169°	1°	92%	161°	3°	97%

*Average transmittance value across visible range (400-700 nm) as a percentage of the optical transmittance of the uncoated substrate

with ITO particles had lower CA and higher CAH than those with SiO₂ and ZnO, although self-cleaning conditions were still met (CA > 150° and CAH < 10°).

The Cassie-Baxter equation (Eq. (3) given in section 1.2) can be used to predict CA in the case where the droplet rests only on highest asperities, with air filling gaps between (Nosonovsky and Bhushan, 2008; Bhushan, 2016). In the case of full wetting with no air pockets (Wenzel regime), CA can be predicted by simply setting f_{LA} equal to zero in Eq. (3), which reduces it to the Wenzel equation (Eq. 2). AFM surface maps were analyzed and f_{LA} values (shown in **Table 7**) were estimated to be 0.94, 0.94, and 0.91 for SiO₂,

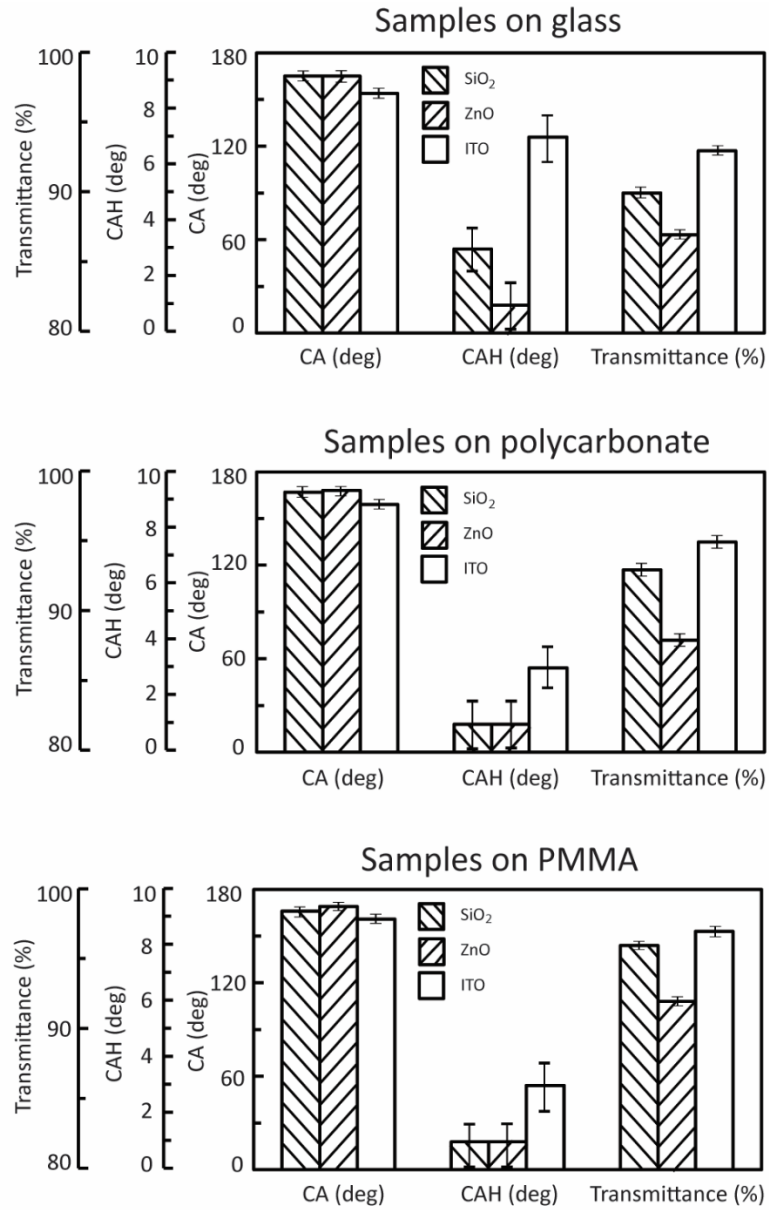


Figure 36: Bar chart showing contact angle (CA), contact angle hysteresis (CAH), and optical transmittance for samples with SiO₂, ZnO, and indium tin oxide (ITO) nanoparticles on glass, polycarbonate, and PMMA substrates. Error bars represent ±1 standard deviation (Ebert and Bhushan, 2012c).

ZnO, and ITO samples, respectively. The lower f_{LA} for samples with ITO nanoparticles may be due to the tendency to form more evenly distributed islands with lower height distribution compared to SiO₂ and ZnO, possibly due in part to smaller primary particle size. Thus, even while the roughness structures occupy less of the surface in a two-dimensional projection, the fraction of solid-liquid interface is higher because lower roughness results in the droplet resting on a greater number of peaks.

An estimation of CAH for superhydrophobic, low adhesion surfaces can be derived making the following assumptions: a high CA (approaching 180°), low CAH (approaching 0°), that Eq. (3) can be applied to the effect of adhesion hysteresis on CAH, and that the energy dissipation resulting in CAH is primarily due to adhesion hysteresis (Nosonovsky and Bhushan, 2008). This last assumption becomes valid when considering that a droplet with very high CA and very low CAH will be in Cassie-Baxter wetting regime. In Cassie-Baxter regime, the droplet rests only on the highest tips of asperities with very high liquid-air fraction of interface (f_{LA}), and roughness effects can be safely neglected. The work of adhesion hysteresis is proportional to the solid-liquid fraction of the interface (Nosonovsky and Bhushan, 2008):

$$\Delta W = R_f f_{SL} \Delta W_0 \quad (8)$$

where f_{SL} is the fraction of solid-liquid interface, and ΔW_0 is the work of adhesion hysteresis on a smooth surface. Applying Eq. (3) to the effect of adhesion hysteresis and using Eq. (8), it can be shown that the difference of cosines of the advancing and

receding CA (θ_{adv} and θ_{rec}) is related to the difference of cosines for a smooth surface (θ_{adv0} and θ_{rec0}) (Nosonovsky and Bhushan, 2008):

$$\begin{aligned} \cos \theta_{adv} - \cos \theta_{rec} &= \frac{\Delta W}{\gamma_{LA}} = \frac{R_f f_{SL} \Delta W_0}{\gamma_{LA}} \\ &= R_f f_{SL} (\cos \theta_{adv0} - \cos \theta_{rec0}) \end{aligned} \quad (9)$$

In Eq. (9), the contributions of the pinning effects of sharp edges and chemical heterogeneities are assumed to negligible, and adhesion hysteresis is considered the dominant contributor to CAH as mentioned above in the assumptions. Considering that as CA approaches 180° , $\cos \theta$ approaches $-1 + (\pi - \theta)^2 / 2$, that as CAH approaches 0° , $\theta_{adv} \approx \theta_{rec} \approx \theta$, and that $f_{SL} + f_{LA} = 1$ for the composite interface, Eq. (9) can be reduced to (Nosonovsky and Bhushan, 2008):

$$CAH \approx \frac{R_f \sqrt{1 - f_{LA}} (\cos \theta_{rec0} - \cos \theta_{adv0})}{\sqrt{2(R_f \cos \theta_0 + 1)}} \quad (10)$$

Table 9 shows measured and calculated CA and CAH values, with measured values taken from samples on glass substrates. Flat-surface angles (θ_0 , θ_{rec0} , and θ_{adv0}) were measured on a glass slide modified with the same ODP solution, and found to be $\theta_0 = 103^\circ$, $\theta_{rec0} = 75^\circ$, and $\theta_{adv0} = 132^\circ$. Comparison of the measured values to calculated Wenzel and Cassie-Baxter values strongly suggests a Cassie-Baxter regime, especially given the very low CAH values measured, which are typically associated with Cassie-Baxter wetting. Thus, the droplet predominantly contacts the highest peaks of the hydrophobic-modified nanoparticles. For CAH, Eq. (10) predicts essentially identical values of 0.3° , 0.4° , and 0.3° for SiO_2 , ZnO , and ITO , respectively. The lower measured

Table 9: Measured and calculated CA and CAH values for samples with SiO₂, ZnO, and indium tin oxide (ITO) nanoparticles. Measured values are taken from samples on glass substrates (Ebert and Bhushan, 2012c).

Particle type	CA measured	CA calculated using Wenzel equation (Eq. 2)	CA calculated using Cassie-Baxter equation (Eq. 3)	CAH measured	CAH calculated using Eq. (10)
SiO₂	165°	110°	164°	3°	< 1°
ZnO	165°	114°	165°	1°	< 1°
ITO	154°	107°	159°	7°	< 1°

CA and higher CAH for ITO compared to calculated values may suggest that a small fraction of the droplet contacts the substrate for ITO samples, leading to partial Wenzel wetting and higher hysteresis. This may be a result of the topography of microsized islands for ITO samples, which tended to be smaller and with greater distance between. In the case that the droplet interface exhibits a small fraction of Wenzel wetting behavior, the hydrophobicity of the silicone resin ($\theta_0 = 99^\circ$) may help to preserve superhydrophobicity (CA > 150°) and low CAH (< 10°) necessary for self-cleaning behavior.

The uncoated glass, PC, and PMMA substrates had optical transmittances of 92%, 87%, and 94%, respectively. Optical transmittances of the samples are reported as percentages of the optical transmittance of the uncoated substrate. **Table 8** shows the average values for samples across the visible spectrum (data shown graphically in **Fig. 36**). **Figure 37** shows optical transmittance data for SiO₂, ZnO, and ITO nanoparticles on all substrates. For all three particles, samples on PMMA had higher optical transmittance than those on PC, and PC samples had higher optical transmittance than those on glass, even with transmittances normalized by substrate transmittance. For all substrates, the samples with ITO particles had higher optical transmittance than those with SiO₂ particles, and SiO₂ samples had higher optical transmittance than those with ZnO. The lower optical transmittance of the ZnO samples likely owes to their significantly higher roughness values compared to ITO and SiO₂. Conversely, the higher optical transmittance of the ITO samples likely owes to their lower roughness, comparatively. Despite somewhat less favorable values for band gap and refractive index, the ITO samples had higher optical transmittance than SiO₂ samples, which suggests that in this case, roughness and coating thickness played a larger role in optical transmittance than did inherent optical properties of particles. This may be due to the fact that roughness and coating thickness values were on the order of the 100 nm approximate threshold for optical transparency.

The optical transmittance of the samples in the context of coating thickness is in rough agreement with other published studies: He *et al.* (2011) and Ling *et al.* (2009) reported optical transmittance of greater than 90% for coating thickness of 380 nm using

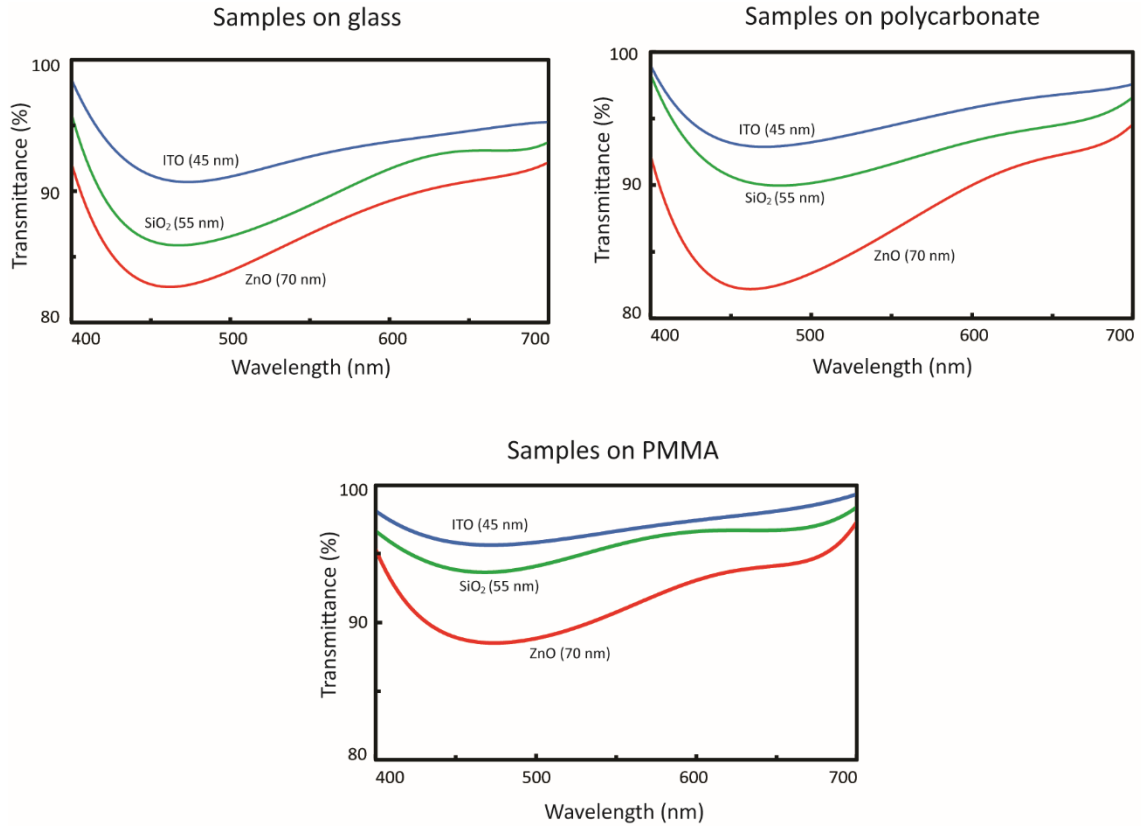


Figure 37: Transmittance spectra in the visible range ($\lambda = 400\text{-}700\text{ nm}$) for samples with silica (SiO_2), zinc oxide (ZnO), and indium tin oxide (ITO) nanoparticle coatings on glass, polycarbonate, and poly(methyl methacrylate) (PMMA) substrates. Data represent optical transmittance as a percentage of the optical transmittance of the uncoated substrate (Ebert and Bhushan, 2012c).

SiO_2/PDMS , and coating thickness of about 60 nm using SiO_2 , respectively. Data for SiO_2 samples in this study were intermediate, with optical transmittance values from 90-96% for coating thickness of 137 nm. Although very high transmittance values were achieved,

an antireflective effect resulting in optical transmittance greater than 100% of the uncoated substrate, as reported in some studies (Bravo *et al.*, 2007; Li *et al.*, 2009; Manca *et al.*, 2009), was not seen. In addition, the typical morphology of disconnected islands of particles, while beneficial for roughness and superhydrophobicity, disallows a path for electrical current. Further development of this technique would be necessary to prepare transparent, superhydrophobic coatings that are also electrically conductive. ITO-coated glass, PC, and PMMA samples with deposited water droplets can be seen in **Fig. 38**, showing superhydrophobicity and high optical transmittance of the coatings. Blue dye was added to water for visual clarity of droplets. A goniometer image of a droplet on ITO-coated glass is shown for better view of a superhydrophobic contact angle.

4.3.3 Wear resistance in AFM sliding wear and water jet experiments

The results of the AFM sliding wear experiment for SiO₂, ZnO, and ITO particles on glass as well as silicone resin alone on glass are shown in **Fig. 39**. Surface height maps before and after the wear experiment are displayed, as well as sample scans across the middle of the image (position indicated by arrow). Roughness values within the wear area (RMS and PV, before and after) are also displayed. Hardness of the silicone resin was measured with a microindenter (Micromet 3 Micro Hardness Tester) and found to be 1.3 GPa. The after-image of silicone resin alone reveals slight wear of the 50 x 50 μm² area worn by the borosilicate ball. The wear mode appears to be adhesive, as there is a fairly uniform removal of material (Bhushan, 2013a). However, morphology was not

Glass

Polycarbonate

PMMA



Shape of droplet on glass



Figure 38: Water droplets deposited on glass, polycarbonate, and PMMA with indium tin oxide (ITO) nanoparticle coatings showing superhydrophobicity and high optical transmittance (top). Blue dye was added to water for visual clarity of droplets. Goniometer image of droplet is shown for glass substrate with ITO coating (bottom) (Ebert and Bhushan, 2012c).

Wear experiment using AFM

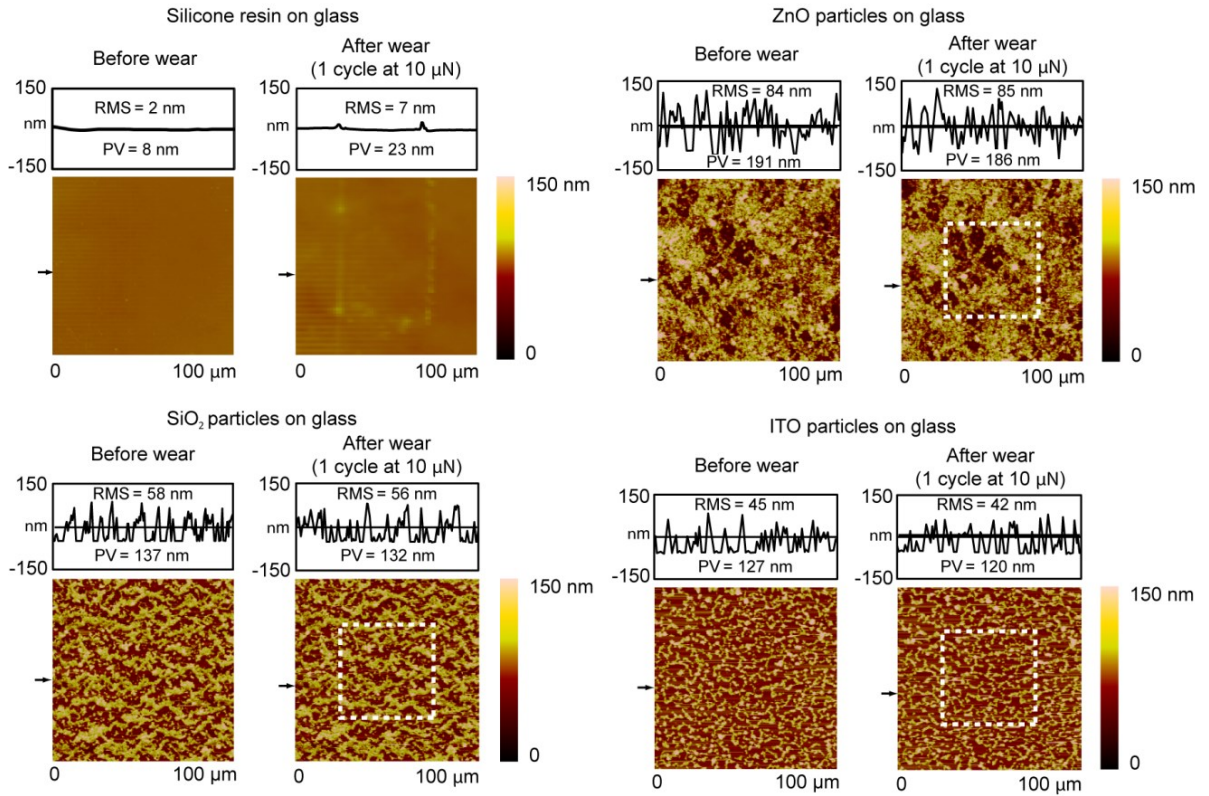


Figure 39: Surface height maps and sample surface profiles (locations indicated by arrows) before and after AFM sliding wear experiment using 15 μm radius borosilicate ball at load of 10 μN for glass samples with silicone resin alone, SiO₂ nanoparticles, ZnO nanoparticles, and indium tin oxide (ITO) nanoparticles. RMS roughness and PV distance values for surface profiles are displayed within surface profile boxes. Results shown are typical for all substrates (Ebert and Bhushan, 2012c).

significantly changed in the after-image for any of the three samples with nanoparticles, and RMS roughness and PV distance values remained similar. The minimal wear of the silicone resin and preservation of nearly identical roughness and surface morphology for samples indicates mechanical strength of the silicone resin, sufficient hardness of nanoparticles, and strong anchoring of particles in the silicone resin layer.

The results of the water jet experiment can be seen in **Fig. 40**. Samples were exposed to water jet for 20 min at each pressure ranging from 0 to 45 kPa. CA and CAH data are displayed for SiO₂ nanoparticles as well as silicone resin alone on glass substrates. For the samples with SiO₂ nanoparticles, superhydrophobicity and self-cleaning properties were maintained even at highest pressure, with CA decreasing from 165° to 160°, and CAH increasing from 3° to 6°. At some intermediate pressures, CAH as low as 1° was measured. The wettability of the samples with silicone resin was likewise not significantly changed, with CA of 97° at 45 kPa compared to an initial value of 99°. CAH for the silicone resin remained between 67° and 69° at all pressures. The results indicate wear resistance of the surfaces under impingement of water. This demonstrates durability of surfaces for applications such as self-cleaning windows and windshields.

4.4 Conclusions

A versatile dip coating technique was used in a systematic study to create transparent, superhydrophobic surfaces on glass and plastic substrates with SiO₂, ZnO, and indium tin oxide (ITO) nanoparticles. ZnO and ITO particles were hydrophobized with

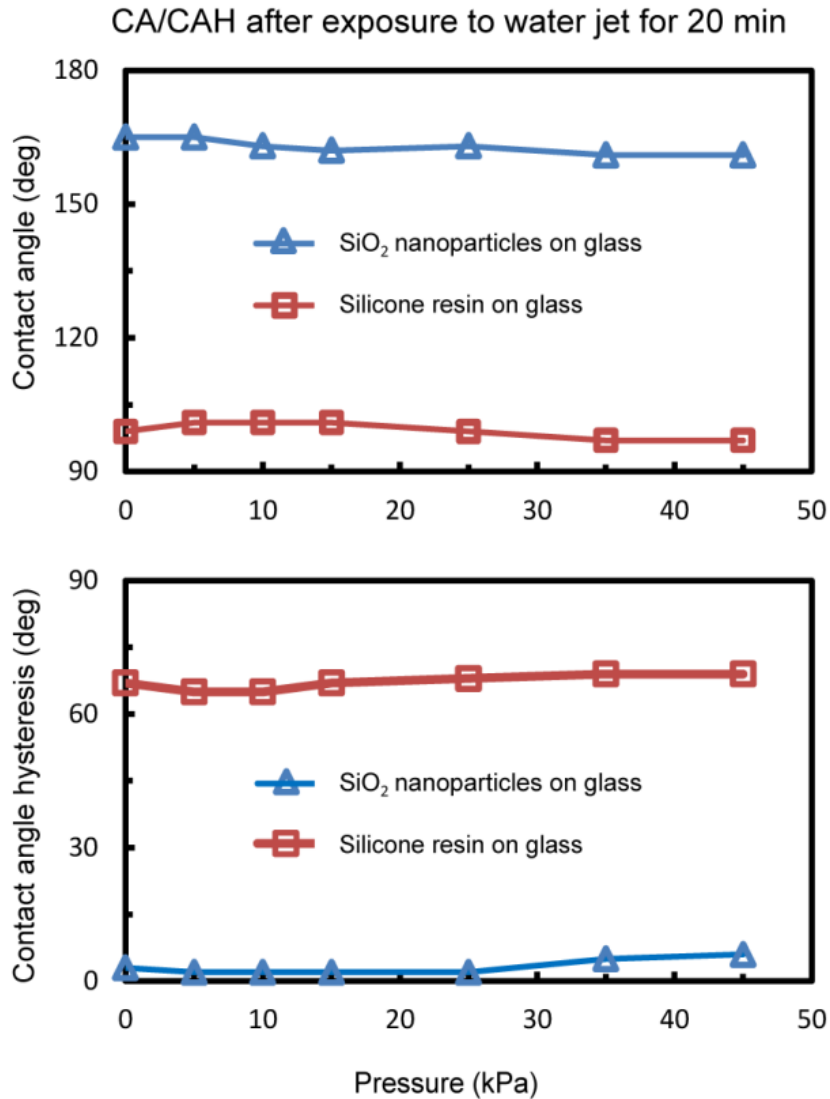


Figure 40: Contact angle (CA) and contact angle hysteresis (CAH) as a function of water pressure after 20 min. exposure time for samples with SiO₂ nanoparticles on glass and silicone resin alone on glass. Reproducibility is $\pm 1^\circ$ for CAH of SiO₂ nanoparticles, $\pm 2^\circ$ for CAH of silicone resin alone on glass, and $\pm 2^\circ$ for all CA data. Results shown are typical for all samples. CA $> 150^\circ$ and CAH $< 10^\circ$ were maintained in all cases. Lines between data points are intended to guide the eyes (Ebert and Bhushan, 2012c).

octadecylphosphonic acid (ODP), and the prepared samples did not require post-treatment with low surface energy substances. The nanoparticles showed different tendencies in the way they deposited onto substrates from dip coating, which may be partly due to differences in primary particle size. This caused variation in coating thickness and morphology between particles, which helps to explain differences in wettability and optical transmittance between samples. ITO samples had slightly lower CA and slightly higher CAH than SiO₂, ZnO, which is likely the result of a comparatively lower liquid-air fractional area (f_{LA}). Roughness and coating thickness seemed to influence optical transmittance more than inherent optical properties of particles, which may be due to the proximity of roughness and thickness values to the 100 nm threshold for optical transparency. Samples on PMMA substrates performed modestly better than those on PC and glass in terms of wettability and optical transmittance. However, all samples exhibited a superhydrophobic CA ($> 150^\circ$), low CAH ($< 10^\circ$), and high transmittance of visible light ($> 90\%$ in most cases). In addition, all surfaces showed wear resistance for potential commercial use in AFM wear and water jet experiments, indicating strong bonding of the silicone resin and sufficient hardness of nanoparticles and resin.

This study indicates that transparent superhydrophobic surfaces with wear resistance can be fabricated with a broad range of materials to expand potential engineering applications. However, primary particle size, roughness, and coating morphology appear

to be at least as important a factor in optical transparency as inherent optical properties of nanoparticles when coating thickness is on the order of 100 nm.

CHAPTER 5: Superhydrophobic Surfaces with High Optical Transmittance on PDMS Using Reactive Ion Etching

5.1 Introduction

Superhydrophobic surfaces, with apparent water contact angle (CA) greater than 150° along with low contact angle hysteresis (CAH) of less than 10° , can have unique characteristics such as self-cleaning, antifouling, and fluid drag reduction (Nosonovsky and Bhushan, 2008; Bhushan, 2011; Bhushan, 2016). As discussed in Chapter 4, many applications also require high optical transparency, such as screen coatings, self-cleaning windows, and solar panels. Additionally, it is typically desirable for surfaces to have a degree of mechanical wear resistance. For industrial use, these surfaces should be reasonably simple and inexpensive to fabricate.

In general, achieving ultra-repellency of liquids involves surface roughness on the micro- and/or nanoscale. On a nominally flat surface, the maximum CA attainable is about 120° even when surface energy is at its practical minimum (Nishino *et al.*, 1999). Lotus-inspired rough surfaces are used to achieve CA higher than 120° (Bhushan, 2011). The air pocket formation in the Cassie-Baxter wetting regime can lead to very low contact angle hysteresis due to the high liquid-air fraction of the interface beneath the droplet. Achieving a low CAH ($<10^\circ$) is important for self-cleaning and other qualities

relying on low adhesion of the droplet to the surface. Therefore, wetting in the Cassie-Baxter regime is often desirable in the design of ultra-repellent surfaces (Bhushan, 2016).

Polydimethylsiloxane (PDMS), which has high optical transmittance, is an important material for biomedical devices, stretchable electronic circuits, and flexible microwave antennas (McClain *et al.*, 2009, Gonzalez *et al.*, 2009; Cheng and Wu, 2010). While PDMS is intrinsically hydrophobic, the surface is often modified to be hydrophilic through oxygen plasma treatment or other means (Chang, 1994; Kim *et al.*, 2000; Bodas and Khan-Malek, 2007). This is useful for applications such as analysis of biological samples and chemical synthesis. However, PDMS that has been made superhydrophobic has potential for use in contact-free dosage nozzles (Tropmann *et al.*, 2012) and devices using passive valves as flow regulators (Avram *et al.*, 2007). Ghosh *et al.* (2009) created biomimetic replicas of the *Colocasia* leaf with PDMS which, following modification with SiO₂ nanoparticles and vapor deposition of a fluorosilane, achieved superhydrophobicity and high advancing CA (120°) for glyceryl trioleate (surface tension = 35 mN/m). Im *et al.* (2010) used an inverse-trapezoidal re-entrant microstructure on PDMS to achieve superhydrophobicity (CA = 153°) as well as high CA (135°) for methanol (surface tension = 23 mN/m) with optical transmittance of 77%. PDMS has also been made superhydrophobic through plasma etching (Tserepi *et al.*, 2006; Manca *et al.*, 2008; Hwang *et al.*, 2009; Tropmann *et al.*, 2012). Tserepi *et al.* (2006) also reported optical transparency for some treatment times. However, an examination of the effects of roughness on superhydrophobicity and optical transmittance for plasma-etched PDMS, as well as an examination of wear resistance, has not been rigorously performed.

The motivation of this work was to create surfaces that simultaneously exhibit Lotus Effect benefits (superhydrophobicity with low CAH leading to self-cleaning ability) and high optical transmittance on PDMS, which is an important and widely used material in biomedical devices, microfluidics, and optical devices. The objectives of this work were to optimize a reactive ion etching (RIE) process with polydimethylsiloxane (PDMS) substrates using an O_2/CF_4 gas mixture, and to examine the effects of subsequent surface modifications on wettability and optical transmittance of samples. RIE is an extremely anisotropic process, making it useful for creating high aspect ratio surface roughness with appropriate process gases. In general, RIE combines effects from both chemical and physical processes in order to etch. Free radicals react with the material chemically while accelerated ions bombard the surface causing physical removal of material (Bjørnsen *et al.*, 2010). Physical etching in RIE is highly anisotropic generally. In the case of PDMS, the faster etching of organic groups compared to inorganic groups has been suggested by Tserepi *et al.* (2006) as an additional source of anisotropy.

An O_2/CF_4 mixture is a particularly powerful etchant of polymers; when mixed, oxygen and tetrafluoromethane create the oxyfluoride ion (OF^-), which can cut the carbon-carbon bonds in the backbone of the polymer and remove the molecule. An additional benefit of using RIE to achieve superhydrophobicity is that the desired surface morphology is formed in the base material itself rather than by nanoparticle-binder coatings or similar methods which can lead to more complicated fabrication and durability issues. To reduce surface energy on the etched surfaces, samples then underwent a plasma treatment with octafluorocyclobutane (C_4F_8), or were modified by

perfluorooctyltrichlorosilane (PFOTCS) through vapor deposition following surface activation by O₂ plasma. A relatively short C₄F₈ plasma treatment can result in deposition of a thin fluoropolymer layer. Fluorosilanes such as PFOTCS can form covalently bonded layers on PDMS after surface activation by oxygen plasma. In general, fluorinated materials are desired for ultra-repellent surfaces due to the very low polarizability of fluorine, which leads to weak adhesive forces and low surface energy (Brown and Bhushan, 2016). The CA, CAH, and optical transmittance of the etched samples were examined in terms of the roughness created by etching as well as the additional surface modifications. Measured CA and CAH are compared to the values predicted by equation using roughness and other parameters. An atomic force microscope (AFM) was used to examine sliding wear resistance of samples.

5.2 Experimental Details

5.2.1 Materials

A sheet of PDMS (Sylgard 184, Dow Corning) with thickness of 5 mm was prepared by mixing the base and curing agent at 10:1 ratio by weight in a Thinky planetary mixer for 4 min at 2000 rpm for mixing step and 4 min at 2200 rpm for defoaming step. The mixed, uncured PDMS was then degassed in vacuum oven at 25 °C for 90 min. It was then allowed to partially cure for 24 h at room conditions followed by full curing in oven at 85 °C for 100 min. Oxygen (O₂), tetrafluoromethane (CF₄), and octafluorocyclobutane (C₄F₈) gases for use in plasma reactor were supplied by Praxair, Inc.

Trichloro(1H,1H,2H,2H-perfluorooctyl)silane 97% (PFOTCS) was obtained from Sigma-Aldrich.

5.2.2 Reactive ion etching of PDMS and fluorosilane vapor deposition

Reactive ion etching (RIE) of the PDMS was performed in an Oxford Instruments Plasmalab 80. An illustration of the plasma chamber is shown in **Fig. 41**. In a chamber configured for reactive ion etching, the bottom electrode (on which the sample is placed) receives the excitation signal with the top electrode grounded, whereas in a non-RIE plasma etch process the top electrode is excited and the bottom electrode (with sample) is grounded. This causes the ion acceleration to be directional toward the sample in the case of reactive ion etching as opposed to random bombardment in a general plasma etch configuration. The processes used to prepare samples in the cases of additional C₄F₈ plasma treatment and PFOTCS deposition are shown schematically in **Fig. 42**.

In the first step in both cases, the PDMS is etched for varying length of time using a mixture of O₂ (flow rate 25 sccm) and CF₄ (flow rate 75 sccm) as process gases. A flow ratio of about 1:3 O₂:CF₄ has been found to yield the highest etch rate with this mixture (Garra *et al.*, 2002). RF power level was 300 W and pressure was 30 mTorr. In the second step in **Fig. 42a**, a thin fluorocarbon layer is formed on the etched PDMS using C₄F₈ gas (flow rate 100 sccm) for 30 s at 250 W, 250 mTorr. In the second step in **Fig. 42b**, PFOTCS forms a covalently bonded fluorosilane layer on the surface. To achieve this, the O₂/CF₄ etched PDMS was first activated by O₂ plasma for 30 s at 100 W and 250 mTorr. This activation allows for Si atom of PFOTCS to bond to surface oxygen, leaving

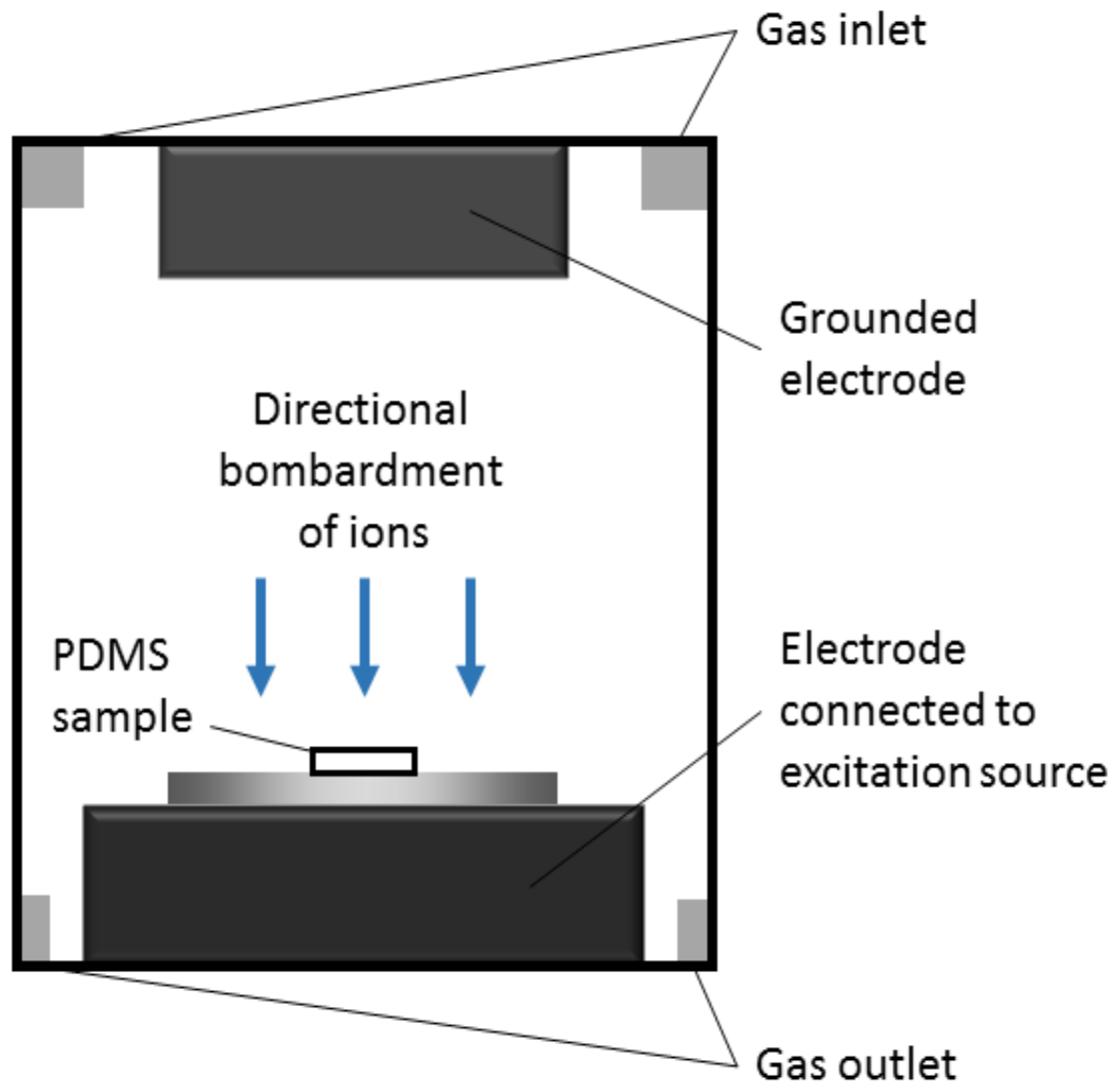


Figure 41: Illustration of plasma chamber configured for reactive ion etching of PDMS samples. The sample is placed on the electrode connected to the excitation source, with the other electrode grounded. This causes directional bombardment of ions toward the sample surface leading to higher etch rate with greater anisotropy.

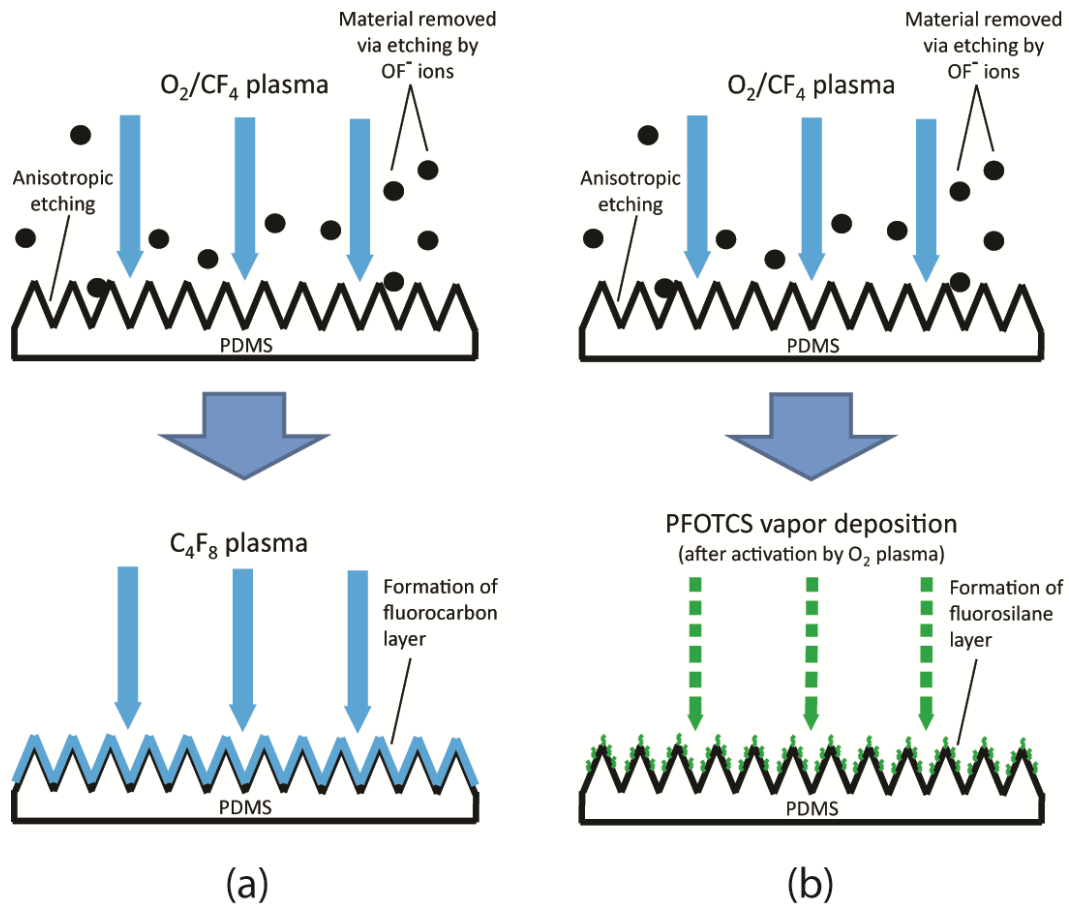


Figure 42: Schematic of (a) reactive ion etching of PDMS by O_2/CF_4 and subsequent C_4F_8 plasma treatment, and (b) reactive ion etching of PDMS by O_2/CF_4 and subsequent vapor deposition of perfluorooctyltrichlorosilane (PFOTCS). In both cases, the surface is first etched anisotropically by the oxyfluoride (OF^-) ions formed in the O_2/CF_4 mixture, resulting in a rough surface. In the case of C_4F_8 treatment (a), a thin fluorocarbon layer is then formed on the surface. In the case of PFOTCS modification (b), after surface activation by O_2 plasma, a covalently bonded fluorosilane layer is then formed with exposed long-chain hydrophobic tails (Ebert and Bhushan, 2016).

hydrophobic tail of the molecule exposed. Immediately after O₂ plasma treatment, deposited droplets spread quickly on samples and had CA < 10°, indicating effective surface activation for PFOTCS attachment. Vapor deposition was then performed by placing samples in a small covered petri dish with a few drops of PFOTCS for 2 h at room conditions.

The anisotropy of the RIE process can be maximized by increasing RF power and decreasing pressure. The lower pressure decreases the number of ions bombarding the surface, which decreases the uniformity of etching. The higher power causes ions to bombard the surface with greater energy, which helps to compensate for the decrease in ions in order to maintain sufficient etch rate. For this reason, high power level (300 W) and low pressure (30 mTorr) were used in this study for the etching of samples with the O₂/CF₄ mixture.

5.2.3 Characterization of etched PDMS samples

For wettability measurements, water droplets of 5 μL volume (~1 mm radius) were deposited onto samples using a microsyringe. CA and CAH were measured using a model 290-F4 Ramé-Hart goniometer (Ramé-Hart Inc., Succasunna, NJ). CAH was determined using the tilt method shown in **Fig. 4b**. Reproducibility of all CA and CAH data is reported as ($\pm\sigma$) as determined from measurement on five samples. Contact angle measurements taken immediately following O₂/CF₄ treatment were found to be inconsistent. However, after 24 h, contact angle values stabilized, suggesting some degree of surface reorganization following plasma treatment. For this reason, all

wettability measurements reported were taken at least 24 h after RIE treatment. Optical transmittance measurements were performed using an Ocean Optics USB400 spectrometer (Ocean Optics Inc., Dunedin, FL) with a 200 μm aperture width. All transmittance data is reported as a percentage of the transmittance of a virgin sample in the visible spectrum ($\lambda = 400\text{--}700$ nm). Scanning electron microscope (SEM) images were taken with a Zeiss Supra 55VP (EHT = 2.00 kV, aperture size = 30 μm).

Sliding wear resistance of samples was examined using an established AFM wear procedure (Bhushan, 2011; Jung and Bhushan, 2009; Ebert and Bhushan, 2012a) as described in section 2.3.3 with a commercial AFM (D3100, Nanoscope IIIa controller, Digital Instruments, Santa Barbara, CA). For wear experiments, investigation of single asperity contact is necessary to understand fundamental interfacial phenomena. An AFM tip can simulate single asperity contact for micro/nanostructured surfaces (Bhushan, 2011). Samples were worn using a borosilicate ball with radius 15 μm mounted on a rectangular Si(100) cantilever ($k = 7.4$ N/m) in contact mode. Areas of 50 x 50 μm^2 were worn for 1 cycle at loads of 1 μN and 10 μN . For Sylgard 184 PDMS at 10:1 mixing ratio cured at 85 $^{\circ}\text{C}$, compressive modulus is estimated to be 157 MPa (Johnston *et al.*, 2014). A Poisson's ratio of 0.5 is typically assumed for polymers (Mark, 1999). Elastic modulus of 70 GPa and Poisson's ratio of 0.2 were used for borosilicate glass (Callister and Rethwisch, 2013). Hertz analysis can be used to find the maximum pressure under the contact (Bhushan, 2013a). The reduced modulus of the tip, E_r , can be found using Eq. (11) (Bhushan, 2013a):

$$\frac{1}{E_r} = \frac{(1-\nu_t^2)}{E_t} + \frac{(1-\nu_s^2)}{E_s} \quad (11)$$

where ν_t , E_t and ν_s , E_s are the Poisson's ratio and elastic modulus of the tip and sample, respectively. After solving for the value E_r , the maximum pressure P_0 under the contact can be found using Eq. (12) (Bhushan, 2013a):

$$P_0 = \sqrt[3]{\frac{6PE_r^2}{\pi^3 R^2}} \quad (12)$$

where P is the applied load and R is the radius of the tip. Using Eqs. (11) and (12), the maximum pressure under the contact was calculated to be 3.3 MPa for load of 1 μN and 7.2 MPa for load of 10 μN . To analyze the change in the morphology of the surfaces before and after wear from borosilicate ball, height scans of 100 x 100 μm^2 in area were obtained using a rectangular Si(100) tip ($f = 76$ kHz, $k = 3$ N/m) in tapping mode.

The values of RMS roughness, PV distance, and R_f were calculated using AFM surface height maps obtained with a Si, N-type (Si_3N_4) tip with Al coating ($f = 66$ kHz, $k = 3$ N/m) with scan area 10 x 10 μm^2 . In the case of R_f , the real surface area can be approximated using the height of each data point in the AFM scan matrix as described in section 3.3.1 and shown in **Fig. 29**. The roughness factor R_f is then found by dividing real surface area by the two-dimensional scan area. The values of f_{LA} were estimated using AFM maps with SPIP™ imaging software (Image Metrology) with the assumption that the droplet contacts only the highest peaks of surface asperities in a stable Cassie-Baxter regime. Based on this assumption, threshold height criteria can be selected for image processing. The criteria are applied consistently across all samples to determine estimated

f_{LA} values so that the differences between measured and calculated CA and CAH for different surface treatments can be compared.

5.3 Results and discussion for etched PDMS samples

The etched PDMS samples both with and without additional surface treatment are discussed below. First, measured roughness values and surface morphology are presented. Then, the CA, CAH, and optical transmittance of samples are reported with discussion of trends in the data. A comparison of measured CA and CAH values to values predicted by equation is then performed based on roughness and other parameters. Lastly, the results of the AFM wear test are examined.

5.3.1 Surface roughness and morphology

Table 10 displays RMS roughness, PV (peak-valley) distance, roughness factor (R_f), and estimated liquid-air fraction of interface (f_{LA}) for samples with varying etch time under RIE with O_2/CF_4 plasma only, samples etched by O_2/CF_4 with subsequent C_4F_8 plasma treatment, and samples etched by O_2/CF_4 with subsequent PFOTCS vapor deposition. The roughness factor R_f is defined as the ratio of the real area of the interface to its two-dimensional projection.

The etched surfaces had high aspect ratio nanoscale roughness because of the highly anisotropic nature of RIE. The RMS roughness and PV distance increased with etch time, reaching RMS = 302 nm and PV = 567 nm at 25 min. The roughness of samples after the additional C_4F_8 plasma treatment, which forms a very thin fluorocarbon layer on the

Table 10: Measured roughness values (RMS, PV, and R_f) and estimated liquid-air fractional area (f_{LA}) for samples etched by O_2/CF_4 plasma only, samples etched by O_2/CF_4 with subsequent C_4F_8 plasma treatment, and samples etched by O_2/CF_4 with subsequent perfluorooctyltrichlorosilane (PFOTCS) vapor deposition (Ebert and Bhushan, 2016)

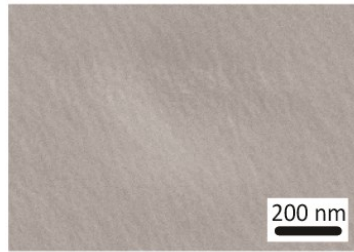
O_2/CF_4 etch time (min)	RMS (nm)	PV (nm)	R_f	f_{LA}
Samples etched by O_2/CF_4 plasma				
0	~0	~0	1	0
5	29	78	1.3	0.84
10	75	186	2.4	0.90
15	126	292	2.9	0.93
20	207	431	3.1	0.95
25	302	567	3.2	0.95
Samples etched by O_2/CF_4 plasma with subsequent C_4F_8 plasma treatment				
0	~0	~0	1	0
5	27	75	1.3	0.82
10	72	181	2.3	0.87
15	120	282	2.7	0.91
20	199	419	3.0	0.93
25	295	556	3.1	0.94
Samples etched by O_2/CF_4 plasma with subsequent PFOTCS vapor deposition				
0	~0	~0	1	0
5	29	78	1.3	0.84
10	75	186	2.4	0.90
15	126	292	2.9	0.93
20	207	431	3.1	0.95
25	302	567	3.2	0.95

rough surface, decreased slightly for all samples, reaching RMS = 295 nm and PV = 556 nm for samples etched 25 min by O₂/CF₄. The thickness of the fluorocarbon layer was measured to be approximately 25 nm using AFM with a simple step method. While the thickness was virtually uniform on a flat PDMS sample, the fluorocarbon formed on rough etched samples may be more prone to fill in gaps between asperities, decreasing measured roughness. A similar effect was noted by Zanini *et al.* (2014) when treating roughened PET surfaces with hexamethyldisiloxane (HMDSO) plasma. In the case of the PFOTCS vapor deposition, which forms a covalently bonded fluorosilane layer, roughness was unchanged. **Figure 43** shows SEM micrograph of unetched PDMS sample at high magnification, as well as samples after 10 min and 20 min etch time at three magnifications. Roughness features are noticeably larger after 20 min compared to 10 min, with increased space between peaks. This nanoscale roughness is important for superhydrophobicity and low CAH, but at a value too high can be expected to impede optical transmittance of light.

5.3.2 Wettability and optical transmittance

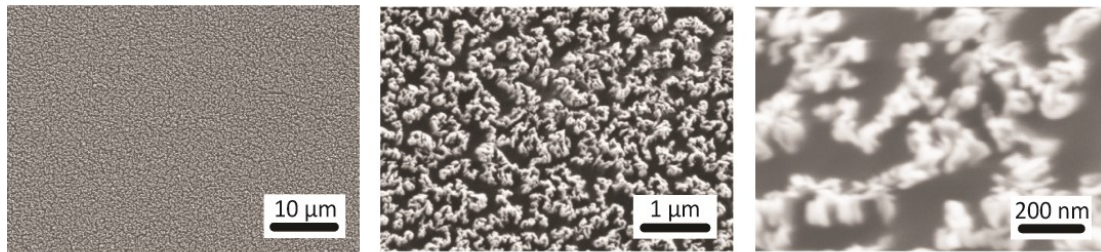
Figure 44 shows measured CA and CAH data for samples etched by O₂/CF₄ plasma only, by O₂/CF₄ with subsequent C₄F₈ plasma treatment, and by O₂/CF₄ with subsequent O₂ plasma surface activation and PFOTCS vapor deposition. The CA on flat, virgin PDMS was measured to be 108°. Etched samples became superhydrophobic for RMS roughness 75 nm and greater (corresponding to etch times 10, 15, 20, and 25 min),

Unetched PDMS sample

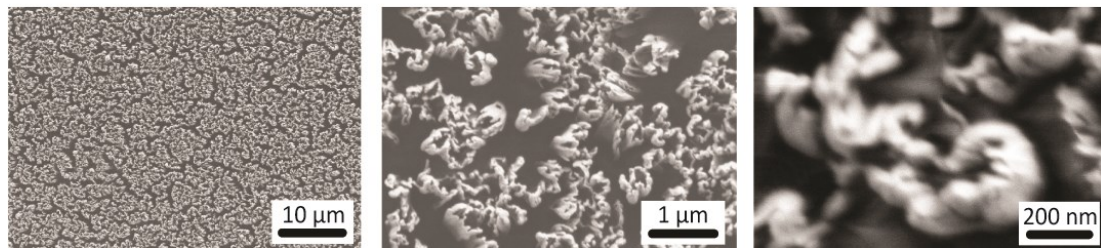


(a)

PDMS sample etched by O_2/CF_4 (10 min etch time)



PDMS sample etched by O_2/CF_4 (20 min etch time)



(b)

Figure 43: SEM micrographs of (a) unetched, virgin PDMS sample at high magnification and (b) PDMS samples at three magnifications after 10 min and after 20 min etch time by O_2/CF_4 plasma (Ebert and Bhushan, 2016)

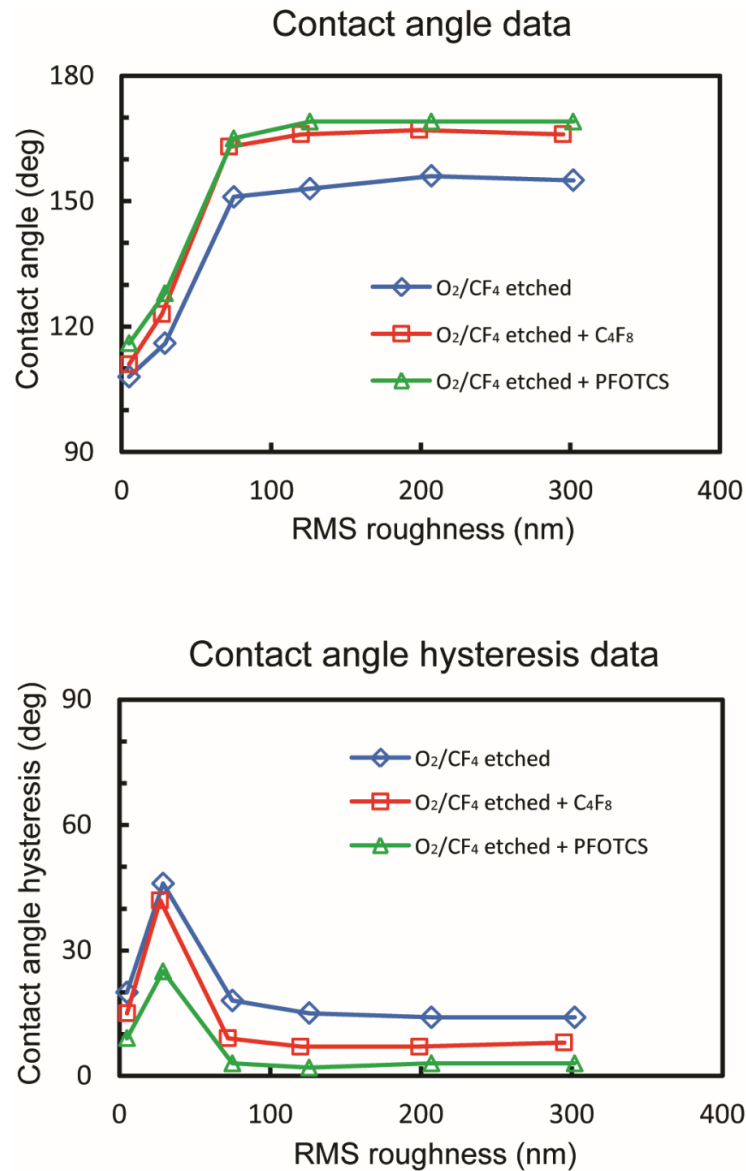


Figure 44: Contact angle and contact angle hysteresis data on PDMS samples of varying RMS roughness values for samples etched by O₂/CF₄ plasma only, by O₂/CF₄ with subsequent C₄F₈ plasma treatment, and by O₂/CF₄ with subsequent perfluorooctyltrichlorosilane (PFOTCS) vapor deposition. Reproducibility is $\pm 1^\circ$ for CA data and $\pm 2^\circ$ for CAH data. Lines between data points are intended only to guide the eyes and not for interpolation (Ebert and Bhushan, 2016).

achieving apparent CA in the range 151–156°. CAH for etched samples with RMS = 29 nm increased to 46° compared to 20° for unetched PDMS. For RMS values 75 nm and greater, CAH was reduced significantly to the range 14–18°.

The CA on unetched PDMS after C₄F₈ treatment was measured to be 111°. Samples remained superhydrophobic for RMS roughness 72 nm and greater, reaching higher apparent CA in the range 163–167°. CAH was lower for the superhydrophobic samples compared to before C₄F₈ treatment, achieving values in the range 7–9°. The thin fluorocarbon layer from C₄F₈ plasma increased CA for superhydrophobic samples by 11–13° compared to before treatment, and decreased CAH by 6–9°. The reduction in CAH is perhaps a more significant benefit, as CAH less than 10° is often desired for many applications involving superhydrophobicity. The CA on unetched PDMS after PFOTCS modification by vapor deposition was measured to be 116°. Samples with roughness of 75 nm and greater achieved CA of 165–169° and CAH as low as 2°. While the increase in CA with PFOTCS compared to C₄F₈ plasma is fairly modest, the further reduction in CAH to nearly zero is potentially beneficial.

Figure 45 displays the average optical transmittance across the visible range of samples plotted against RMS roughness. Transmittance is expressed as a percentage of the transmittance of a virgin PDMS sample. Etched samples remained highly transparent (>85%) up to RMS roughness value of 126 nm (achieved after 15 min etch time). For RMS roughness 207 nm and 302 nm, achieved after 20 and 25 min etch times, respectively, samples became nearly or entirely opaque. This is likely due to the

Transmittance of O₂/CF₄ etched PDMS samples

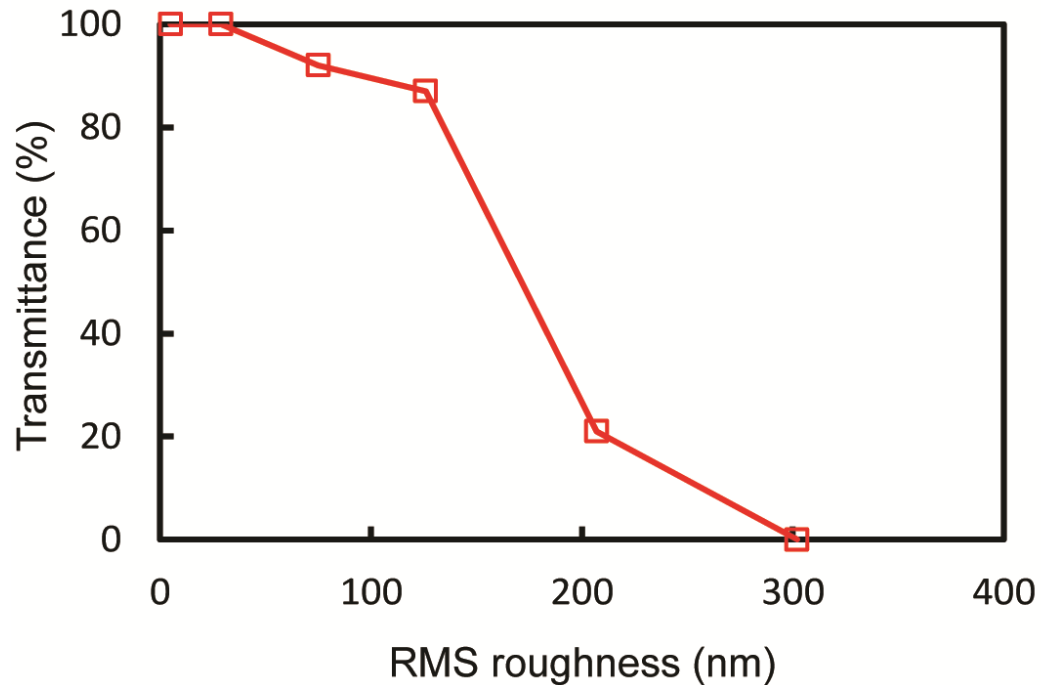


Figure 45: Optical transmittance of O₂/CF₄ etched PDMS samples of varying RMS

roughness values. Data represent the percentage of the baseline transmittance of a PDMS substrate, and is taken as the average across the visible range ($\lambda = 400\text{--}700$ nm). Lines between data points are intended only to guide the eyes and not for interpolation (Ebert and Bhushan, 2016).

roughness values significantly exceeding one quarter the wavelength of visible light (around 100 nm for shortest wavelengths). Measured optical transmittance values were identical for a given etch time before and after 30-second treatment with C₄F₈ plasma or PFOTCS functionalization.

Samples were superhydrophobic and highly transparent after etch times of 10 and 15 min both before and after surface modification with either C₄F₈ plasma treatment or PFOTCS deposition. This agrees with previous findings that superhydrophobicity and optical transparency can be simultaneously achieved with roughness in the vicinity of 100 nm (Ling *et al.*, 2009; He *et al.*, 2011; Ebert and Bhushan, 2012c). An etched PDMS sample with RMS roughness 126 nm (etch time 15 min with C₄F₈ post-treatment) can be seen in **Fig. 46** with deposited water droplet showing superhydrophobicity and high optical transmittance of light. Also displayed is a goniometer image of droplet on sample showing superhydrophobic contact angle.

5.3.3 Comparison of measured CA and CAH to predicted values

The apparent CA of a droplet on a surface is ultimately the result of conditions at the solid-liquid-air triple line that forms the perimeter of the wetting interface. For a surface with non-uniform roughness, the local CA at the triple line must be found as a function of spatial variables in order to determine the apparent macroscale CA. However, if roughness can be considered uniform and roughness features are small compared to the length of the triple line, then CA can be predicted using Eq. (3) (Bhushan, 2016), given in section 1.2. In the case of a Wenzel wetting regime, in which the liquid fully penetrates between roughness features and leaves no air gaps, the liquid-air fraction f_{LA} can be assumed to be zero. In the case of a highly stable Cassie-Baxter wetting regime, in which virtually no penetration occurs and the droplet sits flat across the composite interface, the

Table 11: Summary of measured and calculated contact angle (CA) and measured contact angle hysteresis (CAH) for samples etched by O₂/CF₄ plasma only, samples etched by O₂/CF₄ with subsequent C₄F₈ plasma treatment, and samples etched by O₂/CF₄ with subsequent perfluorooctyltrichlorosilane (PFOTCS) vapor deposition. ($f_{LA} = 0$ assuming Wenzel state, $R_f \sim 1$ assuming Cassie-Baxter state) (Ebert and Bhushan, 2016)

O ₂ /CF ₄ etch time (min)	CA measured (deg) ($\pm 1^\circ$)	CA calculated by Eq. (3) assuming Wenzel state (deg)	CA calculated by Eq. (3) assuming Cassie-Baxter state (deg)	CAH measured (deg) ($\pm 2^\circ$)
Samples etched by O ₂ /CF ₄ plasma				
0	108	108	108	20
5	116	114	153	46
10	151	138	159	18
15	153	154	162	15
20	156	163	165	14
25	155	171	165	14
Samples etched by O ₂ /CF ₄ plasma with subsequent C ₄ F ₈ plasma treatment				
0	111	111	111	15
5	123	118	152	42
10	163	146	156	9
15	166	165	160	7
20	167	~180	163	7
25	166	~180	164	8
Samples etched by O ₂ /CF ₄ plasma with subsequent PFOTCS vapor deposition				
0	116	116	116	9
5	128	125	156	25
10	165	~180	161	3
15	169	~180	164	2
20	169	~180	166	2
25	169	~180	166	3

based on CA alone. However, the low measured CAH for these samples strongly indicates Cassie-Baxter regime since a composite interface tends to result in very low adhesion and CAH. For samples with etch times 20 and 25 min with C₄F₈ treatment and with 10, 15, 20, and 25 min with PFOTCS treatment, the high flat surface CA (θ_0) and R_f values are such that Eq. (3) cannot be resolved in the Wenzel regime (values shown as $\sim 180^\circ$). The CA values predicted by the assumption of a Cassie-Baxter regime, however, are comparable to the measured values. Cassie-Baxter regime is further evidenced by the very low CAH values. For samples both with and without subsequent surface modification, the comparison to predicted values suggests Wenzel regime after 0 and 5 min etch time and Cassie-Baxter regime for 10, 15, 20, and 25 min etch time.

Contact angle hysteresis is governed by many microscale and nanoscale phenomena. Even for a uniformly rough surface, the CAH cannot be calculated from macroscale wettability equations. However, CAH can be estimated by Eq. (10), given in section 4.3.2. **Table 12** summarizes the measured CAH of samples as well as the CAH estimated using Eq. (10). Values are shown for samples etched by O₂/CF₄ plasma only, by O₂/CF₄ with subsequent C₄F₈ plasma treatment, and by O₂/CF₄ with subsequent PFOTCS vapor deposition.

For samples with etch times of 0 and 5 min, Wenzel regime wetting is assumed and $f_{LA} = 0$. For samples with etch times of 10, 15, 20, and 25 min, Cassie-Baxter wetting is assumed, and R_f is taken as 1.0. The measured values of θ_{rec0} and θ_{adv0} on flat PDMS were 91° and 111° , respectively. For samples etched by O₂/CF₄ plasma only, measured CAH

Table 12: Summary of measured and calculated contact angle hysteresis (CAH) for samples etched by O₂/CF₄ plasma only, samples etched by O₂/CF₄ with subsequent C₄F₈ plasma treatment, and samples etched by O₂/CF₄ with subsequent perfluorooctyltrichlorosilane (PFOTCS) vapor deposition. Based on CA analysis in Table 11, Wenzel state assumed ($f_{LA} = 0$) for samples with 0 and 5 min etch times and Cassie-Baxter state assumed ($R_f \sim 1$) for samples with 10, 15, 20, 25 min etch times (Ebert and Bhushan, 2016).

O ₂ /CF ₄ etch time (min)	R_f	f_{LA}	CAH measured (deg) ($\pm 2^\circ$)	CAH calculated using Eq. (10) (deg)
Samples etched by O ₂ /CF ₄ plasma				
0	1.0	0 ^a	20	17
5	1.3	0 ^a	46	23
10	1.0 ^b	0.90	18	5
15	1.0 ^b	0.93	15	4
20	1.0 ^b	0.95	14	4
25	1.0 ^b	0.95	14	4
Samples etched by O ₂ /CF ₄ plasma with subsequent C ₄ F ₈ plasma treatment				
0	1.0	0 ^a	15	13
5	1.3	0 ^a	42	18
10	1.0 ^b	0.87	9	5
15	1.0 ^b	0.91	7	4
20	1.0 ^b	0.93	7	3
25	1.0 ^b	0.94	8	3
Samples etched by O ₂ /CF ₄ plasma with subsequent PFOTCS vapor deposition				
0	1.0	0 ^a	9	8
5	1.3	0 ^a	25	12
10	1.0 ^b	0.90	3	3
15	1.0 ^b	0.93	2	2
20	1.0 ^b	0.95	2	2
25	1.0 ^b	0.95	3	2

^a Assumes Wenzel state ($f_{LA} = 0$)

^b Assumes Cassie-Baxter state ($R_f \sim 1$)

values were significantly higher than values calculated by Eq. (10), including the superhydrophobic samples (etch time 10, 15, 20, 25 min), for which the measured values exceeded estimated values by 10° – 13° . For samples with C_4F_8 treatment ($\theta_{rec0} = 98^{\circ}$, $\theta_{adv0} = 113^{\circ}$), the measured CAH values for superhydrophobic samples exceeded the estimated values by 4° – 5° . For samples with PFOTCS vapor deposition ($\theta_{rec0} = 109^{\circ}$, $\theta_{adv0} = 118^{\circ}$), CAH for superhydrophobic samples was well predicted by Eq. (10), and exhibited the lowest values of 2° – 3° . Since Eq. (10) accounts for the change in flat surface wettability parameters (θ_0 , θ_{rec0} , and θ_{adv0}) due to C_4F_8 treatment, the narrowing of the gap between measured and predicted CAH compared to without treatment may suggest that both the thin fluorocarbon layer and fluorosilane treatment increase f_{LA} for these samples.

In the case of samples etched by O_2/CF_4 but without additional treatment, the assumption made in estimating f_{LA} that the droplet only contacts the peaks of surface asperities may result in underestimation of CAH when calculating from Eq. (10). Thus, the reduction of surface energy by the surface treatments may reduce CAH not only by increasing θ_0 but by decreasing the solid-liquid contact in the composite interface, as the droplet is more likely to rest only on peaks of asperities. In the case of PFOTCS vapor deposition, the lowest CAH values are likely due to the exposed long-chain hydrophobic tails of molecules on the fluorosilane-modified surface.

5.3.4 Wear resistance in AFM sliding wear experiment

The results of the AFM sliding wear experiment are shown in **Fig. 47**. Surface height maps are displayed for before and after wear for samples etched by O₂/CF₄ with C₄F₈ treatment. Roughness values within the wear area (RMS and PV) are given for both before and after wear, as well as sample scans across the middle of the image (position indicated by arrow). Wear data for flat PDMS is difficult to obtain due to the compliance of the material. For etched PDMS, after cycle at load of 1 μN with borosilicate ball, very little wear is evident from surface height map and roughness did not change significantly. After cycle at load of 10 μN, significant wear can be seen as material was pushed in the sliding direction of the borosilicate ball. Wear rate is generally inversely related to hardness and rigidity (Bhushan, 2013a). For PDMS with 10:1 mixing ratio and cured at 85 °C, hardness is relatively low at about 46 (Shore A) or on the order of 400 MPa (Kim *et al.*, 2013; Johnston *et al.*, 2014). It is evident that while the high aspect ratio features formed on the PDMS through RIE have some resistance to wear at lower load (on the order of 1 μN), they appear to be susceptible to wear at higher loads.

5.4 Conclusions

In this study, superhydrophobic surfaces with high optical transmittance were created on PDMS with a simple process using reactive ion etching and subsequent surface modification. The results demonstrated a range of surface roughness values that were high enough to result in superhydrophobicity but low enough to preserve high transmittance of visible light. A degree of mechanical wear resistance was seen at lower

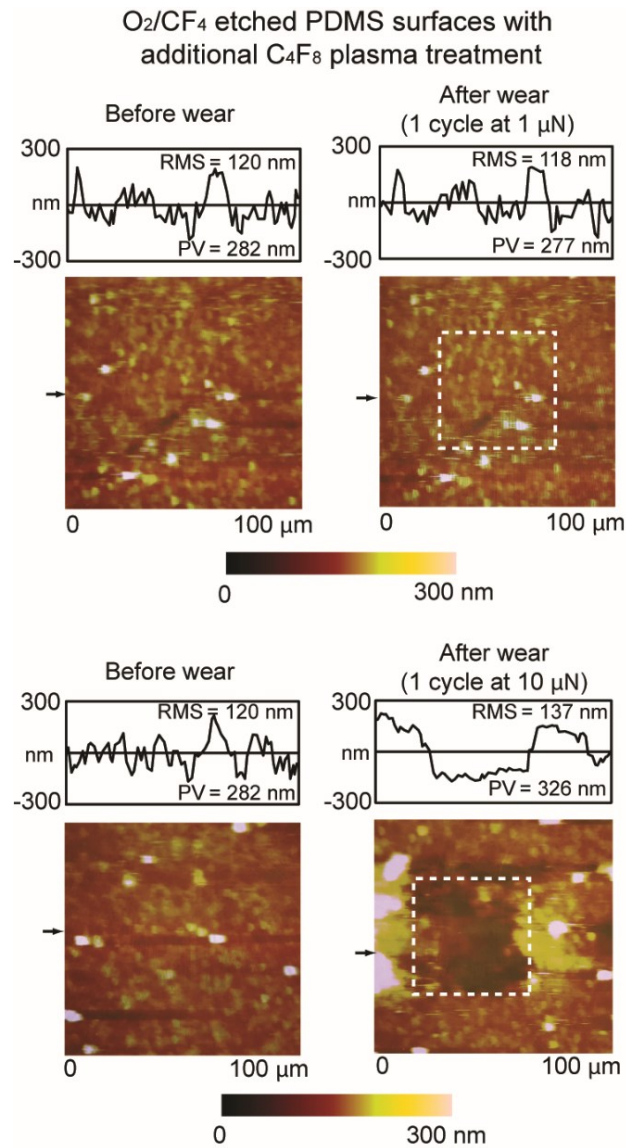


Figure 47: Surface height maps and sample surface profiles (locations indicated by arrows) for before and after AFM wear experiment using 15- μm radius borosilicate ball at loads of 1 μN and 10 μN for PDMS samples etched by O_2/CF_4 for 15 min with subsequent C_4F_8 plasma treatment. RMS roughness and PV distance values for surface profiles are displayed within surface profile boxes (Ebert and Bhushan, 2016).

load, but significant wear was evident at higher load on the rough, etched surfaces of PDMS. Superhydrophobicity was achieved for etched samples both with and without the additional C_4F_8 plasma treatment or perfluorooctyltrichlorosilane (PFOTCS) modification. The fluorocarbon layer from C_4F_8 treatment increased CA, but perhaps more importantly decreased CAH to below 10° for the samples that had CA in the superhydrophobic range ($>150^\circ$). Surfaces modified by PFOTCS showed a modest increase in CA compared to those with C_4F_8 treatment, but also showed a reduction in CAH to as low as 2° . An examination of predicted and measured CA and CAH values suggests the surface modifications, in addition to lowering surface energy, may increase the liquid-air fraction (f_{LA}) for a given surface morphology and correspondingly reduce CAH. For samples modified by vapor deposition of PFOTCS, the very low CAH is also likely due to the exposed long-chain hydrophobic tails of molecules at the surface.

CHAPTER 6: Summary and Future Work

Wettability of surfaces is an important design parameter for many technologies. Extreme wettability states such as superhydrophobicity are of particular interest as they can provide unique benefits. Evolution has produced many surfaces in nature that possess extreme wettability characteristics (as examples, superhydrophobicity and superhydrophilicity) for various survival advantages, often by means of micro- and/or nanoscale topology. The motivation of this work was to use lessons from nature to design and fabricate surfaces that achieve the benefits of these effects (for example, self-cleaning) for engineering applications. The broad objectives of the work were to study the effects of micro- and nanoscale geometry and roughness parameters and surface chemistry with regard to wettability and optical transmittance, and to determine materials and fabrication techniques that result in mechanically durable surfaces.

Hierarchically structured surfaces (i.e., surfaces having multiscale roughness) with Lotus Effect characteristics were fabricated using micro- and nanosized silica (SiO_2) particles and a simple spray process. In addition, a comparison was made between the use of microparticles and micropatterns in terms of wettability across different pitch values. Results showed similar trends in CA and CAH the with pitch value whether the microstructure was formed with particles or a micropattern. The regime transition from

Cassie-Baxter to Wenzel was observed to occur at a lower average pitch value in the case of microparticles compared to uniform micropatterned surfaces.

Hierarchically structured surfaces using micro- and nanoparticles exhibited very high CA of $166^\circ (\pm 2^\circ)$ and very low CAH of $2^\circ (\pm 1^\circ)$ at optimum pitch. For hierarchically structured surfaces using micropatterns with nanoparticles, a nearly identical CA of $168^\circ (\pm 2^\circ)$ and CAH of $1^\circ (\pm 0.5^\circ)$ were measured. In both cases, the requirements of superhydrophobicity ($CA > 150^\circ$) and self-cleaning ($CAH < 10^\circ$) were easily met. In addition, the surfaces demonstrated wear resistance superior to the epoxy resin on multiple length scales in the AFM and tribometer experiments, showing ability to preserve both nanoscale and microscale roughness. Preservation of superhydrophobicity under exposure to impacting water was demonstrated in water jet experiments.

Surfaces exhibiting the Rose Petal Effect (superhydrophobicity with high droplet adhesion) were created using both hydrophilic and hydrophobic zinc oxide (ZnO) nanoparticles on microstructured and flat substrates. The impregnating wetting regime is responsible for this wetting behavior, in which liquid penetrates between microstructures but is only partially able to penetrate between nanostructures. In addition, the surfaces showed wear resistance for potential commercial use in an AFM wear experiment, indicating strong bonding of the epoxy resin and sufficient hardness of ZnO nanoparticles and resin.

With hydrophilic nanoparticles, the Rose Petal Effect could be achieved with high nanoparticle spray concentration (3000 mg/L) on a flat substrate. Droplets on this surface had a CA of 151° , CAH of 71° , and remained adhered when the surface was inverted.

The high nanoparticle concentration created high surface roughness, which is necessary to obtain a superhydrophobic state using hydrophilic materials. However, the high roughness precluded the use of a microstructure with the geometry and the range of pitch values used in this study, as the roughness resulted in a predominantly Cassie-Baxter state on the microstructure with low droplet adhesion.

With hydrophobic nanoparticles, the Rose Petal Effect was achieved with significantly lower nanoparticle spray concentration (1000 mg/L) on a microstructure with 105 μm pitch. Droplets on this surface had a CA of 154° , CAH of 69° , and could likewise remain adhered to an inverted substrate. Increasing nanoparticle concentration or decreasing microstructure pitch resulted in a Cassie-Baxter state with low adhesion. Conversely, decreasing nanoparticle concentration or increasing microstructure pitch resulted in a loss of superhydrophobicity. This is in agreement with results of previous studies using a hydrophobic nanostructure for high adhesion surfaces.

Therefore, it was demonstrated that wear-resistant surfaces with the Rose Petal Effect can be fabricated with either hydrophilic or hydrophobic materials by creating appropriate micro- and nanoscale surface structures. However, the surface energy of material forming the nanostructure greatly affects the required nanostructure density, microstructure pitch value, and roughness necessary to achieve superhydrophobicity with high adhesion. Use of a hydrophobic nanostructure may be preferable considering that a lower surface roughness is required.

A versatile dip coating technique was used in a systematic study to create superhydrophobic surfaces with high optical transmittance on glass and plastic substrates

with silica (SiO₂), zinc oxide (ZnO), and indium tin oxide (ITO) nanoparticles. ZnO and ITO particles were hydrophobized with ODP, and the prepared samples did not require post-treatment with low surface energy substances. The nanoparticles showed different tendencies in the way they deposited onto substrates from dip coating, which may be partly due to differences in primary particle size. This caused variation in coating thickness and morphology between particles, which helps to explain differences in wettability and optical transmittance between samples.

ITO samples had slightly lower CA and slightly higher CAH than SiO₂, ZnO, which is likely the result of a comparatively lower liquid-air fractional area (f_{LA}). Roughness and coating thickness seemed to influence optical transmittance more than inherent optical properties of particles, which may be due to the proximity of roughness and thickness values to the 100 nm threshold for optical transparency. Samples on PMMA substrates performed modestly better than those on PC and glass in terms of wettability and optical transmittance. However, all samples exhibited a superhydrophobic CA (> 150°), low CAH (< 10°), and high transmittance of visible light (> 90% in most cases). In addition, all surfaces showed wear resistance for potential commercial use in AFM wear and water jet experiments, indicating strong bonding of the silicone resin and sufficient hardness of nanoparticles and resin.

This indicates that transparent superhydrophobic surfaces with wear resistance can be fabricated with a broad range of materials to expand potential engineering applications. However, primary particle size, roughness, and coating morphology appear to be at least as important a factor in optical transparency as inherent optical properties of

nanoparticles when coating thickness is on the order of 100 nm. This is an important design consideration in the development of self-cleaning windows and windshields.

Superhydrophobic surfaces with high optical transmittance were also created on PDMS substrates with a simple process using reactive ion etching and subsequent surface modification intended to reduce surface energy. PDMS is an important material for many biomedical and microfluidic devices where wettability and fluid drag can be critical design parameters, and thus superhydrophobic PDMS surfaces are of interest. An advantage of using reactive ion etching to create surface roughness is that the surface roughness is formed in the bulk material itself rather than through a nanoparticle-binder matrix, which may be more desirable or easier to fabricate in some cases.

The results demonstrated a range of surface roughness values that were high enough to result in superhydrophobicity but low enough to preserve high transmittance of visible light. A degree of mechanical wear resistance was seen at lower load, but significant wear was evident at higher load on the rough, etched surfaces of PDMS. Superhydrophobicity was achieved for etched samples both with and without a subsequent surface modification by either C_4F_8 plasma or vapor deposition of perfluorooctyltrichlorosilane (PFOTCS). The fluorocarbon layer from C_4F_8 treatment increased CA, but perhaps more importantly decreased CAH to below 10° for the samples that had CA in the superhydrophobic range ($>150^\circ$). Surfaces modified by PFOTCS showed a modest increase in CA compared to those with C_4F_8 treatment, but also showed a reduction in CAH to as low as 2° . An examination of predicted and measured CA and CAH values suggests the surface modifications, in addition to lowering surface energy, may increase

the liquid-air fraction (f_{LA}) for a given surface morphology and correspondingly reduce CAH. For samples modified by vapor deposition of PFOTCS, the very low CAH is also likely due to the exposed long-chain hydrophobic tails of molecules at the surface. This work indicates that superhydrophobic PDMS with high optical transmittance can be fabricated using a fairly simple reactive ion etching technique to create nanoscale roughness in the PDMS itself, and that further improvements in the Lotus Effect characteristics (higher CA and lower CAH) can be achieved through subsequent modifications to reduce surface energy.

More investigation is required in the design of surfaces that can repel not only water but liquids with lower surface energy, such as oils. Because the flat-surface contact angles for these liquids tend to be very low, oil-repellent (or “oleophobic”) surfaces often require roughness features with re-entrant geometry, which are not only difficult to fabricate but are prone to stress concentrations and breakage. The issue of durability in general remains a challenge, as rough surfaces (which are needed for superhydrophobicity) typically contain high-aspect-ratio features which are inherently prone to failure and wear. There is more work to be done in the area of icephobic surfaces, as de-icing is an expensive and widespread problem. Icephobicity has been found to relate very closely to low contact angle hysteresis, which results in weak adhesion of ice or the prevention of ice formation. However, the extent of the overlap between designing superhydrophobic and icephobic surfaces is not entirely clear.

This work provides valuable data and insights for future research in the design and fabrication of superhydrophobic surfaces, especially regarding micro- and nanoscale

surface geometry, roughness, surface treatments, materials, multiscale mechanical durability, and fabrication techniques. With the continued rise of nanotechnology, interest in superhydrophobicity and extreme wettability in general can only be expected to increase.

BIBLIOGRAPHY

- Avram, M., Avram, M.A., Bragaru, A., Ghiu, A., and Iliescu, C. (2007), "Plasma Surface Modification of Polymer Substrates for Selective Hydrophobic Control," presented at 2007 International Semiconductor Conference, Sinaia, Romania, 2007. IEEE
- Barthlott, W. and Neinhuis, C. (1997), "Purity of the sacred lotus, or escape from contamination in biological surfaces," *Planta* **202**, 1-8
- Bhushan, B. (1999), *Handbook of Micro/Nanotribology*, 2nd ed., Boca Raton, FL: CRC Press
- Bhushan, B. (2010), *Springer Handbook of Nanotechnology*, 3rd ed., Springer-Verlag, Heidelberg, Germany
- Bhushan, B. (2011), *Nanotribology and Nanomechanics I – Measurement Techniques, II – Nanotribology, Biomimetics, and Industrial Applications* 3rd ed., Springer-Verlag, Heidelberg, Germany
- Bhushan, B. (2013a), *Introduction to Tribology*, 2nd ed., Wiley, New York
- Bhushan, B. (2013b), *Principles and Applications of Tribology*, 2nd ed., Wiley, New York
- Bhushan, B. (2016), *Biomimetics: Bioinspired Hierarchical-Structured Surfaces for Green Science and Technology*, 2nd ed.; Springer International
- Bhushan, B. and Her, E. K. (2010), "Fabrication of Superhydrophobic Surfaces with High and Low Adhesion Inspired from Rose Petal," *Langmuir* **26**, 8207-8217
- Bhushan, B. and Jung, Y. C. (2007), "Wetting study of patterned surfaces for superhydrophobicity," *Ultramicroscopy* **107**, 1033-1041
- Bhushan, B. and Jung, Y. C. (2008), "Wetting, Adhesion and Friction of Superhydrophobic and Hydrophilic Leaves and Fabricated Micro/nanopatterned Surfaces," *J. Phys.: Condens. Matter* **20**, 225010

- Bhushan, B., Jung, Y. C., and Koch, K. (2009), "Micro-, Nano- and Hierarchical Structures for Superhydrophobicity, Self-Cleaning and Low Adhesion," *Phil. Trans. R. Soc. A* **367**, 1631-1672
- Bjørnsen, G., Henriksen, L., Ulvensøen, J.H., and Roots, J. (2010), "Plasma etching of different polydimethylsiloxane elastomers, effects from process parameters and elastomer composition," *Microelectron. Eng.* **87**, 67-71
- Bodas, D. and Khan-Malek, C. (2007), "Hydrophilization and hydrophobic recovery of PDMS by oxygen plasma and chemical treatment – An SEM investigation," *Sensors and Actuators B* **123**, 368-373
- Bormashenko, E., Stein, T., Pogreb, R., and Aurbach, D. (2009), "'Petal Effect' on Surfaces Based on Lycopodium: High-Stick Surfaces Demonstrating High Apparent Contact Angles," *J. Phys. Chem. C* **113**, 5568-5572
- Bormashenko, E. (2011), "General equation describing wetting of rough surfaces," *J. Colloid and Interf. Sci.* **360**, 317-319
- Bravo, J., Zhai, L., Wu, Z., Cohen, R.E., and Rubner, M.F. (2007), "Transparent Superhydrophobic Films Based on Silica Nanoparticles," *Langmuir* **23**, 7293-7298
- Brown, P. and Bhushan, B. (2015), "Mechanically durable, superoleophobic coatings prepared by layer-by-layer technique for anti-smudge and oil-water separation," *Sci. Rep.* **5**, 8701
- Brown, P. and Bhushan, B. (2016), "Designing bioinspired superoleophobic surfaces," *APL Mater.* **4**, 015703
- Budunoglu, H., Yildirim, A., Guler, M.O., and Bayindir, M. (2011), "Highly Transparent, Flexible, and Thermally Stable Superhydrophobic ORMOSIL Aerogel Thin Films," *ACS Appl. Mater. Interf.* **3**, 539-545
- Burton, Z. and Bhushan, B. (2006), "Surface characterization and adhesion and friction properties of hydrophobic leaf surfaces," *Ultramicroscopy* **106**, 709–719
- Callister, W.D. and Rethwisch, D.G. (2013), *Materials Science and Engineering – An Introduction*, 9th ed., Wiley, New York
- Cao, L. and Gao, D. (2010), "Transparent superhydrophobic and highly oleophobic coatings," *Faraday Discuss.* **146**, 57-65
- Cassie, A.B.D. and Baxter, S. (1944), "Wettability of porous surfaces," *Trans. Faraday Soc.* **40**, 546–551

- Chang, C.M. (1994), *Surface Modification and Characterization of Polymers*, Hanser Publishers
- Cheng, S. and Wu, Z. (2010), “Microfluidic stretchable RF electronics,” *Lab Chip* **10**, 3227–3234
- Cho, K.L., Liaw, I.I., Wu, A.H.-F., and Lamb, R.N. (2010), “Influence of Roughness on a Transparent Superhydrophobic Coating,” *J. Phys. Chem. C* **114**, 11228-11233
- Cho, Y.-S., Yi, G.-R., Hong, J.-J., Jang, S.H., and Yang, S.-M. (2006), “Colloidal indium tin oxide nanoparticles for transparent and conductive films,” *Thin Solid Films* **515**, 1864-1871
- Chong, M.A.S., Zheng, Y.B., Gao, H., and Tan, L.K. (2006), “Combinational Template-assisted Fabrication of Hierarchically Ordered Nanowire Arrays on Substrates for Device Applications,” *Appl. Phys. Lett.* **89**, 233104
- Cortese, B., Amone, S. D., Manca, M., Viola, I., Cingolani, R., and Gigli, G. (2008), “Superhydrophobicity Due to the Hierarchical Scale Roughness of PDMS Surfaces,” *Langmuir* **24**, 2712-2718
- Dawood, M. K., Zheng, H., and Liew, T. H. (2011), “Mimicking Both Petal and Lotus Effects on a Single Silicon Substrate by Tuning the Wettability of Nanostructured Surfaces,” *Langmuir* **27**, 4126-4133
- del Campo, A. and Greiner, C. (2007), “SU-8: a Photoresist for High-aspect-ratio and 3D Submicron Lithography,” *J. Micromech. Microeng.* **17**, R81-R95
- Deng, X., Mammen, L., Zhao, Y., Lellig, P., Müllen, K., Li, C., Butt, H.-J., and Vollmer, D. (2011), “Transparent, Thermally Stable and Mechanically Robust Superhydrophobic Surfaces Made from Porous Silica Capsules,” *Adv. Mater.* **23**, 2962-2965
- Dufour, R., Harnois, M., Coffinier, Y., Thomy, V., Boukherroub, R., and Senez, V. (2010), “Engineering Sticky Superomniphobic Surfaces on Transparent and Flexible PDMS Substrate,” *Langmuir* **26**, 17242-17247
- Ebert, D. and Bhushan, B. (2012a), “Durable Lotus-effect surfaces with hierarchical structure using micro- and nanosized hydrophobic silica particles,” *J. Colloid Interf. Sci.* **368**, 584-591
- Ebert, D. and Bhushan, B. (2012b), “Wear-resistant rose petal-effect surfaces with superhydrophobicity and high droplet adhesion using hydrophobic and hydrophilic nanoparticles,” *J. Colloid Interf. Sci.* **384**, 182-188

- Ebert, D. and Bhushan, B. (2012c), “Transparent, Superhydrophobic, and Wear-Resistant Coatings on Glass and Polymer Substrates Using SiO₂, ZnO, and ITO Nanoparticles,” *Langmuir* **28**, 11391–11399
- Ebert, D. and Bhushan, B. (2016), “Transparent, superhydrophobic, and wear-resistant surfaces using deep reactive ion etching on PDMS substrates,” *J. Colloid Interf. Sci.* **481**, 82-90
- Ederth, J., Heszler, P., Hultåker, A., Niklasson, G.A., and Granqvist, C.G. (2003), “Indium tin oxide films made from nanoparticles: models for the optical and electrical properties,” *Thin Solid Films* **445**, 199-206
- Englert, B.C., Xiu, Y., and Wong, C.P. (2006), “Deposition and Surface Treatment of Microparticles to Produce Lotus-Effect Surface,” *Advanced Packaging Materials: Processes, Properties and Interface, 11th International Symposium on*, 73-78
- Feng, L., Zhang, Y., Xi, J., Zhu, Y., Wang, N., Xia, F., and Jiang, F. (2008), “Petal Effect: A Superhydrophobic State with High Adhesive Force,” *Langmuir* **24**, 4114-4119
- Gao, W., Dickinson, L., Grozinger, C., Morin, F.G., and Reven, L. (1996), “Self-Assembled Monolayers of Alkylphosphonic Acids on Metal Oxides,” *Langmuir* **12**, 6429-6435
- Gao, L. and McCarthy, T. (2007), “How Wenzel and Cassie Were Wrong,” *Langmuir* **23**, 3762-3765
- Garra, J., Long, T., Currie, J., Schneider, T., White, R., and Paranjape, M. (2002), “Dry etching of polydimethylsiloxane for microfluidics systems,” *J. Vac. Sci. Technol. A* **20**, 975–982
- Ghosh, N., Bajoria, A., and Vaidya, A. (2009), “Surface Chemical Modification of Poly(dimethylsiloxane)-Based Biomimetic Materials: Oil-Repellent Surfaces,” *ACS Appl. Mater. Interf.* **1**, 2636–2644
- Gonzalez, M., Axisa, F., Bossuyt, F., Hsu, Y., Vandeveld, B., and Vanfleteren, J. (2009), “Design and performance of metal conductors for stretchable electronic circuits,” *Circuit World* **35**, 22–30
- Hamberg, I. and Granqvist, C.G. (1984), “Band-gap widening in heavily Sn-doped In₂O₃,” *Phys. Rev. B* **30**, 3240-3249

- Han, J.T., Kim, S.Y., Woo, J.S., and Lee, G.-W. (2008), “Transparent, Conductive, and Superhydrophobic Films from Stabilized Carbon Nanotube/Silane Sol Mixture Solution,” *Adv. Mater.* **20**, 3724-3727
- He, Z., Ma, M., Lan, X., Chen, F., Wang, K., Deng, H., Zhang, Q., and Fu, Q. (2011), “Fabrication of a transparent superamphiphobic coating with improved stability,” *Soft Matter* **7**, 6435-6443
- Hikita, M., Tanaka, K., Nakamura, T., Kajiyama, T., and Takahara, A. (2005), “Super-Liquid-Repellent Surfaces Prepared by Colloidal Silica Nanoparticles Covered with Fluoroalkyl Groups,” *Langmuir* **21**, 7299-7302
- Hong, X., Gao, X., and Jiang, L. (2007), “Application of Superhydrophobic Surface with High Adhesive Force in No Lost Transport of Superparamagnetic Microdroplet,” *J. Am. Chem. Soc.* **129**, 1478-1479
- Hwang, S., Oh, D., Jung, P., Lee, S., Go, J., Kim, J., Hwang, K., and Ko, J. (2009), “Dry etching of polydimethylsiloxane using microwave plasma,” *J. Micromech. Microeng.* **19**, 095010
- Im, M., Im, H., Lee, J.-H., Yoon, J.-B., and Choi, Y.-K. (2010), “A robust superhydrophobic and superoleophobic surface with inverse-trapezoidal microstructures on a large transparent flexible substrate,” *Soft Matter* **6**, 1401–1404
- Irzh, A., Ghindes, L., and Gedanken, A. (2011), “Rapid Deposition of Transparent Super-Hydrophobic Layers on Various Surfaces Using Microwave Plasma,” *ACS Appl. Mater. Interf.* **3**, 4566-4572
- Johnston, I.D., McCluskey, D.K., Tan, C.K.L., and Tracey, M.C. (2014), “Mechanical characterization of bulk Sylgard 184 for microfluidics and microengineering,” *J. Micromech. Microeng.* **24**, 035017
- Jung, Y.C. and Bhushan, B. (2007), “Wetting transition of water droplets on superhydrophobic patterned surfaces,” *Scripta Materiala* **57**, 1057-1060
- Jung, Y.C. and Bhushan, B. (2009), “Mechanically Durable Carbon Nanotube-Composite Hierarchical Structures with Superhydrophobicity, Self-Cleaning, and Low-Drag,” *ACS Nano* **3**, 4155-4163
- Karunakaran, R.G., Lu, C.-H., Zhang, Z., and Yang, S. (2011), “Highly Transparent Superhydrophobic Surfaces from the Coassembly of Nanoparticles (≤ 100 nm),” *Langmuir* **27**, 4594-4602

- Kavale, M.S., Mahadik, D.B., Parale, V.G., Wagh, P.B., Gupta, S.C., Rao, A.V., and Barshilia, H.C. (2011), "Optically transparent, superhydrophobic methyltrimethoxysilane based silica coatings without silylating reagent," *Appl. Surf. Sci.* **258**, 158-162
- Kim, H., Gilmore, C. M., Piqué, A., Horwitz, J. S., Mattoussi, H., Murata, H., Kafafi, Z. H., and Chrisey, D.B. (1999), "Electrical, optical, and structural properties of indium-tin-oxide thin films for organic light-emitting devices," *J. Appl. Phys.* **86**, 6451-6461
- Kim, J., Chaudhury, M., and Owen, M.J. (2000), "Hydrophobic recovery of Polydimethylsiloxane Elastomer Exposed to Partial Electrical Discharge," *J. Colloid Interface Sci.* **226**, 231-236
- Kim, M., Moon, B.-U., and Hidrovo, C.H. (2013), "Enhancement of the thermo-mechanical properties of PDMS molds for the hot embossing of PMMA microfluidic devices," *J. Micromech. Microeng.* **23**, 095024
- Koch, K. and Barthlott, W. (2009), "Superhydrophobic and superhydrophilic plant surfaces: an inspiration for biomimetic materials," *Phil. Trans. R. Soc. A* **367**, 1487-1509
- Koch, K., Bhushan, B., and Barthlott, W. (2008), "Diversity of Structure, Morphology, and Wetting of Plant Surfaces (invited)," *Soft Matter* **4**, 1943-1963
- Koch, K., Bhushan, B., and Barthlott, W. (2009a), "Multifunctional Surface Structures of Plants: An Inspiration for Biomimetics (invited)," *Prog. Mater. Sci.* **54**, 137-178
- Koch, K., Bhushan, B., Jung, Y.C., and Barthlott, W. (2009b), "Fabrication of Artificial Lotus Leaves and Significance of Hierarchical Structure for Superhydrophobicity and Low Adhesion," *Soft Matter* **5**, 1386-1393
- Kuan, C.Y., Hon, M.H., Chou, J.M. and Leu, I.C. (2009), "Wetting Characteristics on Micro/Nanostructured Zinc Oxide Coatings," *J. Electrochem. Soc.* **156**, J32-J36
- Kucheyev, S.O., Bradby, J.E., Williams, J.S., and Jagadish, C. (2002), "Mechanical deformation of single-crystal ZnO," *J. Appl. Phys.* **80**, 956-958
- Kulinich, S., and Farzaneh, M. (2009), "How Wetting Hysteresis Influences Ice Adhesion Strength on Superhydrophobic Surfaces," *Langmuir* **25** 8854-8856
- Li, W. and Amirfazli, A. (2008), "Hierarchical structures for natural superhydrophobic surfaces," *Soft Matter* **4**, 462-466

- Li, Y., Liu, F., and Sun, J. (2009), "A facile layer-by-layer deposition process for the fabrication of highly transparent superhydrophobic coatings," *Chem. Commun.* **19**, 2730-2732
- Ling, X.Y., Phang, I.Y., Vancso, G.J., Huskens, J., and Reinhoudt, D.N. (2009), "Stable and Transparent Superhydrophobic Nanoparticle Films," *Langmuir* **25**, 3260-3263
- Liu, K., Yao, X., and Jiang, L. (2010), "Recent developments in bio-inspired special wettability," *Chem. Soc. Rev.* **39**, 3240-3255
- Liu, M., Zheng, Y., Zhai, J., and Jiang, L. (2010), "Bioinspired Super-antiwetting Interfaces with Special Liquid-Solid Adhesion," *Acc. Chem. Res.* **43**, 368-377
- Liu, X., and He, J. (2007), "Hierarchically structured superhydrophilic coatings fabricated by self-assembling raspberry-like silica nanospheres" *J. Colloid and Interf. Sci.* **314**, 341-345
- Liu, X., Din, X., and He, J. (2008), "Hierarchically Structured Porous Films of Silica Hollow Spheres via Layer-by-Layer Assembly and Their Superhydrophilic and Antifogging Properties," *Chem. Phys. Chem.* **9**, 305-309
- Liu, Y., Chen, X., and Xin, J.H. (2006), "Super-hydrophobic surfaces from a simple coating method: a bionic nanoengineering approach," *Nanotechnology* **17**, 3259-3263
- Malitson, I.H. (1965), "Interspecimen Comparison of the Refractive Index of Fused Silica," *J. Optical Soc. America* **55**, 1205-1209
- Manakasettharn, S., Hsu, T.-H., Myhre, G., Pau, S., Taylor, J.A., and Krupenkin, T. (2012), "Transparent and superhydrophobic Ta₂O₅ nanostructured thin films," *Opt. Mater. Express* **2**, 214-221
- Manca, M., Cortese, B., Viola, I., Aricò, A., Cingolani, R., and Gigli, G. (2008), "Influence of Chemistry and Topology Effects on Superhydrophobic CF₄-Plasma-Treated Poly(dimethylsiloxane) (PDMS)," *Langmuir* **24**, 1833-1843
- Manca, M., Cannavale, A., De Marco, L., Aricò A.S., Cingolani, R., and Gigli, G. (2009), "Durable Superhydrophobic and Antireflective Surfaces by Trimethylsilanized Silica Nanoparticles-Based Sol-Gel Processing," *Langmuir* **25**, 6357-6362
- Mark, J.E. (1999), *Polymer Data Handbook*, Oxford University Press, U.K.

- McClain, M., LaPlaca, M., and Allen, M. (2009), "Spun-cast micromolding for etchless micropatterning of electrically functional PDMS structures," *J. Micromech. Microeng.* **19**, 107002
- McHale, G. (2007), "Cassie and Wenzel: Were They Really So Wrong?" *Langmuir* **23**, 8200-8205
- Ming, W., Wu, D., van Benthem, R., and de With, G. (2005), "Superhydrophobic Films from Raspberry-like Particles," *Nano Lett.* **5**, 2298-2301
- Mishchenko, L., Hatton, B., Bahadur, V., Taylor, J., Krupenkin, T., and Aizenberg, J., (2010), "Design of Ice-free Nanostructured Surfaces Based on Repulsion of Impacting Water Droplets," *ACS Nano* **4**, 7699-7707
- Moustaghfir, A., Tomasella, E., Rivaton, A., Mailhot, B., Jacquet, M., Gardette, J.L., and Cellier, J. (2004), "Sputtered zinc oxide coatings: structural study and application to the photoreception of the polycarbonate," *Surface Coatings Technol.* **180-181**, 642-645
- Nakajima, A., Fujishima, A., Hashimoto, K., and Watanabe, T. (1999), "Preparation of Transparent Superhydrophobic Boehmite and Silica Films by Sublimation of Aluminum Acetylacetonate," *Adv. Mater.* **11**, 1365-1368
- Natsume, Y. and Sakata, H. (2000), "Zinc oxide films prepared by sol-gel spin-coating," *Thin Solid Films* **372**, 30-36
- Nishimoto, S., Kubo, A., Nohara, K., Zhang, X., Taneichi, N., Okui, T., Liu, Z., Nakata, K., Sakai, H., Murakami, T., Abe, M., Komine, T., and Fujishima, A. (2009), "TiO₂-based superhydrophobic-superhydrophilic patterns: Fabrication via an ink-jet technique and application in offset printing," *Appl. Surf. Sci.* **255**, 6221-6225
- Nishino, T., Meguro, M., Nakamae, K., Matsushita, M., and Ueda, Y. (1999), "The Lowest Surface Free Energy Based on -CF₃ Alignment," *Langmuir* **15**, 4321-4323
- Noh, J.H., Han, H.S., Lee, S., Kim, D.H., Park, J.H., Park, S., Kim, J.Y., Jung, H.S., and Hong, K.S. (2010), "A Newly Designed Nb-Doped TiO₂/Al-Doped ZnO Transparent Conducting Oxide Multilayer for Electrochemical Photoenergy Conversion Devices," *J. Phys. Chem. C* **114**, 13867-13871
- Nosonovsky, M. and Bhushan, B. (2007), "Hierarchical roughness makes superhydrophobic states stable," *Microelectronic Engineering* **84**, 382-386

- Nosonovsky, M. and Bhushan, B. (2008), *Multiscale Dissipative Mechanisms and Hierarchical Surfaces: Friction, Superhydrophobicity, and Biomimetics*, Springer-Verlag, Heidelberg, Germany
- Park, T.-Y., Choi, Y.-S., Kang, J.-W., Jeong, J.-H., Park, S.-J., Jeon, D.M., Kim, J.W., and Kim, Y.C. (2010), "Enhanced optical power and low forward voltage of GaN-based light-emitting diodes with Ga-doped ZnO transparent conducting layer," *Appl. Phys. Lett.* **96**, 051124
- Patankar, N.A. (2004), "Mimicking the Lotus Effect: Influence of Double Roughness Structures and Slender Pillars," *Langmuir* **20**, 8209-8213
- Patel, P., Choi, C., and Meng, D. (2010), "Superhydrophilic Surfaces for Antifogging and Antifouling Microfluidic Devices," *J. Association for Laboratory Automation* **15**, 114-119
- Petrenko, V., and Peng, S. (2003), "Reduction of ice adhesion to metal by using self-assembling monolayers (SAM)," *Canadian Journal of Physics* **81**, 387-393
- Sakai, N., Fujishima, A., Watanabe, T., Hashimoto, K. (2001), "Enhancement of the Photoinduced Hydrophilic Conversion Rate of TiO₂ Film Electrode Surfaces by Anodic Polarization," *J. Phys. Chem. B* **105**, 3023-3026
- Schneider, P.M. and Fowler, W.B. (1976), "Band Structure and Optical Properties of Silicon Dioxide," *Phys. Rev. Lett.* **36**, 425-428
- Shackelford, J. and Alexander, W. (2001), *CRC Materials Science and Engineering Handbook*, 3rd ed., CRC Press, Boca Raton, FL p. 1716
- Shirtcliffe, N.J., McHale, G., Newton, M.I., Chabrol, G., Perry, C.C. (2004), "Dual-scale Roughness Produces Unusually Water-repellent Surfaces," *Adv. Mater.* **16**, 1929-1932
- Srikant, V. and Clarke, D. (1998), "On the optical band gap of zinc oxide," *J. Appl. Phys.* **83**, 5447-5451
- Stanton, M.M., Ducker, R.E., MacDonald, J.C., Lambert, C.R., and McGimpsey, W.G. (2012), "Super-hydrophobic, highly adhesive, polydimethylsiloxane (PDMS) surfaces," *J. Coll. Interf. Sci.* **367**, 502-508
- Su, C., Li, J., Geng, H., Wang, Q., and Chen, Q. (2006), "Fabrication of an optically transparent super-hydrophobic surface via embedding nano-silica," *Appl. Surf. Sci.* **253**, 2633-2636

- Sun, M., Luo, C., Xu, L., Ji, H., Ouyang, Q., Yu, D., and Chen, Y. (2005), "Artificial Lotus Leaf by Nanocasting," *Langmuir* **21**, 8978-8981
- Sun, T., Wang, G., Feng, L., Liu, B., Ma, Y., Jiang, L., and Zhu, D. (2004), "Reversible Switching between Superhydrophilicity and Superhydrophobicity," *Angew. Chem. Int. Ed* **43**, 357-360
- Tadanaga, K., Kitamuro, K., Matsuda, A., and Minami, T. (2003), "Formation of Superhydrophobic Alumina Coating Films with High Transparency on Polymer Substrates by the Sol-Gel Method," *J. Sol-Gel Sci. Technol.* **26**, 705-708
- Tarwal, N.L. and Patil, P.S. (2010), "Superhydrophobic and transparent ZnO thin films synthesized by spray pyrolysis technique," *Appl. Surf. Sci.* **256**, 7451-7456
- Teshima, K., Sugimura, H., Inoue, Y., Takai, O., and Takano, A. (2005), "Transparent ultra water-repellent poly(ethylene terephthalate) substrates fabricated by oxygen plasma treatment and subsequent hydrophobic coating," *Appl. Surf. Sci.* **244**, 619-622
- Tourkine, P., Le Merrer, M., and Quéré, D. (2009), "Delayed Freezing on Water Repellent Materials," *Langmuir* **25**, 7214-7216
- Tropmann, A., Tanguy, L., Koltay, P., Zengerle, R., and Riegger, L. (2012), "Completely Superhydrophobic PDMS Surfaces for Microfluidics," *Langmuir* **28**, 8292-8295
- Tserepi, A., Vlachopoulou, M., and Gogolides, E. (2006), "Nanotexturing of poly(dimethylsiloxane) in plasmas for creating robust super-hydrophobic surfaces," *Nanotechnology* **17**, 3977-3983
- Vila, M., Cáceres, D., and Prieto, C. (2003), "Mechanical properties of sputtered silicon nitride thin films," *J Appl. Phys.* **94**, 7868-7873
- Vourdas, N., Tserepi, A., and Gogolides, E. (2007), "Nanotextured super-hydrophobic transparent poly(methyl methacrylate) surface using high-density plasma processing," *Nanotechnology* **18**, 125304
- Watanabe, T., Nakajima, A., Wang, R., Minabe, M., Koizumi, S., Fujishima, A., and Hashimoto, K. (1999), "Photocatalytic activity and photoinduced hydrophilicity of titanium dioxide coated glass," *Thin Solid Films* **351**, 260-263
- Wenzel, R.N. (1936), "Resistance of solid surfaces to wetting by water," *Ind. Eng. Chem.* **28**, 988-994

- Winkleman, A., Gotesman, G., Yoffe, A., and Naaman, R. (2008), "Immobilizing a Drop of Water: Fabricating Highly Hydrophobic Surfaces that Pin Water Droplets," *Nano Lett.* **8**, 1241-1245
- Xiu, Y., Xiao, F., Hess, D.W., and Wong, C.P. (2009), "Superhydrophobic optically transparent silica films formed with a eutectic liquid," *Thin Solid Films* **517**, 1610-1615
- Xu, L., Karunakaran, R.G., Guo, J., and Yang, S. (2012), "Transparent, Superhydrophobic Surfaces from One-Step Spin Coating of Hydrophobic Nanoparticles," *ACS Appl. Mater. Interfaces* **4**, 1118-1125
- Xu, Q.F., Wang, J.N., Smith, I.H., and Sanderson, K.D. (2009), "Superhydrophobic and transparent coatings based on removable polymeric spheres," *J. Mater. Chem.* **19**, 655-660
- Yanagisawa, T., Nakajima, A., Sakai, M., Kameshima, Y., and Okada, K. (2009), "Preparation and abrasion resistance of transparent super-hydrophobic coating by combining crater-like silica films with acicular boehmite powder," *Mater. Sci. Eng. B* **161**, 36-39
- Yang, Y., Sun, X.W., Chen, B.J., Xu, C.X., Chen, T.P., Sun, C.Q., Tay, B.K., and Sun, Z. (2006), "Refractive indices of textured indium tin oxide and zinc oxide thin films," *Thin Solid Films* **510**, 95-101
- Zanini, S., Barni, R., Della Pergola, R., and Riccardi, C. (2014), "Development of superhydrophobic PTFE and PET surfaces by means of plasma processes," *J. Phys. Conf. Ser.* **550**, 012029
- Zeng, K., Zhu, F., Hu, J., Shen, L., Zhang, K., and Gong, H. (2003), "Investigation of mechanical properties of transparent conducting oxide thin films," *Thin Solid Films* **443**, 60-65
- Zhang, B., Kong, T., Xu, W., Su, R., Gao, Y., and Cheng, G. (2010), "Surface functionalization of Zinc Oxide by Carboxyalkylphosphonic Acid," *Langmuir* **26**, 4514-4522
- Zhang, X., Shi, F., Niu, J., Jiang, Y., and Wang, Z. (2008), "Superhydrophobic surfaces: from structural control to functional application," *J. Mater. Chem.* **18**, 621-633
- Zhao, X.D., Fan, H.M., Liu, X.Y., Pan, H., Xu, H.Y. (2011), "Pattern-Dependent Tunable Adhesion of Superhydrophobic MnO₂ Nanostructured Film," *Langmuir* **27**, 3224-3228

Zhao, Y., Li, M., Lu, Q., and Shi, Z. (2008), "Superhydrophobic Polyimide Films with a Hierarchical Topography: Combined Replica Molding and Layer-by-Layer Assembly," *Langmuir* **24**, 12651-12657

Zheng, L., Li, Z., Bourdo, S., Saini, V., Ryerson, C., and Biris, A.S. (2011), "Hierarchical ZnO Structure with Superhydrophobicity and High Adhesion," *Chem. Phys. Chem.* **12**, 2412-2414